COMPUTATIONAL MODELLING OF THE VORTEX STATE IN HIGH-TEMPERATURE SUPERCONDUCTORS

By
Hans Fangohr

Doctor of Philosophy

Department of Electronics and Computer Science,
University of Southampton,
United Kingdom.

June 2002

UNIVERSITY OF SOUTHAMPTON

ABSTRACT

FACULTY OF ENGINEERING

ELECTRONICS AND COMPUTER SCIENCE DEPARTMENT

Doctor of Philosophy

COMPUTATIONAL MODELLING OF THE VORTEX STATE IN HIGH-TEMPERATURE SUPERCONDUCTORS

by Hans Fangohr

The vortex state in high temperature superconductors is investigated using computer simulations. Vortices are represented as particles and we employ Langevin dynamics to study the statics and dynamics of the system.

We show that the long-range nature of the vortex-vortex interaction can result in numerical artefacts, and provide two techniques to overcome these problems: (i) using a 'smooth' cut-off which reduces the interaction force near the cut-off smoothly to zero, and (ii) an infinite lattice summation technique applicable for a K_0-Bessel function interaction potential.

Using these methods, we investigate a two-dimensional vortex system driven over a weak random potential. We observe the moving Bragg glass regime, and study the recently predicted critical transverse force. Our results agree with and extend other theoretical and numerical works, and provide important confirmation for the moving glass theory. We investigate the critical transverse force as a function of system size, temperature, driving force and disorder strength. We provide numerical estimates to assist experimentalists in verifying its existence.

We study vortex matter in three-dimensional layered superconductors in the limit of zero Josephson coupling. The long-range nature of the electromagnetic interaction between pancake vortices in the c-direction allows us to employ a mean-field method: all attractive inter-layer interactions are described by a substrate potential, which pancakes experience in addition to the in-layer pancake repulsion. Using an averaged pancake-density, we iteratively re-compute the substrate potential. The self-consistent method converges, depending on temperature, either to a pancake lattice or a pancake liquid. We investigate different methods to perform these simulations efficiently, and compute the instability line for the transition from solid to liquid, the melting line and the entropy jump across the transition.

Contents

List of Tables

List of Figures

Acknowledgements

I would like to thank my supervisors Prof. S. J. Cox and Prof. P. A. J. de Groot for providing the opportunity to perform this work, and for their support and guidance. For their financial support I am grateful to the funding body of EPSRC and to the Department of Electronics and Computer Science at the University of Southampton.

I am thankful to Dr. Jacek M. Generowicz from whom I learned much about programming, software tools and operating systems. He was always happy to discuss the pitfalls of numerical analysis, and in an indirect way he contributed much to the efficient implementation of this work.

I had the opportunity to work with some of the finest scientists in this field, and I would like to thank Dr. Matthew J. W. Dodgson and Dr. Alexei E. Koshelev for their patience and their advice on the physics of the vortex state.

I am thankful to a number of people who have contributed to this work, mainly through helpful discussions: Dr. G. J. Daniell, Dr. A. R. Price, Dr. S. Gordeev, Dr. A. A. Zhukov, Dr. P. Le Doussal, Dr. D. A. Nicole, Dr. V. Vinokur, and Prof. L. Radzihovsky.

The members of the High Performance Computing Group could always be relied on to have a coffee break at any time of the day which made the work even more enjoyable. Thanks also to Mimi who made my grant last quite a bit longer.

Finally, love and thanks to Susanne who has seen me through the highs and lows along the way.

Author's declaration

The work detailed in this report is partly the result of collaborative studies. The author recognises the following as the efforts of others:

Prof. Simon J. Cox had the idea to use an infinite lattice summation as described in Section 4.6, and provided the data for figures 4.7 and 4.9.

Dr. Andrew R. Price provided the figures 4.3 and 4.5 which he created using his Monte Carlo simulations of the vortex state.

Dr. Alexei E. Koshelev provided the plot shown on the right-hand side in figure 6.7 and figure 6.9. He also suggested to use the reduced-Q Fourier-filtered method for the computation of the substrate potential.

Publications

Publications based on the work presented in this thesis:

- Fangohr H, Price A, Cox S, de Groot PAJ, Daniell GJ and Thomas KS. "Efficient methods for handling long-range forces in particle-particle simulations." *J. Comput. Phys*, **162**, 372–384 (2000).

- Fangohr H, de Groot PAJ and Cox SJ. " Critical transverse forces in weakly pinned driven vortex systems." *Physical Review B*, **63**, 064501 (2001).

- Fangohr H, Koshelev AE and Dodgson MJW. "Vortex matter in layered superconductors without josephson coupling: numerical simulations within mean field approach." *cond-mat/0210580* (2002). Submitted to Phys. Rev. B.

- Fangohr H, Koshelev AE and Dodgson MJW. "Vortex matter in layered superconductors without josephson coupling in the presence of random pinning: numerical simulations within mean field approach." In preparation for submission.

Chapter 1

Introduction

Superconductivity has fascinated scientists ever since *Kamerlingh Onnes* discovered in 1911 that some materials lose their electric resistance below a critical temperature. The ability to conduct electricity without any dissipation and thus to create large magnetic fields is of great technological interest. While superconductors are already routinely used, for example in Magnetic Resonance Imaging (MRI), widespread use is limited by two factors. Firstly, the critical temperatures below which superconductivity occurs are below 150 Kelvin (K) even for so-called "high-temperature" superconductors. Secondly, in the presence of magnetic fields dissipation occurs through the interaction of the magnetic flux with the current inside the material.

In this work we will focus on the behaviour of the magnetic flux that enters the superconductor in form of "vortex lines". About 15 years ago the discovery of high-temperature superconductors (*Bednorz and Müller*, 1986) stimulated strong interest in the physics of vortex lines. High-temperature superconductors are extreme type-II superconductors and exclude only small magnetic fields below approximately 10^{-2} Tesla (T). Stronger fields up to about 100T penetrate as an array of magnetic flux lines, each consisting of exactly one quantum of magnetic flux surrounded by circulating supercurrents. These flux lines are called vortices. In the presence of a transport current, vortices experience a Lorentz force pushing them in a direction perpendicular to the current and the magnetic field. Motion of vortices resulting from this force, causes dissipation of energy. Crystal imperfections attract vortices and can inhibit vortex motion. Thus, it is of great technological interest to understand how the vortex lines can be pinned to the material most efficiently.

The vortex state is also of great importance for fundamental science. Vortices are flexible one-dimensional objects that repel each other, and imperfections in the

crystal structure impose disorder onto the system. In addition, they can be subjected to a Lorentz force due to a transport current, and show thermal fluctuations. The vortex-vortex interaction favours a hexagonal vortex lattice, whereas thermal fluctuations and random pinning favour a liquid or a disordered glassy vortex state. The vortex state is dominated by the competition between these energies, and the equilibrium phases include crystalline, liquid, and glassy states. The situation is complicated further by the anisotropy and layered structure of the high-temperature superconductors. For driven systems the non-equilibrium states show remarkable complexity and contain several types of plastic and elastic motion. The statistical mechanics of driven interacting elastic media in the presence of disordering forces is not yet fully understood.

The complex behaviour of the statics and the dynamics of the vortex state can be described theoretically only by highly simplified models; in which case the properties can be investigated analytically. It is then vital to attempt to assess how appropriate the chosen simplifications are. Experiments provide a wealth of data on macroscopic systems (consisting of many millions of vortices) but it is very hard to deduce from these the microscopic details of the vortex state.

Computer simulations form a bridge between theory and experiments: on the one hand computational models are based on certain assumptions which simplify the true situation, but on the other hand computations can be performed for systems which are much more complex and closer to reality than can be described by analytical theory. In this respect computer simulations play an important role in assessing the appropriateness of theoretical models. The microscopic vortex configurations can be studied in detail since all vortex positions and velocities are known. Furthermore, a virtual experiment can be performed numerically and then related to real experimental data via macroscopic observables (such as the average vortex velocity and the measured voltage). Due to computational constraints, simulated vortex systems are currently limited to sizes of a few thousand vortices. In spite of this restriction, computer simulations provide valuable insight into the different phases of the vortex state.

One of the challenges for such numerical simulations is that the interaction between vortices are long-range. Not only does this increase the computational effort significantly in comparison to short-range interactions, but it also poses the question whether it is acceptable to cut off the interaction for large distances. In this work, we start by investigating this problem. We demonstrate that using a

cut-off can result in artefacts, and we present two methods which can avoid these problems (Chapter 4). We employ these methods in chapters 5 and 6.

Over the last decade the experimental and theoretical interest has been extended from the statics of the vortex state (*e.g. Larkin and Ovchinnikov*, 1979, *Blatter et al.*, 1994, *Giamarchi and Le Doussal*, 1995) to the dynamic phases of the vortex state. *Koshelev and Vinokur* (1994) first proposed and demonstrated numerically a dynamic phase transition between the plastically deformed phase and a moving lattice for the moving vortex lines in the presence of random pinning. Further theoretical work was done by *Giamarchi and Le Doussal* (1996), *Balents et al.* (1997, 1998), *Le Doussal and Giamarchi* (1998) and *Scheidl and Vinokur* (1998). The predicted reordering of a rapidly driven vortex lattice across a disordering pinning potential is supported by simulations of two-dimensional vortex systems (*Shi and Berlinsky*, 1991, *Faleski et al.*, 1996, *Moon et al.*, 1996, *Ryu et al.*, 1996, *Spencer and Jensen*, 1997), as well as neutron diffraction (*Thorel*, 1973, *Yaron et al.*, 1994) and decoration experiments (*Pardo et al.*, 1997, 1998). The most recent theoretical descriptions (*Balents et al.*, 1998, *Le Doussal and Giamarchi*, 1998, *Scheidl and Vinokur*, 1998) for high-driving forces predict either a topologically ordered vortex-system which shows algebraic translational order, or for stronger pinning smectic order transverse to the direction of motion. Both regimes can be summarised as a "moving glass" (*Le Doussal and Giamarchi*, 1998). The existence of both moving-glass phases is confirmed by numerical results (*Olson et al.*, 1998b, *Fangohr et al.*, 2001a). Within the moving glass, the existence of a critical transverse force is predicted.

In this work, we carry further the initial work of *Moon et al.* (1996), *Ryu et al.* (1996) and *Olson and Reichhardt* (2000) and investigate the critical transverse force in the moving glass regime of the vortex state in two dimensions. We study the dependence of the critical transverse force on system size, pinning strength and temperature. By varying the disorder strength, we show that the critical transverse force can be used as an order parameter of the moving glass. The critical transverse force reduces with increasing temperature before it vanishes at the melting temperature of the system. Eventually, we provide data that can assist experimentalists in providing the experimental confirmation of the existence of the critical transverse force.

A computationally even more demanding task is the simulation of the three-dimensional vortex state in layered superconductors. While in moderately anisotropic

materials the short-range Josephson coupling is the dominating inter-layer interaction, and the vortices can be described as elastic strings (for example *Ryu and Stroud*, 1996, *Nordborg and Blatter*, 1997, *Wilkin and Jensen*, 1997b, *Nordborg and Blatter*, 1998, *van Otterlo et al.*, 1998, *Olson et al.*, 2000b), in very anisotropic materials on the other hand, the Josephson coupling is weak and the long-range electromagnetic interaction between the pancakes has to be taken into account.

The challenge for a numerical investigation is that the interlayer interaction between pancakes extends over a range of approximately 100 layers. In principle, one can stack a set of two-dimensional pancake systems on top of each other, and introduce additional interlayer interactions but the computational effort grows with the square of the number of layers. It is therefore only possible to study relatively small systems with 10 layers and about 100 pancakes in each layer (*e.g. Kolton et al.*, 2000b, *Olson et al.*, 2001).

Recently, *Dodgson, Koshelev, Geshkenbein and Blatter* (2000b) suggested using a mean-field method to deal with the inter-layer interaction. Using a self-consistent harmonic approximation, they managed to estimate the melting line for a layered pancake system in the limit of no Josephson coupling and no pinning.

In chapter 6, we show how to implement and use the mean field method suggested by *Dodgson et al.* (2000b) to study three-dimensional pancake systems in the limit of dominating electromagnetic interactions. We compute the interactions within the layers explicitly rather than using analytical approximations, and employ a substrate potential to represent the inter-layer interactions. Using this novel technique, we study the phase diagram of a three-dimensional layered superconductor in the absence of pinning. In contrast to the Lindemann approach, we can not only estimate the melting line, but also study the nature of the transition. We map out the phase diagram and compute the entropy jump across the transition.

In chapter 2, a short overview of superconductivity is given which focuses on aspects important for this work. In chapter 3 we describe the computer simulation we have developed and implemented. Chapter 4 presents our results from investigating the cut-off approach for systems with long-range interactions, and shows two ways of solving the resulting problems. We add random pinning to our simulations and study the critical transverse force in a driven system in chapter 5. In chapter 6 we extend our model to three dimensions, and study a layered pancake vortex system in the absence of pinning using a mean field approach. We close with a summary in chapter 7. The appendices A to C contain additional derivations and details that have been removed from the preceeding chapters for brevity.

Chapter 2

The vortex state

2.1 Superconductivity

Kamerlingh Onnes found in 1911 that the electrical resistance of Mercury drops below any measurable value when it was cooled below a critical temperature of $T_c = 4.2$ K. This effect was christened "superconductivity" and many more elements and compounds have been found to become superconducting at sufficiently low temperatures, including the recently discovered magnesium diboride (*Nagamatsu et al.*, 2001). The critical temperature T_c below which the superconductivity exists has been increased up to well above 100 K in the late 1980s after the discovery by *Bednorz and Müller* (1986) of a new class of cuprate superconductors.

The understanding of conventional type-I superconductors, which expel an external magnetic field completely, is relatively good. In 1935 *London and London* proposed equations which govern the behaviour of microscopic electric and magnetic fields and introduced the characteristic length λ, which is now called the London penetration depth. *Bardeen, Cooper and Schrieffer* (BCS) produced their Nobel prize winning theory of superconductivity in 1957 from which the London equations can be derived. It states that there is a phonon-mediated attraction between superconducting electrons. Two electrons with equal but opposite momentum and spin can form a so-called "Cooper pair". The spatial extension of such a pair is given by the *Pippard* coherence length (1953), and the Cooper pairs are separated from the normal conducting electrons by an energy gap.

Already in 1950 *Ginzburg and Landau* published their theory which is based on Landau's general theory of phase transitions. They introduced a complex pseudo-wave-function ψ as an order parameter which measures the "superconducting order" and derived differential equations which couple ψ and the magnetic vector potential. Ginzburg and Landau introduced the Ginzburg-Landau coherence length $\xi(T)$

which, sufficiently far below T_c, is similar to the temperature independent Pippard coherence length. It has been shown subsequently that the Ginzburg-Landau theory is a limiting form of a suitably generalised BCS-theory (*Gorkov*, 1959). The ratio of the London penetration depth, λ, and the Ginzburg-Landau coherence length, ξ, defines the Ginzburg-Landau parameter $\kappa = \lambda/\xi$.

The quantitative description of the high-temperature superconductors is based on the phenomenological Ginzburg-Landau theory, Abrikosov's work on the vortex state (as described in section 2.2), and Gorkov's work. It is therefore occasionally referenced as the GLAG-description. However, a theoretical description of the pairing mechanism giving rise to superconductivity is still lacking.

2.2 The vortex state

In 1957 *Abrikosov* investigated theoretically what would happen if the Ginzburg-Landau parameter, κ, was larger than 1, in contrast to being much smaller than 1, as it is for classical pure superconductors. He found that the surface energy of an interface of a superconducting and a normal region would be negative. It turned out that a sample of such a material being exposed to a magnetic field (near the upper critical field H_{c2}) would be subdivided into smaller and smaller domains of alternating superconducting and non-superconducting regions to reduce the system's overall energy. Abrikosov called these materials "type-II" superconductors because their behaviour differs strongly from the classical type-I superconductors.

It is now established that the normal regions are tube-like flux lines which penetrate a type-II superconductor in the form of a regular triangular array (in the absence of any disordering effects). Each of these flux lines, which are also called vortices, carries a magnetic flux quantum $\Phi_0 = h/2e$, with h being Planck's constant and e the electron charge. Each flux line is surrounded by a supercurrent screening the enclosed magnetic induction. Figure 2.1 on the following page shows the magnetic induction and the superconducting order parameter in the neighbourhood of a vortex.

Type-I superconductors with $\kappa < 1/\sqrt{2}$ expel an external magnetic field completely up to a critical field value H_c at which the superconductivity breaks down, as demonstrated schematically in figure 2.2 on the next page (dotted line). Type-II superconductors show the same behaviour for small fields but only up to field strengths $H_{c1} < H_c$. For field strengths between H_{c1} and H_{c2}, the external field penetrates the bulk in the form of vortices. This regime is called the "vortex state" or the "mixed state" and it is this situation which has been investigated in this

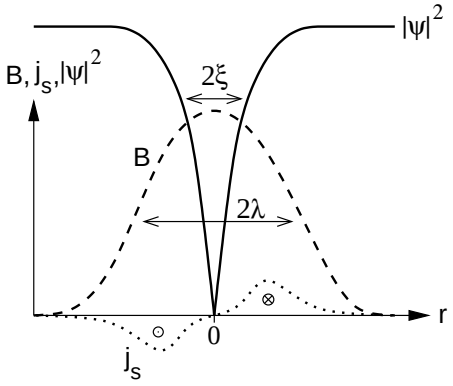

Figure 2.1: Spatial variation of the Cooper pair density $|\psi|^2$, the magnetic induction B, and the supercurrent j_s around the vortex centre. The magnetic induction drops to zero over the length scale given by the London penetration depth, λ, and the superconducting order parameter, ψ, varies on the length scale ξ.

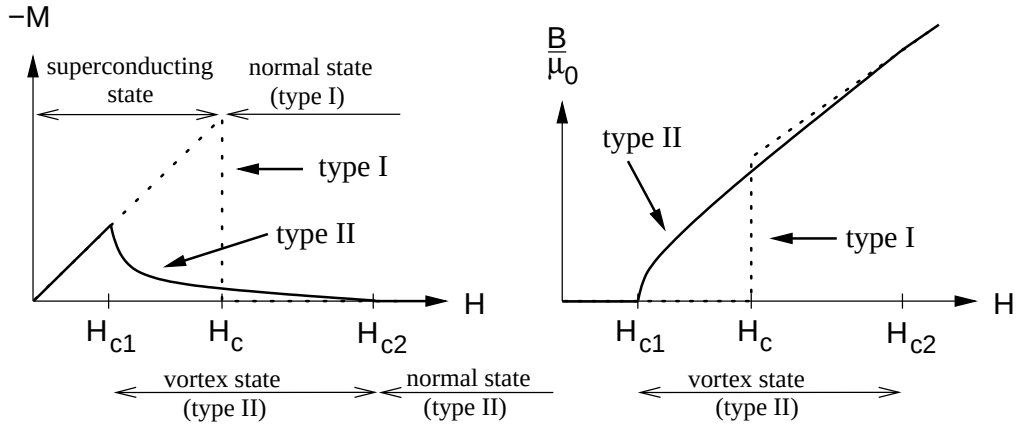

Figure 2.2: Different behaviour of magnetisation M *(left)* and magnetic induction B *(right)* to an external applied magnetic field H in type-I and type-II superconductors. In type-II superconductors, vortices start penetrating the material at H_{c1} and represent B within the sample. At H_{c2} the vortex cores overlap and the external field H_{c2} is established as superconductivity breaks down.

work. Because of the partial flux penetration, the diamagnetic energy cost of expelling the field is reduced and therefore H_{c2} can be significantly larger than H_c. This property has made high-field superconductors possible.

In the mixed state, vortices tend to align in a hexagonal lattice to minimise their energy. This will be discussed in more detail in section 2.4.

The critical fields $H_{\rm c1}$ and $H_{\rm c2}$ are functions of the temperature and decrease with increasing temperature. In figure 2.3 we show the phase diagram of a type-II superconductor as a function of magnetic field and temperature. At zero temperature, we can estimate $H_{\rm c1} \approx \frac{1}{\kappa} H_{\rm c}$ and $H_{\rm c2} \approx \kappa H_{\rm c}$ (*Kittel*, 1996). For high-temperature-materials, the Ginzburg-Landau parameter is big ($\kappa_{\rm YBCO} \approx 90$ and $\kappa_{\rm BSCCO} \approx 60$) and therefore $H_{\rm c1}$ is much smaller than shown in figure 2.2 and 2.3.

In this work the regime $H \gg H_{c1}$ is investigated and hence $B \approx \mu_0 H$, where μ_0 is the free-space permeability. For convenience both the magnetic field H and the magnetic induction B are referred to as magnetic fields.

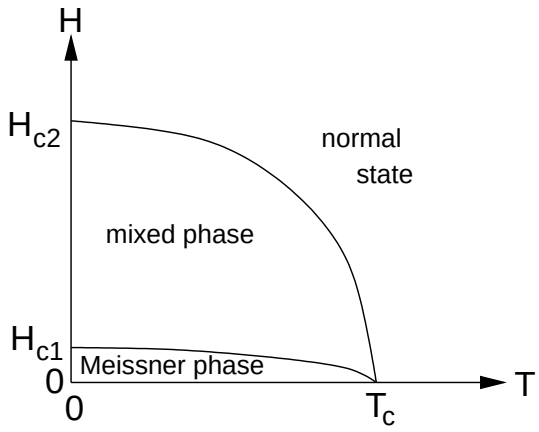

Figure 2.3: Phase diagram of type-II superconductor

2.3 Interactions in the vortex state

2.3.1 Lorentz force and flux flow

In the presence of a transport current, a Lorentz force $\mathbf{f}_\mathrm{L}$ per unit length, proportional to the current density $\mathbf{j}$ acts on the vortices and pushes them in a direction perpendicular to the transport current and perpendicular to the orientation of the magnetic field

$$\mathbf{f}_\mathrm{L} = \mathbf{j} \times \mathbf{\Phi}_0, \tag{2.1}$$

where $\mathbf{\Phi}_0$ is a vector pointing in the direction of the magnetic field with a magnitude of the magnetic flux quantum Φ_0.

For an ideal homogeneous material, *Bardeen and Stephen* (1965) showed that the resulting motion of vortices with velocity v is resisted by a viscous drag force $f_\mathrm{visc} = -\eta_\mathrm{volume} v$ per unit volume with a viscosity coefficient η_volume per unit volume given by

$$\eta_\mathrm{volume} = B^2/\rho_\mathrm{ff} \qquad \text{and} \qquad \rho_\mathrm{ff} \approx \rho_n B/B_{c2}, \tag{2.2}$$

with ρ_ff the flux flow resistivity, ρ_n the normal state resistivity of the material, B the magnetic induction, and B_{c2} the upper critical value of B at which superconductivity breaks down. Equation (2.2) has been confirmed in experiments, for example by *Kunchur et al.* (1993). The normal state resistivity enters the expression because the moving vortices induce local electric fields (due to the magnetic induction changing with time) which act on the unpaired non-superconducting electrons. There is another contribution coming from the change of the Cooper pair density on a time scale comparable to the relaxation time of the Cooper pair system (*Buckel*, 1993, p.181).

If vortices move, they dissipate energy which is taken from the transport current. This manifests itself as a voltage across the material, and in such circumstances the material has a resistance.

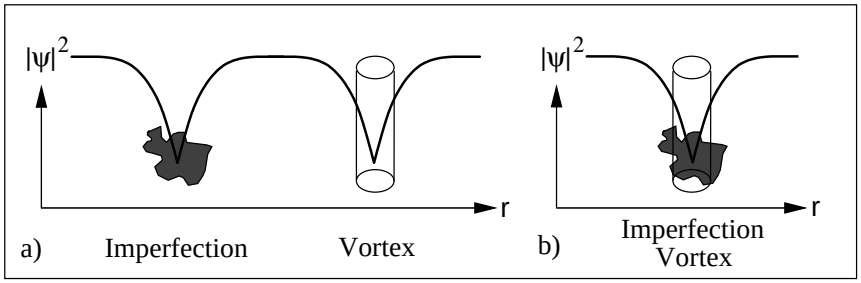

Figure 2.4: a) Schematic plot of the density of Cooper pairs in the neighbourhood of an imperfection in the crystal structure and a vortex. b) If the vortex is placed into the imperfection then the system's energy is reduced.

2.3.2 Pinning

In practice, real materials always have inhomogeneities, which tend to "pin" vortices to the atomic crystal structure. Therefore, for currents below a critical current density, the vortices are pinned and do not respond to a small Lorentz force, so no resistance is measured.

Imperfections in the crystal structure influence the motion of vortices via scattering or the suppression of the superconducting order parameter (*Blatter et al.*, 1994, p.1143). The latter mechanism can be explained qualitatively in terms of the energy contribution of the condensation energy to the superconducting state and is illustrated in figure 2.4. Imperfections in the periodicity of the atomic structure locally inhibit superconductivity. In these areas, there is no negative contribution from the condensation energy to the total energy of the superconducting state. The net reduction in system energy of a vortex in a type-II superconductor is positive, and the core of the vortex is not superconducting. It is therefore energetically advantageous if a vortex is located in an imperfection. Any attempt to move it from there to another position would increase the system energy. For forces which are not too large the vortex is pinned.

There are different kinds of pinning objects in high-temperature superconductors such as $YBa_2Cu_3O_{7-\delta}$ (YBCO). On the atomic scale, there are oxygen vacancies which locally suppress the superconducting order parameter and appear spatially uncorrelated. On the other hand, there are correlated defects such as twin boundaries due to the orthorhombic structure of YBCO which separate domains in which the crystal a- and b-directions interchange roles. These twin planes and other extended defects such as grain boundaries, stacking faults, screw dislocations, and sample surfaces are larger pinning objects and can pin more than one vortex strongly. Finally, using ionising radiation, columnar defects can be created which can also be relatively strong pinning centres if a vortex aligns with the defect.

2.3.3 Vortex-vortex interactions

In addition to the Lorentz force and the pinning interaction a third force acting on vortices is their mutual repulsion.

All high-temperature superconductors known to date, such as YBCO and $Bi_2Sr_2CaCu_2O_8$ (BSCCO), are layered materials, *i.e.* superconducting CuO_2 layers alternate with less superconducting layers. A vortex line can be understood as a coupled line of two-dimensional "pancake" vortices which occupy the CuO_2 layers (*Artemenko and Kruglov*, 1990, *Feigel'man et al.*, 1990, *Buzdin and Feinberg*, 1990, *Clem*, 1991). The following is a short summary of the different kinds of electromagnetic interaction between pancake vortices in single and stacked two-dimensional layers (*Clem*, 1991, *Blatter et al.*, 1994, pp.1277, *Clem*, 1998).

2.3.3.1 Two pancake vortices in an isolated superconducting thin film

The energy $U(r)$ of two pancake vortices separated by a distance $r = \sqrt{x^2 + y^2}$ in a thin film of thickness d is given by Pearl's solution (*Pearl*, 1964)

$$U(r) = \frac{\Phi_0^2 d}{2\pi\mu_0\lambda_s^2}\left(H_0\left(\frac{r}{\Lambda}\right) - Y_0\left(\frac{r}{\Lambda}\right)\right) \tag{2.3}$$

where $\lambda_s \approx 1000\text{Å}$ is the London bulk penetration depth, and $\Lambda = 2\lambda_s^2/d \approx 3 \cdot 10^5\text{Å}$ is the two-dimensional thin film screening length. The quoted numbers are characteristic of an YBCO layer and are given to provide a feel for the order of magnitude of the different lengths. H_0 and Y_0 are the Struve function and the Bessel function of the second kind.

The bulk penetration depth, λ_s relates to the in-plane penetration depth of a thin layer, $\lambda_{ab} \approx 1400\text{Å}$, via $\lambda_s = \lambda_{ab}\sqrt{d/s}$, where $d \approx 6\text{Å}$ is the layer thickness and $s \approx 12\text{Å}$ is the layer spacing. We re-write $\Lambda = 2\lambda_{ab}^2/s$, and introduce

$$\epsilon_0 = \frac{\Phi_0^2}{4\pi\mu_0\lambda_{ab}^2}, \tag{2.4}$$

with $\mu_0 = 4\pi \cdot 10^{-7}\frac{\text{Vs}}{\text{Am}}$ being the vacuum permeability and Φ_0 the magnetic flux quantum. Eventually, we can express the interaction (2.3) strength in terms of ϵ_0

$$U(r) = 2\epsilon_0 s\left(H_0\left(\frac{r}{\Lambda}\right) - Y_0\left(\frac{r}{\Lambda}\right)\right). \tag{2.5}$$

For small and large r, the following approximations hold:

$$U(r) \propto -\ln\left(\tfrac{r}{\Lambda}\right) \quad : \quad r \ll \Lambda \tag{2.6}$$

$$U(r) \propto \tfrac{1}{r} \quad : \quad r \gg \Lambda. \tag{2.7}$$

2.3.3.2 Two pancake vortices in one layer in a system of stacked thin films

Due to induced screening currents in the layers above and below the "central" layer (which holds one pancake vortex), the resulting current distributions are different from those in the isolated thin film. For the repulsive force between two vortices in one layer in an infinite system of stacked layers it has been shown (*Clem*, 1991, eqn. 27) that the interaction force $F(r)$ is given by

$$F(r) = 2\epsilon_0 s \frac{1}{r}\left[1 - \frac{\lambda_{\mathrm{ab}}}{\Lambda}\left(1 - \exp\left(-\frac{r}{\lambda_{\mathrm{ab}}}\right)\right)\right]. \tag{2.8}$$

Since $\lambda_{\mathrm{ab}}/\Lambda \approx 10^{-3}$, this is effectively

$$F_r(r) = \frac{2\epsilon_0 s}{r}. \tag{2.9}$$

This corresponds to a potential

$$U(r) = -2\epsilon_0 s \ln(r) \tag{2.10}$$

which is logarithmic at all distances, not just for $r \ll \Lambda$ as in the isolated thin film (2.6).

For the electromagnetic interaction of two pancake vortices in different layers an attractive force is found that is weaker than the in-layer repulsion by a factor of approximately $\lambda_{\mathrm{ab}}/\Lambda$. We consider this in detail for the studies of three-dimensional pancake systems in chapter 6.

2.3.3.3 Two stacks of aligned pancake vortices

For aligned stacks of pancake vortices where the magnetic field is perpendicular to the superconducting planes as shown in figure 2.5 on the following page, the interaction energy per unit length between two such stacks is found to be

$$U(r) = 2\epsilon_0 K_0\left(\frac{r}{\lambda_{\mathrm{ab}}}\right). \tag{2.11}$$

K_0 is the modified Bessel function of the second kind. Equation (2.11) shows the same r-dependence as the result derived from the London theory for the interaction

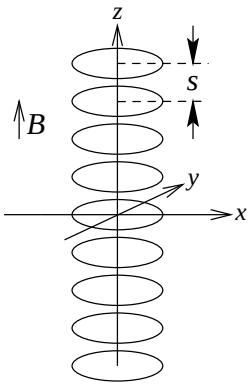

Figure 2.5: A stack of aligned two-dimensional vortex pancakes.

energy of two vortex lines in a continuous medium (*Tinkham*, 1996, p. 154). In the latter result λ_{ab} is given by λ_s, the isotropic London penetration depth. $K_0(r/\lambda_{\mathrm{ab}})$ can be approximated with

$$K_0\left(\frac{r}{\lambda_{\mathrm{ab}}}\right) = \begin{cases} \sqrt{\frac{\pi\lambda}{2r}}\exp\left(-\frac{r}{\lambda_{\mathrm{ab}}}\right) & : \quad r \to \infty \\ \ln\left(\frac{\lambda_{\mathrm{ab}}}{r}\right) + 0.12 & : \quad r \ll \lambda. \end{cases} \tag{2.12}$$

In contrast to equation (2.10) the interaction energy drops off exponentially for large distances. This is due to the weak attraction of pancakes in different layers.

In the remainder of this work, we are dealing with λ_{ab} rather than λ_s. We therefore use $\lambda \equiv \lambda_{\mathrm{ab}}$ to shorten our notation.

The other interaction which is important for vortex pancakes is the Josephson coupling of pancake vortices between different layers. This contribution has to be considered for a complete treatment of layered superconductors (*Clem*, 1991). A theoretical model is given by *Lawrence and Doniach* (1971) which is a discrete version of the Ginzburg-Landau theory. This has been further investigated by *Bulaevskii et al.* (1992) who found that three- and four-body interactions between pancakes have to be considered. However, for this work we will restrict ourselves to the electromagnetic interactions as they alone provide highly complex physics. This is justified in the quasi-two dimensional case of rigid vortices in thin-films and for individual layers of pancakes (chapter 5), and it is a fair first approximation for simulations of three-dimensional loosely coupled materials such as BSCCO (chapter 6).

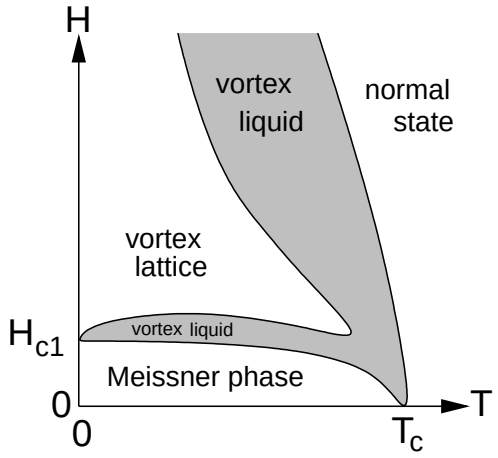

Figure 2.6: The vortex state in the absence of pinning but considering thermal fluctuations. The plot is based on figure 2 from *Blatter et al.* (1994). Large parts of the diagram are occupied by the molten vortex lattice.

2.3.4 Summary

The vortex state is determined by the relative strengths of the following energies:

- the vortex-vortex interaction which favours a hexagonal lattice,
- the vortex-pinning energy which (generally) introduces disorder and
- the thermal energy which destabilises the lattice further.

The Lorentz force drives the system over the pinning energy surface and this results in complex vortex dynamics.

2.4 Static vortex phases

2.4.1 The vortex phases without pinning

We have shown the conventional picture of a clean superconductor (*i.e.* without pinning) in figure 2.3 on page 8: in the Meissner phase the material shows perfect diamagnetism, and between the two critical fields H_{c1} and H_{c2} vortices penetrate the sample and arrange in a hexagonal lattice. On crossing the upper critical field H_{c2} the vortex cores overlap, and the material becomes normal.

If one considers the hexagonally arranged vortices as "vortex matter" than it would be plausible to assume that the vortex crystal could melt at a sufficiently high temperature. This is indeed the case although in conventional superconductors the melting transition line lies so close to the upper critical field line that they are virtually indistinguishable (*Brézin et al.*, 1985). It was first predicted by *Nelson* (1988) that due to the increased importance of thermal fluctuations, the vortex melting transition should be observed to be distinct from the upper critical field line in high temperature superconductors.

We add thermal fluctuations to the phase diagram and show the result in figure 2.6, which is based on figure 2 from *Blatter et al.* (1994). The vortex lattice phase can melt either due to an increase in temperature (in which case thermal fluctuations destroy long-range order), or the vortex lattice can melt due to a decrease of the field. In this case the vortex separation becomes large and the interaction between vortices becomes exponentially weak. This results in a decaying shear-modulus which softens the lattice until it melts. Note that the figure is not drawn to scale in order to emphasise the main structures appearing in the diagram, and that the dilute vortex liquid exists only for a very small range of H. We will not consider the Meissner phase and the re-entrant liquid phase at very low fields $H \approx H_{c1}$ in the remainder of this work.

The position of the melting line can be estimated with a Lindemann[1] criterion (*Blatter et al.*, 1994, 1996, *Vinokur et al.*, 1998), but the nature of the transition cannot easily be determined. The challenge in defining a theoretical scheme describing vortex-lattice melting follows from the complexity of the vortex system in real (three-dimensional) superconductors combined with the general lack of exact theories of melting (*Dodgson et al.*, 2000b). We address this issue in chapter 6 and study the melting transition for a layered system of pancakes that interact electro-magnetically with each other.

2.4.2 The static phases in presence of pinning

The theoretical treatment of a system of vortices under the influence of pinning objects is difficult as it is a many-body problem with competing interactions. Due to the vortex-vortex interaction, the vortices repel each other and try to establish the hexagonal Abrikosov lattice as introduced in section 2.2. At the same time, the underlying pinning potential deforms the vortex lattice such that as many vortices as possible have a low pinning energy. However, this happens at the expense of increasing the vortex lattice elastic energy by deforming it. The equilibrium vortex configuration is the one which minimises the sum of the lattice deformation and the pinning energy.

For random point pinning, *Larkin and Ovchinnikov* (1979) presented their elastic theory of collective pinning which describes the distortion of the flux line lattice in terms of correlation volumes $V_c = R_c^2 L_c$ in which the vortex lattice is reasonably

[1]The empirical Lindemann criterion (*Lindemann*, 1910) assumes that a crystalline lattice becomes unstable with respect to thermal fluctuations of its constitutive elements (atoms, vortex lines, etc.) as the mean-squared amplitude of fluctuations $<u^2>$ increases beyond a certain fraction c_L of the lattice constant a_0: $<u^2(T_m)> \approx c_L^2 a_0^2$, where T_m is the melting temperature. The Lindemann number $c_L \approx 0.1 - 0.2$ depends weakly on the specific material.

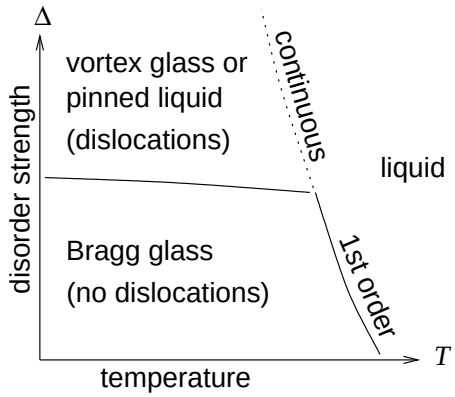

Figure 2.7: Static phase diagram suggested by *Le Doussal and Giamarchi* (1998) for the elastic manifolds in a random potential. The axes show temperature T and the strength Δ of the disordering random potential. This can qualitatively be compared with figure 2.6 on page 13 as the disorder strength Δ relatively increases with the magnetic field (*Vinokur et al.*, 1998).

undistorted. The correlation volume has a length L_c in the field direction and a transverse size of R_c. R_c and L_c are chosen to optimise the trade-off between pinning and elastic energies. One of the main conclusions is that for less than four dimensions any small amount of pinning destroys long-range order.

However, several experimental results were difficult to interpret in this framework. For example Bitter decoration experiments for low fields showed remarkably large regions free of dislocations (*Grier et al.*, 1991). Following work by *Nattermann* (1990), *Giamarchi and Le Doussal* suggested in 1994 that the Larkin-Ovchinnikov argument may be too simple. They studied the related problem of an elastic periodic medium submitted to a random potential (corresponding to uncorrelated pinning), and found that a "Bragg glass" phase could exist for low fields and weak disordering potentials.

2.4.2.1 Three dimensions

Giamarchi and Le Doussal (1994, 1995) used variational and renormalisation group techniques to investigate the statics of periodic elastic manifolds in random potentials, such as vortex lines in superconductors. Following the terminology in the literature, the strength of the random pinning potential is, in short, referred to as "disorder". They obtain the following three distinct phases for line vortices in three dimensions, which are schematically shown in figure 2.7. A dislocation-free phase with algebraically decaying translational order (*i.e.* quasi-long-range order) is predicted to exist for sufficiently weak disorder[2] and temperature. In more detail, the translational order correlation function decays like a power law with distance, whereas for short-range order it decays exponentially and for a solid it becomes constant for large distances. Although there is no true long-range translational order

[2]For large ranges of parameter space it can be shown that the relative strength of the disorder (due to pinning) increases with the magnetic field (*Vinokur et al.*, 1998).

(as for a perfect lattice with δ-Bragg peaks in the structure factor), the quasi-long-range order still allows low order algebraically diverging Bragg peaks to be observed in the structure factor of such a system, and therefore Giamarchi and Le Doussal called this thermodynamic phase the "Bragg glass" phase. In contrast to a glass in which no periodic lattice structure is visible, a Bragg glass appears as a deformed hexagonal lattice, in which all lattice sites have six nearest neighbours. Thus, from a topological point of view, the Bragg glass is much closer to a solid than a glass, in which translational order decays exponentially, and topological order is destroyed. However, it has many meta-stable states and only quasi-long-range translational order.

For higher fields, Giamarchi and Le Doussal predict an order-disorder transition to a "pinned vortex liquid" or a "vortex glass" which contains topological defects, and for temperatures above the melting temperature, a "vortex liquid".

The phase transition from the Bragg glass to the liquid is predicted to be first order, whereas the transition from the vortex glass to a liquid is predicted to be continuous (or second order) (*Giamarchi and Le Doussal*, 1995).

The results as summarised in figure 2.7 seem to be supported by several analytical and numerical studies and compare well with the most recent experiments (for example *Kokkaliaris et al.*, 1999, *Klein et al.*, 2001, and references [47-52] in *Le Doussal and Giamarchi*, 1998).

Vinokur et al. (1998) obtained a similar phase diagram using an extended Lindemann criterion, where the Bragg glass is referred to as a "quasi-lattice" and the vortex glass is referred to as an "entangled solid". The same orders for the phase transitions are suggested.

2.4.2.2 Two dimensions

The general theoretical belief based on qualitative arguments and simulations (*Shi and Berlinsky*, 1991, *Blatter et al.*, 1994, Sec.VIII.D.3) is that no solid phase with long-range order exists in two dimensions at finite temperatures in the presence of disorder. However, signatures of melting were observed in experiments in two-dimensional regimes (*Yazdani et al.*, 1994, *Theunissen et al.*, 1996) although on large length scales there was no order (*Yazdani et al.*, 1993). This can be explained by the results of recent theoretical investigations by *Carpentier and Le Doussal* (1998) and *Le Doussal and Giamarchi* (2000) who found that below a length scale ξ_D the Bragg glass is stable and that ξ_D can become arbitrarily large for weak disorder and low temperatures. On the other hand, it is not even clear whether the assumptions underlying the theoretical models overestimate the relevance of

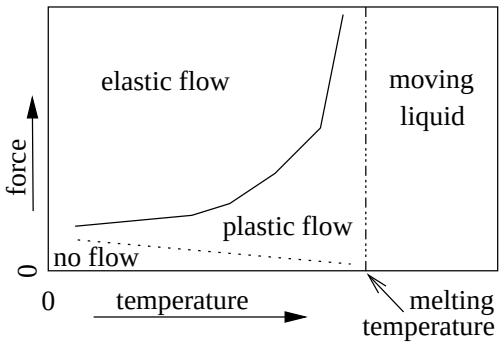

Figure 2.8: Schematic representation of the results of *Koshelev and Vinokur* (1994) on the dynamic phase diagram for a system with a fixed magnetic field and varying Lorentz force and temperature.

topological defects (*Giamarchi and Le Doussal*, 1998, Sec.3.5) and there may be a two-dimensional Bragg glass phase for all length scales.

In summary, there is some evidence that the two-dimensional Bragg glass phase exists only up to certain length scales, ξ_D, and not for infinitely large systems, but the existence of the two-dimensional Bragg glass phase is a subtle issue which cannot be answered definitely today. However, in either case the two-dimensional situation is of physical interest, since ξ_D can be large and, apart from thin-film superconductors, other two-dimensional physical systems exist such as Wigner crystals (*Andrei et al.*, 1988) and magnetic bubble arrays (*Seshadri and Westervelt*, 1992) which very likely can be described in the same theoretical framework.

2.5 Dynamic vortex phases

Due to the competing interactions (see section 2.3) in the vortex state, vortices display not only a rich static phase diagram. Also, when being driven by a Lorentz force in the presence of pinning, a wide range of dynamical behaviour can be observed, including avalanches, stick-slip dynamics, thresholds for motion, nonlinear and hysteretic response, and plastic and elastic motion.

An important early step concerning the dynamics of the vortex state was made by *Koshelev and Vinokur* (1994). Using a molecular dynamics simulation of the two-dimensional vortex state, they found the "dynamic phase diagram" shown in figure 2.8. Applying a force to a pinned system of vortices below the melting temperature of the system results in plastic flow as soon as a critical depinning force (dotted line) is reached. The term "plastic flow" is defined such that the nearest neighbours of one vortex change in time. In contrast, after reaching a second critical force (solid line), the whole system of vortices shows "elastic flow", where the nearest neighbours stay the same and the vortices move together in a coordinated manner. With increasing temperature, the system becomes depinned

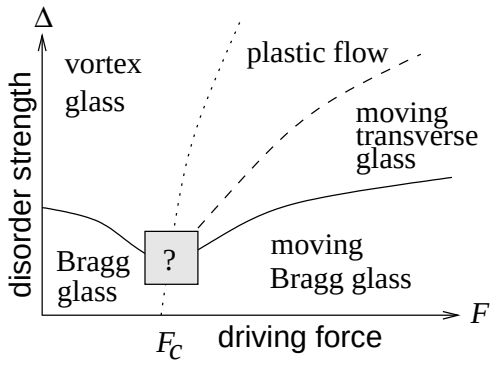

Figure 2.9: Schematic representation of the phase diagram for three-dimensional systems suggested by *Le Doussal and Giamarchi* (1998) as a function of disorder strength Δ and driving force F (at zero temperature). For weak disorder and a weak driving force, a pinned Bragg glass phase with quasi-long-range translational order is expected. For larger driving forces, this depins and becomes a moving Bragg glass. With increasing disorder at low driving forces, the system transforms into a pinned vortex glass (with topological defects and short-range order only). Increasing the driving force from the vortex glass regime results in first plastic flow, then motion in decoupled channels (the moving transverse glass) and for the largest driving forces, a moving Bragg glass is recovered, in which the separate channels couple. F_c denotes the depinning force. There are no predictions for the behaviour within the regime of the grey box.

more easily and the plastic flow regime extends to larger forces. If the temperature is higher than the melting temperature, the system behaves as a liquid.

For larger driving forces Koshelev and Vinokur observed a dynamical ordering of the system which is in agreement with other simulation results (*Shi and Berlinsky*, 1991, *Olson et al.*, 1998b). They also predicted the existence of a dynamic phase transition at some characteristic "crystallisation" current. The underlying argument was that for a strongly driven system the pinning potential is felt as a random force and that this can be expressed as an effective "shaking temperature" which is inversely related to the velocity of the system. For large enough driving forces the system is predicted to crystallise into a perfect lattice.

Recently *Giamarchi and Le Doussal* (1996) extended their description of the statics of the vortex state to the dynamics, predicting a "moving" Bragg glass. Shortly afterwards, *Balents et al.* (1997) commented on Giamarchi and Le Doussal's publication, predicting that, in addition to the moving Bragg glass, a moving "smectic" should exist. They later detailed this (*Balents et al.*, 1998), and their ideas contributed to the detailed work of *Le Doussal and Giamarchi* (1998).

2.5.1 Three dimensions

Figure 2.9 shows a schematic sketch of the dynamic phase diagram suggested by *Le Doussal and Giamarchi* (1998) as a function of disorder strength Δ and driving

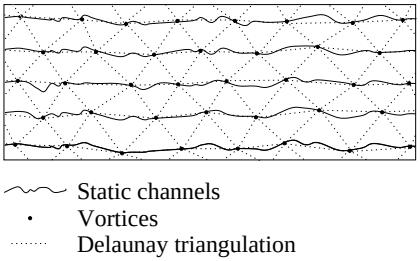

Figure 2.10: The moving Bragg glass. A driving force is acting horizontally from left to right. Vortices move along static channels like beads on a string. Vortices in different channels are coupled and move with the same average velocity in the horizontal direction. There are no dislocations in the system.

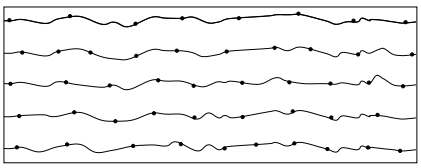

Figure 2.11: The moving transverse glass. Vortices move in static channels, but vortices in different channels can move with different velocities. The channels are decoupled, and dislocations between different channels exist.

force F (at zero temperature). For low disorder and weak driving forces the system is expected to be pinned and to form a Bragg glass as described in the static case (section 2.4.2.1). For stronger disorder it is expected to be pinned as a disordered vortex glass, as in the static case. Increasing the driving force in this regime leads to a plastic flow phase where vortices move more or less independently of their neighbours. For further increases of the driving force, a moving transverse glass phase and moving Bragg glass phase are predicted to exist.

2.5.1.1 The moving Bragg glass

For weak disorder or large enough driving forces, a new dynamic phase is predicted to exist: the "moving Bragg glass". It is shown schematically in figure 2.10. The figure shows a two-dimensional cross section of vortex lines, such that each vortex line is represented by a point. A driving force is acting in the horizontal direction. The hexagonal vortex system which is free of dislocations is indicated by the dotted lines connecting nearest neighbours. The vortices move along "static channels" in the direction of the driving force, which are represented by the solid lines in the figure. This motion of vortices in the channels is analogous to beads moving on a string. The static channels are determined by the static disorder and do not fluctuate in time. They can be visualised in experiments or simulations by superimposing vortex position images at different times. The channels are the easiest paths for the vortices to flow, and are determined by a subtle competition between elastic energy, disorder and dissipation. The channels are correlated in the vertical direction (perpendicular to the driving force direction), and they are predicted to be "rough". This roughness is in contrast to the prediction of *Koshelev and Vinokur* (1994) in which straight lines are expected for the vortex paths for high driving forces. In the moving Bragg glass regime, the vortices in the different

static channels move with the same average velocity in the direction of the driving force, and the system retains topological order.

2.5.1.2 The moving transverse glass

In contrast, for smaller driving forces or stronger disorder the "moving transverse glass" is expected, as sketched in figure 2.11 and first predicted by *Balents et al.* (1997). Vortices move along static channels, but the motion between different channels is not necessarily coupled. The average horizontal velocity can vary from static channel to static channel such that phase-slips may occur, and thus there can be topological defects between two channels moving with different velocities. It is expected in the moving transverse glass that channels are coupled up to a certain length (perpendicular to the channel orientation), and that phase slips occur between chunks of such coupled channels. The length scale of coupled channels increases with the driving force and decreases with the disorder strengths. In the limit of small pinning or large driving forces, consequently, all channels are coupled, and the moving Bragg glass is recovered.

In terms of "dynamic Larkin domains" (over which the vortices form a relatively undisturbed lattice) in the drifting vortex system, the moving transverse glass is due to a strong anisotropy in the Larkin lengths, $R_c^{\parallel}$-parallel to the driving direction and $R_c^{\perp}$-perpendicular to the direction of the driving force (*Le Doussal and Giamarchi*, 1998, *Scheidl and Vinokur*, 1998).

Different names for the Moving Bragg Glass (MBG) and the Moving Transverse Glass (MTG) are in common use: in the work of *Balents et al.* (1998) the moving Bragg glass is termed "moving lattice", and the moving transverse glass is called a "moving smectic". *Scheidl and Vinokur* (1998) came to similar conclusions for the dynamic phase diagram as *Balents et al.* (1998) and *Le Doussal and Giamarchi* (1998) using a perturbative approach, and call the moving Bragg glass "coherent phase" and the moving transverse glass "decoupled channels".

2.5.2 Two dimensions

In two dimensions it is not clear whether the moving Bragg glass exists as a stable phase. It seems more likely (*Balents et al.*, 1998, *Le Doussal and Giamarchi*, 1998) that the moving transverse glass is the only stable phase, although motion of vortices in different channels could still couple at high enough driving forces (*Le Doussal*, 1999). If one assumes that there is no topologically ordered phase in two dimensions in the static case (see section 2.4.2.2), then the dynamic two-dimensional phase diagram is supposed to look like figure 2.12, and so there is no pinned topologically

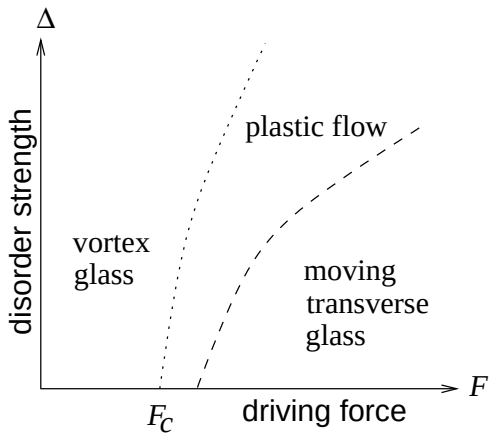

Figure 2.12: Schematic representation of the phase diagram for two-dimensional systems suggested by *Le Doussal and Giamarchi* (1998) as a function of disorder strength Δ and driving force F (at zero temperature). It has been assumed that there is no topologically ordered static phase for finite disorder strength and zero driving force. Whether there is a moving Bragg glass phase at large driving forces (in which the decoupled channels of the moving transverse glass couple) is currently not known. No such phase is shown in this figure.

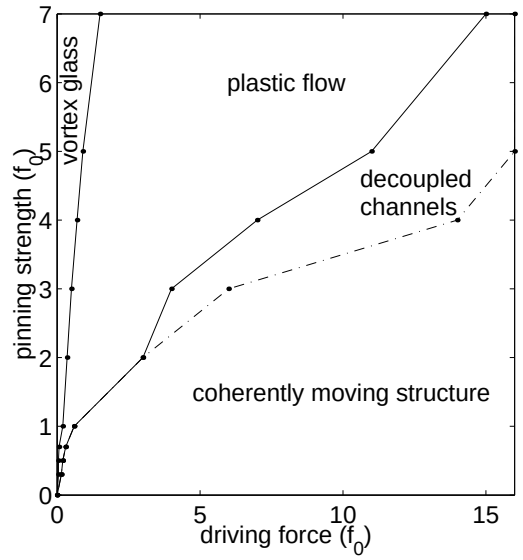

Figure 2.13: Numerically obtained dynamic phase diagram for a two-dimensional vortex-system (*Fangohr et al.*, 2001a).

ordered state for any finite disorder strength. Above the depinning driving force, F_c, highly filamentary plastic flow is expected at first, which transforms into a moving transverse glass for even higher driving forces. Whether the decoupled static channels that constitute the moving transverse glass couple for large velocities cannot be decided at present. In the figure no such moving Bragg glass phase is shown.

Recent two-dimensional Langevin dynamics simulations (*Olson et al.*, 1998b, *Fangohr et al.*, 2001a) provide phase-diagrams of the dynamic vortex state which are qualitatively in agreement with figure 2.9 on page 18, for example the data shown in figure 2.13: there is a vortex glass and a plastic flow phase, the decoupled channels represent the moving transverse glass phase, and the coherently moving structure corresponds to the moving Bragg glass phase. The physics at the smallest pinning strength could not be resolved here: it is not clear whether there is a static Bragg glass phase at the smallest pinning strengths. The coherently moving

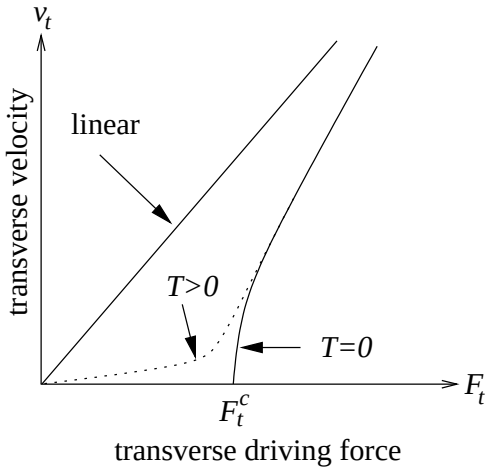

Figure 2.14: Schematic representation of the transverse current-voltage relation predicted by *Le Doussal and Giamarchi* (1998) for the moving glass. Shown is the velocity v_t transverse to the main direction of motion as a function of a transverse driving force F_t. At zero temperature the system does not respond to transverse driving forces $F_t < F_t^c$ below a critical transverse force F_t^c. For finite temperature a linear response in velocity is expected for finite and small transverse driving forces, as shown by the dotted line. For F_t near F_t^c the finite temperature curve approaches the zero-temperature curve.

structure could be a moving Bragg glass, or it could be the decoupled channel regime in which the channels are so broad that they cover the complete simulation cell. Thus, it cannot be decided whether the numerical data from a two-dimensional simulation correspond more closely to the three-dimensional prediction (figure 2.9) or the two-dimensional prediction (figure 2.12 on the preceding page). However, the existence of the moving glass phase is confirmed.

2.6 The critical transverse force

Giamarchi and Le Doussal (1996) found that for the moving glass there should be a finite transverse barrier for a system moving along one of its principal axes at zero temperature. To investigate this, one drives a system in the moving glass regime, where it is moving along a principal lattice axis. Once a steady state has been found and the rough time-independent channels have developed, one applies a small driving force transverse to the direction of motion. Experimentally, this can be achieved by applying a small second current transverse to the first current which drives the system. It is predicted that for small enough transverse driving forces the system does not leave the static channels. Only for transverse forces exceeding a critical force, does the system start to move transversely. The expected transverse current–transverse voltage (or equivalently transverse driving force–transverse velocity) relation is shown figure 2.14.

For zero temperature, it is expected that the system responds non-analytically to a transverse driving force, such that it is only transversally depinned for transverse driving forces larger than the critical transverse driving force. In contrast, for finite temperature the transverse current-voltage characteristic starts for small transverse driving forces with a linear response in transverse velocity with a small slope, which depends on the longitudinal velocity of the system. For transverse driving forces

near to the zero temperature critical transverse force, the curve approaches the zero-temperature curve.

The transverse critical force is a rather subtle effect, even more so than the usual longitudinal critical force. It does not exist for a single particle in a random potential, although a single particle does experience a non-zero longitudinal critical force. The transverse critical force is a dynamical effect due to barriers preventing the channels re-orienting. The transverse critical force has been proposed to be the order parameter of the moving glass phase at zero temperature (*Le Doussal and Giamarchi*, 1998). If there is a transverse critical force in a moving state, then there should be a history dependence in the system.

In numerical work, a critical transverse driving force has been found in two dimensions (*Ryu et al.*, 1996, *Moon et al.*, 1996, *Olson and Reichhardt*, 2000), but to the best of our knowledge, no such experimental results have been published yet. We address the critical transverse force in chapter 5.

2.7 Summary

The theoretical models introduced here (*Giamarchi and Le Doussal*, 1996, *Balents et al.*, 1998, *Le Doussal and Giamarchi*, 1998, *Scheidl and Vinokur*, 1998) are the best description of the statics and dynamics of the vortex state currently available and increasingly experimental data are interpreted within these frameworks. However, there are many open questions within these models which cannot be answered analytically, but have to be investigated experimentally and numerically.

2.8 Applications

Apart from a strong interest in basic research in the (non-equilibrium) statistical mechanics of (driven) systems with quenched disorder, there is a wide range of practical applications of high-temperature superconductivity which are currently used or could be very useful in the future.

Macroscopic superconducting devices are nowadays mainly used to provide strong magnetic fields for various applications such as medical magnetic resonance imaging (MRI) machines, and for particle accelerators. There are applications such as non-exploding fault current limiters and superconducting voltage transformers in the electric power industry.

From a practical point of view, the main challenge is to increase the critical current in the high-temperature superconductors. The current-carrying capabilities

are determined by the behaviour of vortex lines, and that is the physical system under investigation in this thesis.

On a much smaller scale superconducting filters have very high Q-values and improve bandwidths and selectivity of telecommunication receivers. Finally, superconducting quantum interference devices (SQUIDs) are used to detect magnetic fields of strengths of a few femto-tesla. This allows magneto encephalography (MEG) measurements of the magnetic fields generated by electric currents in human brains. Another application of these highly sensitive sensors is non-destructive evaluation (NDE) of aeroplane wings, wheels and rivets.

Other possible applications of superconductors include high-power cables, magnetic levitation, energy storage, very fast digital components and the use of superconducting Josephson junctions to construct qubits for quantum computing. However, these examples are not practically or economically feasible at the present time.

Chapter 3

The Simulation

This chapter describes the computer simulation that has been developed and used for this work. The central idea is to represent vortices as massless classical particles that are free to move in a two-dimensional area. Those particles can be identified with vortex-lines when modelling thin films in which vortices are "stiff". To model three-dimensional systems we associate these particles with pancake-vortices, and use a mean field approach (chapter 6) to account for interactions in the third dimension.

In section 3.1, an overview of techniques to simulate many-body problems is given and in section 3.2 these techniques are related to the vortex state, followed by a detailed description of the simulation software. This includes the derivation of the central equations of motion in section 3.3 and methods to solve them (section 3.4). In sections 3.5 we describe the boundary conditions and section 3.6 details our choice of simulation units. Section 3.7 assesses the applicability of the model, and in section 3.8 the observables to monitor the simulation are introduced. Section 3.9 concentrates on practical aspects of the usage of the simulation software such as the user interface, and hardware and software requirements. A summary is provided in section 3.10.

3.1 Computer simulations of many-body systems

Computer simulations have proved to be a valuable tool for problems that cannot be solved analytically. Numerical solutions are particularly useful for providing results for specific parameters which are not at all obtainable otherwise.

Following *Haile* (1997), the simulations used to study many-particle problems can be ordered from stochastic simulations to deterministic models as shown in figure 3.1 on the next page.

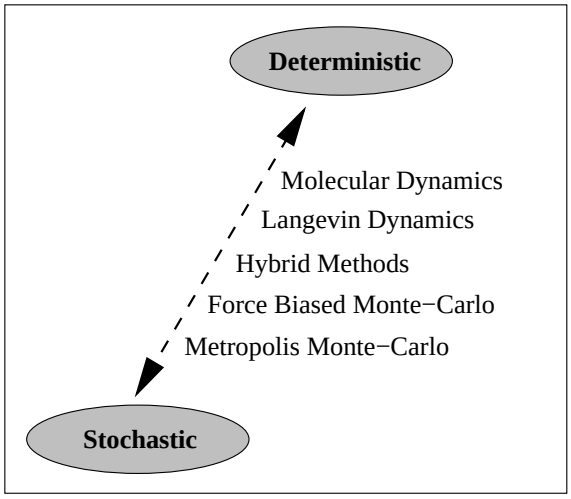

Figure 3.1: Monte Carlo simulations work stochastically and molecular dynamics simulations work deterministically. There are various techniques that combine both methods.

Monte Carlo simulations are adopted from general Monte Carlo methods for solving high-dimensional integrals. In Monte Carlo simulations the integrals of interest are the statistical mechanics ensemble averages for a property $f(\mathbf{r}^N)$, for example in the canonical ensemble:

$$< f >= \frac{\int \dots \int \, \mathrm{d}\mathbf{r_1}\, \mathrm{d}\mathbf{r_2} \dots \mathrm{d}\mathbf{r_N} \;\; f\left(\mathbf{r}^N\right) \, \exp\left(-\frac{U(\mathbf{r}^N)}{k_\mathrm{B}T}\right)}{\int \dots \int \, \mathrm{d}\mathbf{r_1}\, \mathrm{d}\mathbf{r_2} \dots \mathrm{d}\mathbf{r_N} \;\; \exp\left(-\frac{U(\mathbf{r}^N)}{k_\mathrm{B}T}\right)}. \tag{3.1}$$

This is the standard case where the number of particles N, the temperature T, and the volume V of the simulation are given. The vector $\mathbf{r}^N$ has Nd components when each particle's position $\mathbf{r}_i$ has d components, and $U(\mathbf{r}^N)$ is the energy of the system. Since Monte Carlo methods are generally not well suited to study dynamical quantities, the integration in phase space over the generalised momenta $\mathbf{p}_1, \dots, \mathbf{p}_N$ has been carried out already in equation (3.1).

Taking the Boltzmann factor $\exp\left(-\frac{U(\mathbf{r}^N)}{k_\mathrm{B}T}\right)$ into account, it was suggested by *Metropolis et al.* (1953) to consider only configurations which contribute most to the integral. This is known as importance sampling for general Monte Carlo methods and in the context of Monte Carlo simulations it is referred to as the "Metropolis algorithm".

Particle positions are altered by trial moves which are conditionally accepted. Each new configuration depends only on the previous one and is achieved by moving one particle a small distance to a new position which is determined by a random number generator. The configurations encountered in the run of a simulation are obtained stochastically.

Molecular dynamics methods can be divided into equilibrium and non-equilibrium dynamics. Equilibrium dynamics are usually applied in the micro-canonical ensemble to an isolated system with energy E, containing a fixed number of particles N, in a fixed volume V. However, there exist methods to fix the simulated temperature, which allows investigation of canonical ensembles (for example *Rapaport*, 1995). In non-equilibrium molecular dynamics, an external force is applied to the system to establish non-equilibrium situations of interest. The particles' positions are obtained by integrating Newton's equation of motion. For a set of N particles with positions $\mathbf{r}_i$, the set of equations to solve reads[1]

$$m_i \ddot{\mathbf{r}}_i = \mathbf{F}_i \left(\mathbf{r}_{1,\ldots,N}, \dot{\mathbf{r}}_{1,\ldots,N}, t \right) \qquad \text{i} = 1, \ldots, \text{N}, \tag{3.2}$$

where m_i is the mass of particle i, and $\mathbf{F}_i$ is the total force acting on i. The velocity of particle i is $\dot{\mathbf{r}}_i$ and $\ddot{\mathbf{r}}_i$ is its acceleration.

To compute a system property $f(\mathbf{r}^N, \dot{\mathbf{r}}^N)$, one takes the time average of that property

$$< f >= \lim_{t \to \infty} \frac{1}{t} \int_{t_0}^{t_0+t} \mathrm{d}t' \; f\left(\mathbf{r}^N(t'), \dot{\mathbf{r}}^N(t') \right). \tag{3.3}$$

In contrast to the Monte Carlo simulations, it is here easily possible to investigate dynamical quantities such as transport coefficients and time correlation functions. According to the ergodicity hypothesis the ensemble average in equation (3.1) and the time average in equation (3.3) should be the same.

Force biased Monte Carlo methods compute the force exerted from all other particles on particle i and then move that particle i in this direction. This reduces the number of trial moves required, but each sweep is computationally more expensive.

Hybrid methods are Monte Carlo simulations that use a sequence of molecular dynamics steps to generate new random configurations. This ensures that very different areas in phase space are covered and reduces the number of Monte Carlo sweeps required to study equilibrium properties of the system.

Langevin dynamics were developed to investigate Brownian Motion (*Lenk and Gellert*, 1989, p.537). One studies particles immersed in a continuum, for example a fluid. Instead of considering all microscopic interactions of all particles establishing the fluid, one concentrates on one particle and its interactions with the continuum. The force exerted on the particle by the fluid is broken into two parts: an average

[1] The following convention is used: the dot notation represents the time derivative: $\dot{\mathbf{r}} = \frac{\mathrm{d}\mathbf{r}}{\mathrm{d}t}$ and $\ddot{\mathbf{r}} = \frac{\mathrm{d}^2\mathbf{r}}{\mathrm{d}t^2}$.

viscous force $-\eta\dot{\mathbf{r}}_i$ and a random force $\boldsymbol{\chi}(t)$ whose time average is zero (*Kubo et al.*, 1985, p.14). The equation of motion for particle i is

$$m_i\ddot{\mathbf{r}}_i = -\eta\dot{\mathbf{r}}_i + \boldsymbol{\chi}_i + \mathbf{F}'_i, \tag{3.4}$$

where $\mathbf{F}'_i$ represents all forces not covered in the other two terms. The macroscopic frictional force represents an averaged value of many microscopic interactions. In cases where inertial effects are small, the mass m_i of the particles can be set to zero. That reduces the system of differential equations of second order in (3.4) to a system of first order equations which are occasionally referred to as the "overdamped" Langevin equations of motion because the absence of the inertial term causes the motion to be overdamped.

3.2 Methods to simulate the vortex state

The most direct method to investigate the vortex state is to solve the (time-dependent) Ginzburg-Landau differential equations numerically to obtain solutions for the complex valued order parameter ψ and the magnetic vector potential. The set of coupled non-linear partial differential equations can be solved on a discrete grid, as demonstrated for example by *Braun et al.* (1996), *Gropp et al.* (1996) and *Aranson and Vinokur* (1998). On the one hand this approach does not simplify the physical situation, but on the other hand it is computationally very demanding since it requires many grid points to resolve even a single vortex.

Another starting point is to treat vortices as structureless point- or string-like objects. Each of the areas in which the superconducting order parameter ψ drops to zero is mapped to such an object, which is then considered as being a classical particle. To compute the interactions between these classical particles one uses effective interaction potentials (for example *Clem*, 1991, *Bulaevskii et al.*, 1992). The price which has to be paid for decreasing the computational complexity is that the small length scale ξ is lost and phenomena like pinning, vortex-anti-vortex creation or flux cutting do not come intrinsically with these models, but have to be implemented by other means. To study the statics of the vortex state, Monte Carlo simulations can be used (for example *Täuber and Nelson*, 1995, *Yates et al.*, 1995, *Ryu and Stroud*, 1996), whereas to study the dynamics, Langevin dynamics methods are required (for example *Brass et al.*, 1989, *Koshelev and Vinokur*, 1994, *Grønbech-Jensen et al.*, 1996, *Groth et al.*, 1996, *Moon et al.*, 1996, *Ryu et al.*, 1996, *Spencer and Jensen*, 1997, *Olson et al.*, 1998a, *Wilkin and Jensen*, 1997b,a,

van Otterlo et al., 1998, *Kohandel and Kardar*, 1999). Here, we follow this approach and use Langevin dynamics to study the static and dynamic behaviour of vortices.

Parts of this work are applicable to particle simulations in general and not limited to vortex state simulations. Therefore, we frequently use the term "particle" instead of "vortex".

In addition to the methods described above, there are other approaches to simulate the physics of the vortex state. These range from xy-models (for example *Li and Teitel*, 1994, *Nguyen and Sudbø*, 1999) to the solving of a coarse grained equation of motion for the displacement field (*Aranson et al.*, 1998), investigating a disordered array of Josephson junctions (for example *Domínguez*, 1999), mapping vortex lines to bosons (for example *Nordborg and Blatter*, 1997) and combination of methods, such as the London-Langevin method coupled to solving the time-dependent Ginzburg-Landau equation (*Bou-Diab et al.*, 2001).

3.3 Equation of motion

The terms in the equation of motion that influence the behaviour of each vortex are the viscous force and a stochastic term from the Langevin equation (3.4), the vortex-vortex interaction, the Lorentz force, and pinning forces. Each of these will be presented in detail in the following subsections.

3.3.1 Overdamped Langevin dynamics

The Langevin dynamics as introduced in section 3.1 form the physical basis of this simulation. The flux motion is strongly overdamped since the viscous force is much greater than any possible inertial forces (*Brandt*, 1995, Sec. 5.2) and the vortex mass can be ignored. The mass term m_i on the left-hand side of equation (3.4) is set to zero and the remaining Langevin equation for vortex i reads (with $\boldsymbol{\chi}_i = \mathbf{F}_i^{\text{thermal}}$):

$$0 = -\eta\dot{\mathbf{r}}_i(t) + \mathbf{F}_i^{\text{vv-interaction}}(\mathbf{r}_1(t), \ldots, \mathbf{r}_N(t)) + \mathbf{F}^{\text{drive}}(t) + \mathbf{F}_i^{\text{thermal}}(t) + \mathbf{F}^{\text{pinning}}(\mathbf{r}_i(t)). \tag{3.5}$$

The terms represent from left to right: the viscosity term, the forces from the vortex-vortex interaction, the drive or Lorentz force acting on all vortices equally, the noise term which introduces temperature, and the pinning force which depends on the position of the vortex.

3.3.2 Viscosity

The viscosity, η, of the vortex state is related to the Bardeen-Stephen expression for flux-flow resistivity in a homogeneous material (see section 2.3.1 on page 8). The

viscous drag coefficient per volume is

$$\eta_{\text{volume}} \approx \frac{BB_{c2}}{\rho_n}. \tag{3.6}$$

Considering that the magnetic induction, B, is represented by N vortices, each carrying a flux quantum Φ_0 over the area A, leads to $B = N\Phi_0/A$. Equation (3.6) can be converted into the viscosity per vortex per unit length $\eta^1_{\text{length}} = \frac{\eta_{\text{volume}}}{N} A \approx \frac{\Phi_0 B_{c2}}{\rho_n}$. The viscosity η in equation (3.5) is given by the viscosity per (pancake) vortex which for a (pancake) vortex of length s is

$$\eta = \eta^1_{\text{length}} s = \frac{\Phi_0 B_{c2}}{\rho_n} s. \tag{3.7}$$

3.3.3 Vortex-vortex interaction

The energy U and force F per unit length of interacting stiff vortex lines separated by a distance r is (see section 2.3.3)

$$U_{\text{line}}(r) = 2\epsilon_0 K_0\left(\frac{r}{\lambda}\right) \qquad \Longleftrightarrow \qquad F_{\text{line}}(r) = \frac{2\epsilon_0}{\lambda} K_1\left(\frac{r}{\lambda}\right) \tag{3.8}$$

and the interaction energy and force between pancakes in the same layer is effectively (see section 6.2 for details)

$$U_{\text{pancake}}(r) = 2\epsilon_0 s \ln\left(\frac{\lambda}{r}\right) \qquad \Longleftrightarrow \qquad F_{\text{pancake}}(r) = \frac{2s\epsilon_0}{\lambda}\frac{1}{r} \tag{3.9}$$

where $\epsilon_0 = \frac{\Phi_0^2}{4\pi\mu_0\lambda^2}$, λ is the London penetration depth, and s is the layer separation.

For simulations of isolated thin-films, the vortex-vortex interaction is given by Pearl's solution (2.3).

We have implemented all three relevant interactions ($\ln, K_0$ and Pearl's solution), and the interaction potential can be chosen in the configuration file (section 3.9.2.1). We use the smooth cut-off as described in chapter 4 to overcome problems resulting from truncating the interaction.

Using, for example the logarithmic interaction potential (3.9), the vortex-vortex interaction force $\mathbf{F}^{\text{vv}}_{ij}$ felt by pancake i from pancake j at positions $\mathbf{r}_i$ and $\mathbf{r}_j$, respectively, reads

$$\mathbf{F}^{\text{vv}}_{ij}(\mathbf{r}_i - \mathbf{r}_j) = 2\epsilon_0 s \frac{1}{|\mathbf{r}_i - \mathbf{r}_j|}\frac{\mathbf{r}_i - \mathbf{r}_j}{|\mathbf{r}_i - \mathbf{r}_j|} = 2\epsilon_0 s \frac{\mathbf{r}_i - \mathbf{r}_j}{|\mathbf{r}_i - \mathbf{r}_j|^2}, \qquad i \neq j. \tag{3.10}$$

Antisymmetry of $\mathbf{F}^{\mathrm{vv}}$ can be used to optimise its computation. The total force acting on pancake i is given by

$$\mathbf{F}_i^{\mathrm{vv-interaction}} = \sum_{\substack{j=1 \\ j \neq i}}^{N} \mathbf{F}_{ij}^{\mathrm{vv}}(\mathbf{r}_i - \mathbf{r}_j). \tag{3.11}$$

For practical computation, the chosen boundary conditions and a cut-off must be taken into account, as explained in section 3.5.

3.3.4 Lorentz force

The Lorentz force per unit length $\mathbf{f}_{\mathrm{L}} = \mathbf{j} \times \mathbf{\Phi}_0$ acts equally on every vortex (assuming a homogeneous current density). Symbols are as in equation (2.1). The Lorentz force acting on vortices of length s is given by

$$\mathbf{F}^{\mathrm{drive}}(t) = s\,\mathbf{j} \times \mathbf{\Phi}_0. \tag{3.12}$$

3.3.5 Temperature

The thermal motion of a particle i in equilibrium overdamped Langevin dynamics (section 3.3.1) described by

$$0 = -\eta \dot{\mathbf{r}}_{\mathbf{i}} + \zeta_i(t) \tag{3.13}$$

is given by a stochastic noise term which, for clarity, is here called $\zeta_i(t)$ to distinguish it from $\chi_i(t)$ which is used in the simulation. $\zeta_i(t)$ must be normally distributed and have the properties (*Chaikin and Lubensky*, 1995, p.381)

$$< \zeta_i(t) > \; = \; 0 \tag{3.14}$$

and

$$< \zeta_i(t)\zeta_j(t') > \; = \; 2\eta k_{\mathrm{B}} T \delta_{ij} \delta(t - t') \tag{3.15}$$

where η is the viscosity as in equation (3.13), k_{B} the Boltzmann number and T the effective temperature in Kelvin. The angular brackets indicate time-averages in the context of Langevin simulations. Thus, the average of the force from the noise term acting on each particle is zero, and it is neither correlated in time, nor for different particles.

The noise term, χ, chosen in the simulation is

$$\chi(t) = \sigma \Psi \tag{3.16}$$

where $\Psi(t)$ is normally distributed with variance 1.0 with σ as a measure of temperature. It follows that

$$< \chi^2 > = \sigma^2. \tag{3.17}$$

To relate σ to the effective temperature, T, one has to consider that the differential equation of motion is solved discretised in time. This means that high-frequency components of the stochastic term, $\zeta(t)$, are ignored and that $\chi(n\Delta t)$, $n \in \mathbb{N}$, represents the average of $\zeta(t)$ over a time step Δt. Therefore, one has to consider the correlations of the impulses rather than the forces ζ and χ:

$$\begin{aligned}\left\langle \int_t^{t+\Delta t} \int_{t'}^{t'+\Delta t} \zeta(t)\zeta(t')\mathrm{d}t\mathrm{d}t' \right\rangle &= \int_t^{t+\Delta t} \int_{t'}^{t'+\Delta t} < \zeta(t)\zeta(t') > \mathrm{d}t\mathrm{d}t' \\ &\overset{(3.15)}{=} \int_t^{t+\Delta t} \int_{t'}^{t'+\Delta t} 2\eta k_\mathrm{B} T \delta(t-t')\mathrm{d}t\mathrm{d}t' \\ &= 2\eta k_\mathrm{B} T \int_t^{t+\Delta t} \mathrm{d}t \quad = \quad 2\eta k_\mathrm{B} T \Delta t \end{aligned} \tag{3.18}$$

and for χ we obtain $\left\langle \int_t^{t+\Delta t} \int_{t'}^{t'+\Delta t} \chi^2 \mathrm{d}t\mathrm{d}t' \right\rangle \overset{(3.17)}{=} \sigma^2 (\Delta t)^2$. Now the last two expressions can be equated to relate the effective temperature, T, to the temperature parameter, σ, in the simulation:

$$T = \frac{\Delta t}{2\eta k_\mathrm{B}} \sigma^2. \tag{3.19}$$

We will later express forces in multiples of $f_0 \overset{(3.32)}{=} 2\epsilon_0 s / L_\mathrm{scale}$ and the time-step Δt in units of $t_\mathrm{scale} \overset{(3.35)}{=} L_\mathrm{scale}\eta / f_0$ and denote dimensionless parameters with a tilde (section 3.6). Eventually we use $\sigma = \sqrt{\tilde{T}} f_0$ where $\tilde{T}$ is the dimensionless temperature parameter in the simulation, and relates to the real temperature, T, via

$$T = \frac{\Delta t f_0^2}{2\eta k_\mathrm{B}} \tilde{T} = \frac{t_\mathrm{scale} \widetilde{\Delta t} f_0^2}{2\eta k_\mathrm{B}} \tilde{T} \overset{(3.35)}{=} \frac{\widetilde{\Delta t} L_\mathrm{scale} f_0}{2 k_\mathrm{B}} \tilde{T} \overset{(3.32)}{=} \frac{\epsilon_0 s \widetilde{\Delta t}}{k_\mathrm{B}} \tilde{T}. \tag{3.20}$$

3.3.6 Pinning forces

The values of the pinning potential are stored on a fine two-dimensional grid, and we interpolate to obtain potential values between the grid-points. In this section we describe technical details of this interpolation, and have chosen a point like pin on a very coarse grid for demonstration purposes. The physical pinning potential we employ in the simulations is described in section 5.3 on page 70.

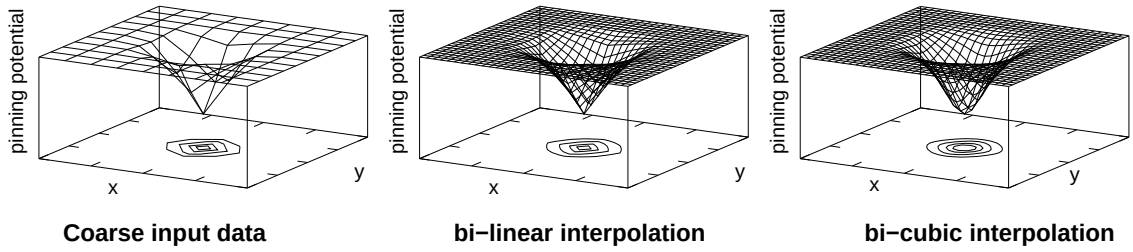

Figure 3.2: Demonstration of pinning potential interpolation. *Left:* Original pinning data as stored in file, showing $-\exp(-r^2)$. For demonstration purposes we have chosen the mesh to be very coarse in order to better visualise the interpolation process. For intermediate positions we interpolate the pinning data. *Middle:* Bi-linear interpolation. *Right:* Bi-cubic interpolation.

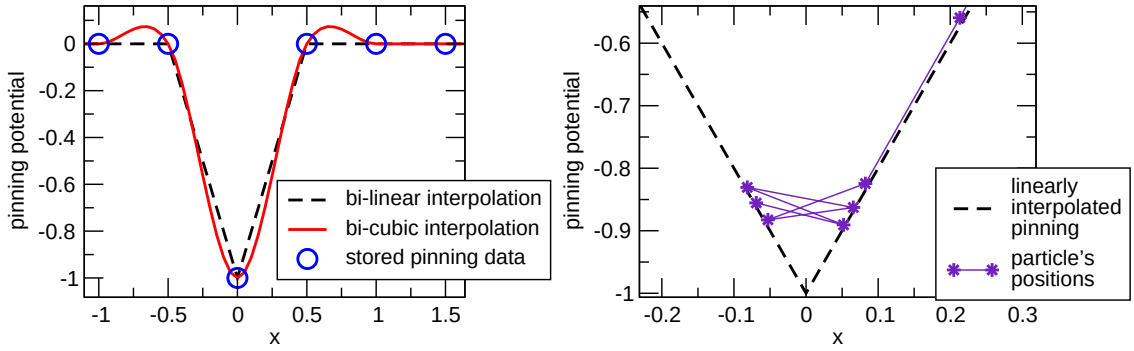

Figure 3.3: *Left:* Comparison of linear interpolation (dashed line) and cubic interpolation (solid line) between the defined potential values (circles). The cubic interpolation results in a smooth minimum at $x = 0$, but overshoots, for example, at $0.5 < x < 1$ thus creating an artifical barrier. *Right:* Bi-linear interpolation of the pinning potential. Artificial behaviour can occur on a small scale: Suppose a particle drops into a pinning well, which is as crudely approximated as shown here. In the absence of other forces it will oscillate around the minimum in the pinning potential.

To compute potential values between the grid-points, we use either a bi-linear or a bi-cubic interpolation method. The bi-cubic method results in a smoother potential. We demonstrate this in figure 3.2.

In figure 3.3 we show a one-dimensional cut through a pinning potential. On the left plot, we demonstrate the difference between the two interpolation techniques for an even coarser pinning potential. It can be seen that the cubic method results in a smooth line, but overshoots. The right plot shows a problem that can occur from using linear interpolation: a trapped particle may oscillate artificially around its equilibrium position.

The overshooting of the cubic interpolation is due to the discontinuity of the first derivative at $x = \pm 0.5$, and this problem is unlikely to happen for realistic pinning

potentials: the vortex core smears pinning over a length scale ξ and the pinning potential should reflect this and therefore vary smoothly. Therefore, the cubic interpolation is the safe method to describe a smoothly varying pinning potential, but for sufficiently fine pinning meshes, the linear interpolation produces the same results.

To obtain the force $\mathbf{F}^{\text{pinning}}(\mathbf{r}_i(t))$ for vortex i at position $\mathbf{r}_i(t)$ one needs the negative gradient of the pinning potential which we compute numerically. We measure the strength of a pinning potential by the root-mean-square value of its force

$$F_{\text{rms}}^{\text{vp}} = \left(\int \mathrm{d}^2 r \quad |\mathbf{F}^{\text{vp}}(\mathbf{r})|^2 \right)^{\frac{1}{2}}. \tag{3.21}$$

3.3.7 The complete equation of motion

Having considered all the forces contributing to the equation of motion, one obtains the following system of N two-dimensional first order ordinary differential equations which describes the motion of vortex pancakes with time in one layer:

$$\begin{aligned} \eta \dot{\mathbf{r}}_i(t) &= \mathbf{F}_i^{\text{vv-interaction}}(\mathbf{r}_1(t), \ldots, \mathbf{r}_N(t)) + \mathbf{F}^{\text{drive}}(t) + \mathbf{F}_i^{\text{thermal}}(t) + \mathbf{F}^{\text{pinning}}(\mathbf{r}_i(t)) \\ &= 2\epsilon_0 s \sum_{\substack{j=1 \\ j\neq i}}^{N} \frac{\mathbf{r}_i(t) - \mathbf{r}_j(t)}{|\mathbf{r}_i(t) - \mathbf{r}_j(t)|^2} + s \cdot \mathbf{j}(t) \times \mathbf{\Phi_0} + \mathbf{F}_i^{\text{thermal}}(t) + \mathbf{F}^{\text{pinning}}(\mathbf{r}_i(t)) \\ & \quad i = 1, \ldots, N \qquad \text{and} \qquad (\mathbf{r}_1(t_0), \mathbf{r}_2(t_0), \ldots, \mathbf{r}_N(t_0)) = (\mathbf{r}_1^0, \mathbf{r}_2^0, \ldots, \mathbf{r}_N^0) \end{aligned} \tag{3.22}$$

The constants η and ϵ_0 are defined in equations (3.7) and (2.4), respectively, s is the length of a vortex, $\mathbf{j}$ is the current density of the transport current, $\mathbf{\Phi}_0$ is the flux quantum directed along the magnetic field perpendicular to the layer, and the $\mathbf{r}_i^0$ are the initial positions of the pancakes at time $t = t_0$.

3.4 Solving the equation of motion

The problem to be solved as given in equation (3.22) is an initial value problem for a coupled set of $2N$ ordinary first order differential equations. Each equation can be written as

$$\frac{\mathrm{d}x}{\mathrm{d}t}(t) = f(t, x) \qquad \text{with} \qquad x(t_0) = x_0. \tag{3.23}$$

Integrating equation (3.23) from time t_n to time t_{n+1} yields

$$x(t_{n+1}) = x(t_n) + \int_{t_n}^{t_{n+1}} f(t, x(t))\, \mathrm{d}t. \tag{3.24}$$

This converts the problem into solving an integral. Integration methods with varying step size $\Delta t = t_{n+1} - t_n$ cannot be used, because a changing step size would change the effective temperature, as visible in equation (3.19).

In principle, there are a variety of methods available to integrate equation (3.24). Most of them can quickly be dismissed for the reason that the most expensive part of the computation is the evaluation of the right-hand side of equation (3.24). Therefore, any method requiring more than one such calculation per time step is wasteful, unless it can deliver a proportionate increase in the step size Δt. However, due to the strongly repulsive force for vortices approaching each other closely, there is an effective upper bound for Δt (*Rapaport*, 1995, p.57).

For this reason, in molecular dynamics simulations only "predictor-corrector" methods or low order "leap-frog" methods play important roles (*Haile*, 1997, p.158). Predictor-corrector methods use information from several previous time steps to approximate the function to integrate by a polynomial, but cannot be used in Langevin simulations as the noise term, $\mathbf{F}^{\mathrm{thermal}}$, in (3.22) introduces discontinuities in the right-hand side of (3.24) and the predictor-corrector method relies on $f(t, x(t))$ being a smooth and continuous function. The typical leap-frog integration employs a simple Euler-integration step for both the velocity and the positions, but computes velocities and positions on a staggered grid in time. The leap-frog method is very stable.

We use a leap-frog type integration scheme which is equivalent to Euler's method since we have no second order derivative in (3.22). For zero-temperature runs, predictor-corrector methods can be employed, but one has to reduce the time step size in comparison to the leap-frog method to make them stable, and the gain in accuracy is not worth the effort: *Rapaport* (1995, p.57) states that a high degree of accuracy in the trajectories is neither a realistic nor a practical goal, and this is particularly true for differential equations with a stochastic term. It is more important that time- and space-dependent correlations can be reproduced. For finite temperatures in our simulations, predictor-corrector methods are intrinsically unstable as they are based on the assumption that the right-hand-side of the differential equation (3.22) can be described by a polynomial. In particular, this requires

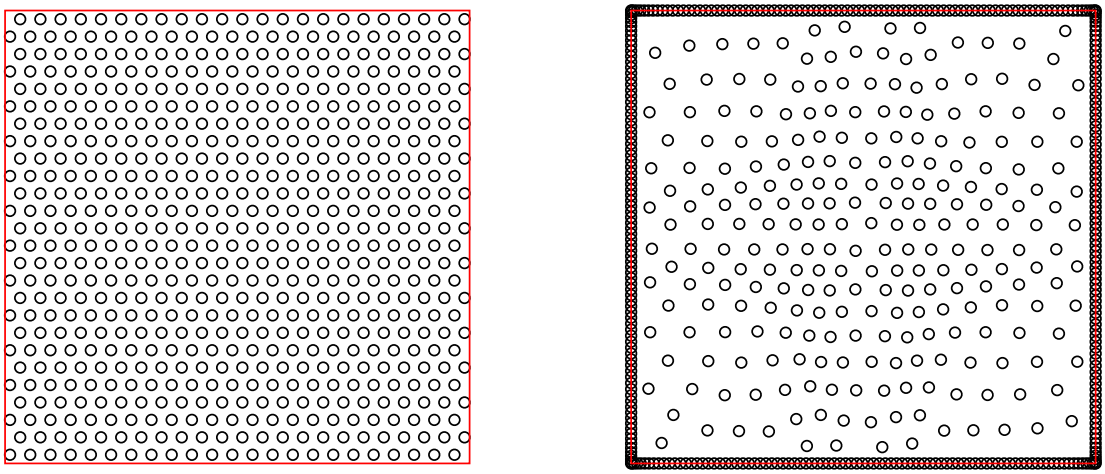

Figure 3.4: *Left:* Initial hexagonal vortex configuration. *Right:* Final configuration after relaxation from configuration shown on the left, using hard boundaries. Due to the strong repulsion, vortices gather at the boundary and the vortex distribution is spatially inhomogeneous. Note, that the apparent thick line around the simulation cell is in fact composed of overlapping circles which represent the vortices at the system's boundary.

continuity which is not given with the randomly varying Langevin noise term.

3.5 Boundary conditions

One simple form of boundary conditions are "hard" boundary conditions: we confine the vortices inside the simulation cell and do not to allow them to cross the boundary. Results of such a run starting from a hexagonal vortex distribution are shown in figure 3.4. The hexagonal configuration is unstable, and the majority of vortices moves to the borders because there is no repulsion from outside the simulation cell.

We are generally interested in the case where the vortex density stays approximately constant. In particular, we would like the hexagonal configuration to be the ground state and therefore stable. This is easily achieved by the conventional approach of using periodic boundary conditions, (next section 3.5.1). In section 3.5.2, we present a second method that allows us to use hard boundary conditions and to achieve a spatially homogenous vortex density. We extend this, and show how any desired vortex density can be achieved.

3.5.1 Periodic boundary conditions

The standard approach in particle simulations in order to avoid the influence of surfaces on the system is to use periodic boundary conditions (for example *Rapaport*,

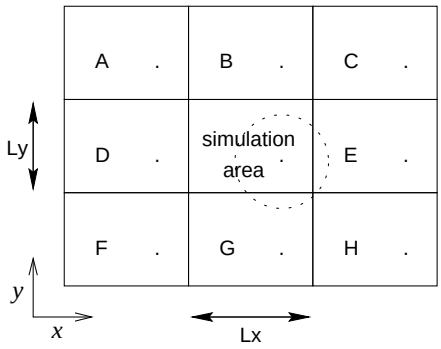

Figure 3.5: Periodic boundary conditions within the planes. The primary cell is surrounded by eight image cells (A to H) of itself. One vortex and all its mirror images are drawn in the lower right corner of the simulation area. Also, the cut-off range for the computation of the interaction force of this vortex with all other vortices is indicated by the dotted circle.

1995, p.16). A system of infinite size is simulated by tiling space with an infinite array of identical copies of the finite simulation region, as indicated in figure 3.5 for only eight copies. There are two different approaches how to deal with particle-particle interactions across the border of the simulation cell:

- The cut-off method cuts off the interaction at some distance shorter than half the length of the simulation cell. This avoids self-interaction of particles. For long-range forces this approach can give misleading results (see chapter 4).
- The infinite lattice summation takes into account the interaction of the particles with all particles in all infinite repeats of the simulation cell in order to evaluate forces and energies. Every particle interacts with all its mirror images which is only feasible if the infinite double sum can be simplified. This method can impose an artificial periodicity onto the system, and is usually computationally more complex than the cut-off approach.

Both methods will be discussed in detail in chapter 4, where we demonstrate that long-range potentials have to be cut-off smoothly, and where we derive a fast method to compute an infinite lattice summation for particles interaction with the Bessel function potential $K_0(\mathbf{r})$. In addition, we have implemented the infinite lattice summation for logarithmic interaction which was developed by *Grønbech-Jensen* in 1996.

In principle, any space-filling convex region can be used as the shape of the primary cell. We have chosen a rectangular simulation cell with lengths L_x and L_y being commensurate with a hexagonal lattice to avoid frustration of the system. Other shapes can be used, but provide no advantage (section 4.3).

3.5.2 Hard boundary conditions

For some applications it is desirable not to use periodic boundary conditions. For example, vortex positions can be used as nodes for a finite-element mesh where

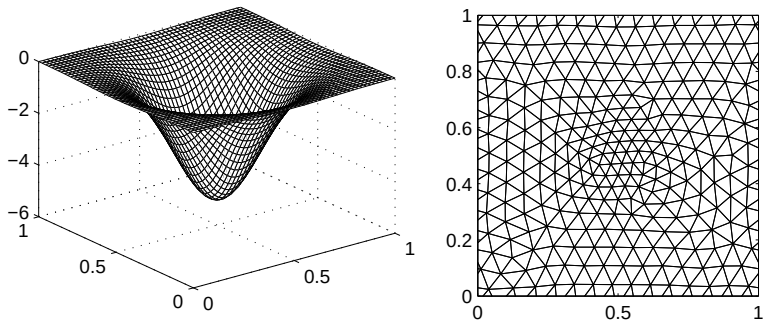

Figure 3.6: Using vortex dynamics to create finite-element meshes. The potential on the left has been used as a "pinning" potential to generate the vortex distribution shown on the right. The vortex density varies spatially, while the mesh maintains a high regularity. We annealed from a liquid system to zero temperature and have used periodic boundary conditions.

the edges are constructed using a Delaunay triangulation of the nodes. The finite-element community requires meshes with a high degree of regularity in order to minimise the numerical error when solving differential equations on the mesh. Regularity usually means that (for unstructured meshes in 2 dimensions) the angles of the triangles should be as close as possible to 60 degrees. This is not trivial as the node-density is required to vary spatially, and the varying node density leads to dislocations. We have shown that such meshes can be created by vortex-dynamics simulations and that they exceed the quality of meshes generated with other available techniques (*Molinari, Fangohr, Generowicz and Cox*, 2001). An example of a finite-element mesh generated using vortex dynamics is shown in figure 3.6.

In this case one would like not to depend on periodic boundary conditions, and to be able to vary the density of the vortices as a function of their position. We have developed a way to achieve both targets: hard boundaries and a varying node density.

3.5.2.1 Spatially constant average vortex density

We start by showing how a constant (spatial) average vortex density can be achieved without using periodic boundary conditions. The underlying problem is that vortices repel each other strongly, and will therefore push each other towards the boundaries of the simulation cell (figure 3.4). We compensate for this by assuming a homogenous anti-vortex distribution within the cell. This is equivalent to having a homogenous vortex distribution outside the simulation cell, which keeps the vortices homogeneously spread within the cell. The effect of these virtual vortices is represented by an extra "pinning" potential which will be added to the Hamiltonian like the pinning potential. In the framework of force computations, the forces from the extra potential have to be added to the equation of motion (3.22).

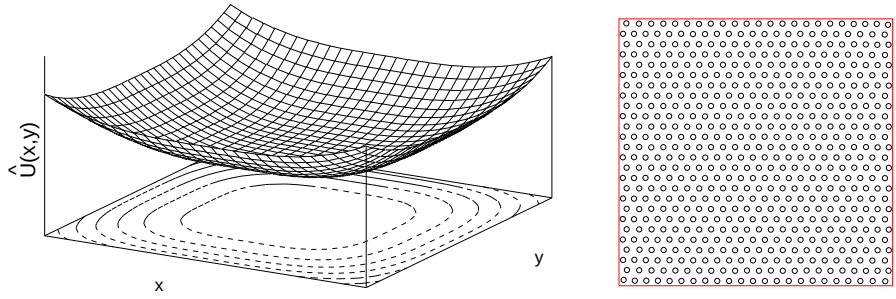

Figure 3.7: *Left:* Potential $\hat{U}(r)$ required for hard boundaries. *Right:* Final vortex distribution after relaxation from hexagonal lattice (as shown in figure 3.4) using hard boundary conditions in the presence of $\hat{U}(\mathbf{r})$. The hexagonal lattice is mainly undistorted, only close to the left and right boundaries some deformation took place.

Suppose vortices interact with an interaction potential $f(\mathbf{r})$ in a rectangular simulation cell of size $L_x L_y$. We compute the potential $\hat{U}(\mathbf{r})$ experienced at position $\mathbf{r}$ when interacting with a (hexagonally distributed) set of anti-vortices j at positions $\mathbf{r}_j$:

$$\hat{U}(\mathbf{r}) \quad = \quad -\sum_j f(\mathbf{r}-\mathbf{r}_j)$$

This will favour vortices at positions r_j (we assume the same number of vortices and anti-vortices). We rewrite

$$\hat{U}(\mathbf{r}) \quad = \quad -\int \mathrm{d}^2 r' \;\; \rho(\mathbf{r}') f(\mathbf{r}-\mathbf{r}') \qquad \text{with} \quad \rho(\mathbf{r}') \equiv \sum_j \delta(\mathbf{r}'-\mathbf{r}_j) \tag{3.25}$$

and smear each anti-vortex over the area it occupies

$$\hat{U}(\mathbf{r}) \quad \approx \quad -\int \mathrm{d}^2 r' \;\; \bar{\rho}\, f(\mathbf{r}-\mathbf{r}') \qquad \text{with} \quad \bar{\rho} \equiv \frac{1}{L_x L_y} \int \mathrm{d}^2 r' \sum_j \delta(\mathbf{r}'-\mathbf{r}_j) \tag{3.26}$$

i.e. $\bar{\rho}$ is just the average (anti) vortex density. Using (3.26) we numerically compute the potential $\hat{U}(\mathbf{r})$ which will (in the absence of any other pinning) result in vortices being distributed homogeneously in the simulation cell without the need to use periodic boundary conditions. We demonstrate this in figure 3.7.

3.5.2.2 Spatially varying average vortex density

Equation (3.26) can be read as a convolution of the interaction $f(\mathbf{r})$ with the required vortex density $\rho(\mathbf{r})$ in the special case of $\rho(\mathbf{r}) = \text{const}$. However, we can

simply write

$$\hat{U}(\mathbf{r}) = -\int \mathrm{d}^2\mathbf{r}'\rho(\mathbf{r})f(\mathbf{r}-\mathbf{r}') \tag{3.27}$$

which provides a pseudo pinning potential $\hat{U}(\mathbf{r})$ which result in a vortex density distribution following $\rho(\mathbf{r})$.

The hard-boundary techniques described here have been used by us (*Molinari et al.*, 2001, *Grigorenko et al.*, 2002) and independently discovered and used by Daniel Shantsev (*Johansen et al.*, 2002).

3.6 Simulation units

It is advisable to scale variables in the simulation such that resulting numbers are of the order of unity: firstly, numerical overflow and underflow have to be avoided. Secondly, scaling can simplify tracking down errors because humans are better in working with number of the order of unity rather than big or small numbers that have to be expressed with exponents. Finally, universal parameters can be identified: it may turn out (by investigating the equations) that some parameters of the problem are irrelevant for the computation, and that numerical results can be scaled afterwards with these parameters.

We label quantities expressed in dimensionless simulation units with a tilde, and introduce scaling factors L_{scale} for length and t_{scale} for time such that

$$\mathbf{r} = L_{\mathrm{scale}}\tilde{\mathbf{r}} \qquad \text{and} \qquad t = t_{\mathrm{scale}}\tilde{t}. \tag{3.28}$$

We express equation (3.22) schematically as

$$\frac{\mathrm{d}\mathbf{r}_i}{\mathrm{d}t} = \mathbf{v}_i = \frac{1}{\eta}(\mathbf{F}_i^{\mathrm{vv-interaction}} + \mathbf{F}_i^{\mathrm{pinning}} + \mathbf{F}_i^{\mathrm{thermal}} + \mathbf{F}^{\mathrm{drive}}) \tag{3.29}$$

with ($\mathbf{r}_{ij}$ representing the displacement of vortex j from vortex i, and $r_{ij} = |\mathbf{r}_{ij}|$)

$$\mathbf{F}_i^{\mathrm{vv-interaction}} \overset{(3.11)}{=} \sum_{j\neq i} \mathbf{F}_{ij}^{\mathrm{vv}}(\mathbf{r}_{ij}) \overset{(3.10)}{=} \sum_{j\neq i} 2\epsilon_0 s \frac{1}{r_{ij}}\frac{\mathbf{r}_{ij}}{r_{ij}}. \tag{3.30}$$

We introduce the scaling length L_{scale} into $\mathbf{F}_{ij}^{\mathrm{vv}}$ given in (3.10)

$$\mathbf{F}_{ij}^{\mathrm{vv}}(\mathbf{r}_{ij}) = 2\epsilon_0 s \frac{1}{r_{ij}}\frac{\mathbf{r}_{ij}}{r_{ij}} = \frac{2\epsilon_0 s}{L_{\mathrm{scale}}}\frac{1}{\tilde{r}_{ij}}\frac{\tilde{\mathbf{r}}_{ij}}{\tilde{r}_{ij}} \equiv f_0\tilde{r}_{ij}\frac{\tilde{\mathbf{r}}_{ij}}{\tilde{r}_{ij}} = f_0\tilde{\mathbf{F}}_{ij}^{\mathrm{vv}}(\tilde{\mathbf{r}}_{ij}) \tag{3.31}$$

which defines our unit of force, f_0, as the repulsion two vortices experience when they are separated by L_{scale}:

$$f_0 = |\mathbf{F}_{ij}^{\text{vv}}(L_{\text{scale}})| = \frac{2\epsilon_0 s}{L_{\text{scale}}} \overset{(2.4)}{=} \frac{\Phi_0^2 s}{2\pi\mu_0\lambda^2 L_{\text{scale}}}. \tag{3.32}$$

Using

$$\mathbf{v}_i = \frac{\mathrm{d}\mathbf{r}_i}{\mathrm{d}t} = \frac{L_{\text{scale}}}{t_{\text{scale}}}\frac{\mathrm{d}\tilde{\mathbf{r}}_i}{\mathrm{d}\tilde{t}} = \frac{L_{\text{scale}}}{t_{\text{scale}}}\tilde{\mathbf{v}}_i \tag{3.33}$$

we rewrite (3.29) as

$$\frac{\mathrm{d}\tilde{\mathbf{r}}_i}{\mathrm{d}\tilde{t}} = \tilde{\mathbf{v}}_i = \frac{t_{\text{scale}}}{L_{\text{scale}}}\frac{f_0}{\eta}\left(\tilde{\mathbf{F}}_i^{\text{vv-interaction}} + \tilde{\mathbf{F}}_i^{\text{pinning}} + \tilde{\mathbf{F}}_i^{\text{thermal}} + \tilde{\mathbf{F}}^{\text{drive}}\right). \tag{3.34}$$

We fix the time-scale t_{scale} by requiring

$$\frac{t_{\text{scale}}}{L_{\text{scale}}}\frac{f_0}{\eta} = 1 \qquad \Longleftrightarrow \qquad t_{\text{scale}} = \frac{L_{\text{scale}}\eta}{f_0}. \tag{3.35}$$

We choose

$$L_{\text{scale}} = \lambda \tag{3.36}$$

but any length of the order of the vortex-spacing would suffice. We thus get a dimensionless equation of motion in which all terms are of the order of unity:

$$\frac{\mathrm{d}\tilde{\mathbf{r}}_i}{\mathrm{d}\tilde{t}} = \tilde{\mathbf{F}}_i^{\text{vv-interaction}} + \tilde{\mathbf{F}}_i^{\text{pinning}} + \tilde{\mathbf{F}}_i^{\text{thermal}} + \tilde{\mathbf{F}}^{\text{drive}}. \tag{3.37}$$

Table 3.1 shows some typical values for $YBa_2Cu_3O_{7-\delta}$ materials, and table 3.2 shows the resulting scaling factors for a simulation using those values. Our choice for the scaling parameters and the resulting natural length, L_{scale}, and time, t_{scale}, are in line with other simulations (*Ryu et al.*, 1996, *van Otterlo et al.*, 1998).

3.6.1 Smallness of time step

The time scale of the simulation is given by t_{scale}. It turns out that for a typical field $B = 1\text{T}$, a time step of $\Delta t \leq 0.005\, t_{\text{scale}}$ has to be used to obtain accurate and stable solutions of the system of differential equations in equation (3.37). This is due to the diverging repulsive vortex-vortex interaction term. If the step size is too large, then vortices come too close to each other and will shoot off in the next time step because they feel a large repulsive force. The smallness of the time step (in real units about 0.5 picoseconds) is, in fact, a common feature of molecular dynamics simulations of microscopic systems (*Allen and Tildesley*, 1989, p.155, and *Haile*,

parameter	symbol	comment	approx. value
YBCO:			
anisotropy	Γ_a		5 - 7
penetration depth (parallel to layers)	λ		1400Å
coherence length	ξ		15Å
layer spacing	s		12Å
upper critical field	B_{c2}	at $T = 90$K	6T
superconductivity transition	T_c	at $B = 0$T	93K
normal state resistivity	ρ_n		$10^{-6}\Omega$m
pancake viscosity (3.7)	η		$1.4 \cdot 10^{-17}$kg/s
BSCCO:			
anisotropy	Γ_a		50-200
penetration depth parallel to layers	λ		$1400 - 2000$Å
coherence length	ξ		$20 - 40$Å
layer spacing	s		15Å
superconductivity transition	T_c	at $B = 0$T	110K
Other entities:			
Planck's constant	h	$2\pi\hbar$	$6.6 \cdot 10^{-34}$Js
electron charge	e		$1.6 \cdot 10^{-19}$C
flux quantum	Φ_0	$\frac{h}{2e}$	$2.1 \cdot 10^{-15}$Tm^2
vacuum permeability	μ_0		$4\pi 10^{-7} \frac{\text{Vs}}{\text{Am}}$
vortex lattice spacing	a_0	$a_0 = \sqrt{\frac{2\Phi_0}{\sqrt{3}B}}$	at $B = 1$T: $a_0 \approx 500$Å

Table 3.1: Typical values for $YBa_2Cu_3O_{7-\delta}$ and $Bi_2Sr_2CaCu_2O_8$ compounds (*Blatter et al.*, 1994, *Tinkham*, 1996, *Gordeev*, 2000) and some physical constants.

name	relation	factor	typical value (YBCO)
Scaling factors			
length (3.36)	$r = L_{\text{scale}}\tilde{r}$	$L_{\text{scale}} = \lambda$	1400Å
time (3.35)	$t = t_{\text{scale}}\tilde{t}$	$t_{\text{scale}} = \frac{L_{\text{scale}}\eta}{f_0}$	$9.1 \cdot 10^{-12}$s
velocity	$v = \frac{L_{\text{scale}}}{t_{\text{scale}}}\tilde{v}$	$\frac{L_{\text{scale}}}{t_{\text{scale}}} = \frac{f_0}{\eta}$	$1.5 \cdot 10^{4}$m/s
force (3.32)	$F = f_0\tilde{F}$	$f_0 = \frac{2\epsilon_0 s}{\lambda}$	$2.2 \cdot 10^{-13}$N
energy	$E = e_0\tilde{E}$	$e_0 = L_{\text{scale}} f_0 = 2\epsilon_o s$	$3 \cdot 10^{-20}$Nm ≈ 0.2eV
temperature (3.20)	$T = T_0\tilde{T}$	$T_0 = \frac{\Delta t f_0^2}{2\eta k_{\text{B}}} = \frac{\epsilon_0 s \widetilde{\Delta t}}{k_{\text{B}}}$	5.6K
Gamma (6.1)	$\Gamma = \frac{\Gamma_0}{\tilde{T}}$	$\Gamma_0 = \frac{2}{\widetilde{\Delta t}}$	400
Other factors			
ϵ_0 (2.4)		$\epsilon_0 = \frac{\Phi_0^2}{4\pi\mu_0\lambda^2}$	$1.3 \cdot 10^{-11}$N
time step $\widetilde{\Delta t}$			0.005

Table 3.2: Typical values for simulation scaling factors using physical parameters given in table 3.1, and some other factors used.

1997, p.163). This limits quantitative simulations to time scales $\approx 0.1\mu$s, since about one million time steps can be computed in reasonable time (for $B = 1$T).

The main problem in quantitative high-temperature superconductor simulations of the vortex state is that the critical Lorentz force, F_c, required to depin the system can be very small, for example in comparison to the force $F_{j_0}^{\text{drive}}$ exerted by the Cooper-pair depairing current $j_0 = \Phi_0/(3\sqrt{3}\pi\lambda_{ab}^2\xi\mu_0) \approx 3 \cdot 10^{12}\text{Am}^{-2}$ (*Brandt*, 1995, Sec 1.1). Whereas at low temperatures for YBCO the ratio $F_c/F_{j_0}^{\text{drive}}$ is of the order of $j_c/j_0 \approx 0.01$ (*Higgins and Bhattacharya*, 1996), it becomes much smaller for larger temperatures. At liquid nitrogen temperature the depinning current density is of the order $j = 10^5\text{Am}^{-2}$ corresponding to $F_c/F_{j_0}^{\text{drive}} \approx 3 \cdot 10^{-8}$. For a driving force $F^{\text{drive}} = 3 \cdot 10^{-8} F_{j_0}^{\text{drive}}$ the resulting free flow velocity is so small that the vortex system travels less than one lattice spacing a_0 within 0.1μs.

In simulation units the de-pairing drive is[2] $\tilde{F}_{j_0}^{\text{drive}} \approx 30$. The smallest (transverse) forces investigated in this work are of the order of $10^{-4} f_0$ and the largest forces are $8 f_0$ corresponding to $3 \cdot 10^{-6}\tilde{F}_{j_0}^{\text{drive}}$ and $\approx 0.25\tilde{F}_{j_0}^{\text{drive}}$, respectively.

In computer simulations of the vortex state, Lorentz forces which are significantly larger than realistic for high temperatures are employed to compensate for the smallness of the time interval (for example *Olson et al.*, 1998a, *van Otterlo et al.*, 1998). Accordingly, there is a tendency to choose the strength of the pinning potential to be too big to allow investigation of the depinning transition.

[2] $\tilde{F}_{j_0}^{\text{drive}} = F_{j_0}^{\text{drive}}/f_0 \overset{(3.12)}{=} |\mathbf{j}_0 \times \mathbf{\Phi_0} s|/f_0 = \ldots = 2L_{\text{scale}}/(3\sqrt{3}\xi)$

In other areas of research using molecular dynamics techniques similar problems exist. Two examples are simulations of protein unfolding, in which unphysically high temperatures are used to trigger the reaction to happen within the simulation time window (*Tirado-Rives and Jorgensen*, 1993), and computations which model the stretching of a dextran molecule due to an atomic force microscope (AFM), in which the simulated pulling force used is nine orders of magnitude larger than in the experiment (*Rademacher*, 1999).

In summary, whereas the low-temperature regime can be simulated with quantitatively reasonable parameters, this is not possible for the dynamics in the high-temperature regime. This is due to the small time window a computer simulation can cover.

3.7 Limits of model applicability

The described simulation is a model of a set of classical repelling massless point-like particles under the influence of thermal fluctuations, a driving force, and an underlying potential in two dimensions. This can be related to the vortex state in high-temperature superconductors in two-dimensional (thin-films, stack of superconducting layers) and quasi-two-dimensional systems (rigid vortices) with and without pinning, and at zero and finite temperatures. Using the substrate model (chapter 6) we can also study a three-dimensional layered system in the high anisotropy limit of zero Josephson coupling with electromagnetic interlayer interactions. Our simulation can also be related to the classical two-dimensional one-component plasma (*de Leeuw and Perram*, 1982, *Caillol et al.*, 1982, *Choquard*, 1983) in which electrons experience the same logarithmic repulsion. In the context of the vortex state we mention two limitations:

- The use of classical particles to represent vortices makes it impossible to include phenomena such as vortex-anti-vortex pair creations. Of course, the breakdown of superconductivity at too high a field or too high a temperature cannot be simulated either. Therefore, the simulation should not be applied to regimes near the upper or lower critical field.
- Quantitative simulations of dynamic systems are restricted by the smallness of the time scale that can be simulated (subsection 3.6.1). However, the number of computer simulations being subjected to the same or similar restrictions and still providing great insight into physical concepts encourages the belief that the results are qualitatively correct, even if driving forces which are artificially large have to be used.

3.8 Observables

3.8.1 Positions and velocities

The governing equation of motion (3.22) automatically provides velocities and positions of all vortices as a function of time, and we can compute the "centre of mass"-position and velocity of the system

$$\mathbf{r}_{\mathrm{cm}}(t) = \frac{1}{N}\sum_{i=1}^{N}\mathbf{r}_i(t) \qquad \text{and} \qquad \dot{\mathbf{r}}_{\mathrm{cm}}(t) = \frac{1}{N}\sum_{i=1}^{N}\dot{\mathbf{r}}_i(t). \tag{3.38}$$

Periodic boundary conditions are considered in the computation of the centre of mass, *i.e.* a vortex leaving the simulation box to the left and re-entering from the right will not result in a discontinuity in $\mathbf{r}_{\mathrm{cm}}(t)$.

3.8.2 Energy

The energy of the system consists of the electromagnetic interaction between vortices (section 2.3.3), and the energy gain from the pinning surface. There is no kinetic energy since the inertial mass is zero.

3.8.3 Mean square displacement

The running mean square displacement

$$\Delta r^2(t) = \frac{1}{N}\sum_{i=1}^{N}[\mathbf{r}_i(t) - \mathbf{r}_i(t_0)]^2 \tag{3.39}$$

can be used to distinguish between a solid and a liquid state of the system. For a solid, $\Delta r^2(t)$ remains nearly constant, whereas for a fluid it increases almost linearly with time (*Haile*, 1997, p.209).

3.8.4 Structure factor

The structure factor as the Fourier transform of the local density $\rho(\mathbf{r}) = \sum_{l=1}^{N}\delta(\mathbf{r}-\mathbf{r}_l)$ for a set of N discrete particles reads

$$S(\mathbf{k}) = \int \mathrm{d}\mathbf{r}\, \sum_{l=1}^{N}\delta(\mathbf{r}-\mathbf{r}_l)\exp(-i\mathbf{k}\cdot\mathbf{r}) = \sum_{k=l}^{N}\exp(-i\mathbf{k}\cdot\mathbf{r}_l). \tag{3.40}$$

This can be evaluated numerically for every required value of $\mathbf{k}$. An alternative approach to compute $S(\mathbf{k})$ for many $\mathbf{k}$, is to define a coarse grained density function $\tilde{\rho}(r)$ based on a two-dimensional grid with suitable spatial resolution and equidistant grid points and then to use a discrete two-dimensional fast Fourier transform (*Frigo*

and Johnson, 1998) to obtain $S(\mathbf{k})$. The latter method is more efficient if we require $S(\mathbf{k})$ for many $\mathbf{k}$.

3.8.5 Delaunay triangulation

The Delaunay triangulation for a set of points in a plane can be defined as in *de Berg et al.* (1997, p.188): "A triangulation of a set of points $\mathcal{P}$ is the Delaunay triangulation if and only if the circumcircle of any triangle (going through the three points of the triangle) in the triangulation does not contain any further points of $\mathcal{P}$ in its interior." The Delaunay triangulation is unique, if points are not co-circular, *i.e.* four particles must not be located on a circle. The Delaunay triangulation allows easy visualisation of the lattice structure of a set of particles and also provides further topological data such as the nearest neighbours.

We have used the "Quickhull"-routine in order to obtain Delaunay triangulations of vortex positions. The source code in C, which has kindly been provided by the Indianapolis Computation Geometry Centre (*Geometry Centre*, 1999), has been integrated in the analysis software. For sets with co-circular points the data is randomly jiggled to resolve this undefined situation. Details of the very efficient algorithm employed, are found in *Barber et al.* (1996).

3.8.6 Number of defects

The Delaunay triangulation provides information about nearest neighbours, and by counting them we find vortices with more or less than six nearest neighbours. These are referred to as topological defects.

3.8.7 Local hexagonal order

From the Delaunay triangulation the bond angles, θ_k, of the vortices can be evaluated. Using these, a parameter Ψ_6 that represents the local hexatic order of the system can be computed:

$$\Psi_6 = \frac{1}{n_{\mathrm{bond}}} \left| \sum_{k=1}^{n_{\mathrm{bond}}} \exp(i6\theta_k) \right| \tag{3.41}$$

Here, n_{bond} gives the number of bonds (or equivalently angles) in the Delaunay triangulation which are considered to be numbered from 1 to n_{bond}. For a perfect hexagonal lattice $\Psi_6 = 1$.

3.8.8 Other observables

A variety of observables can easily be computed in the framework of the substrate model, and equations are given in chapter 6.

3.9 Simulation software

3.9.1 Programming language

We have developed a suite of programs written in platform independent ANSI C++, complemented with a set of Python[3] and Bash[4]-scripts to assist in data analysis and job submission.

3.9.2 A computation cycle

3.9.2.1 Input data

The user specifies their requirements by writing the configuration of a run (run-ID, number of vortices, magnetic induction, vortex-interaction, ...), in a simple text-file, called a *configuration file*. If a pinning potential is required, then the name of a data-file[5] containing the potential is included in the file. Any time-dependent events (such as an increase of the driving force) are including in this configuration file in the form of an event list.

It is advantageous to have configuration files stored in plain text as they can easily be created and modified by scripts, which is useful for parameter space exploration.

3.9.2.2 Pre-processing of input data

The configuration file is processed by the first program of our suite. This checks for correct syntax and plausibility. If required, further parameters — which usually the user does not need to care about — are computed (such as coefficients for the smoothing of the interaction close to the cut-off), and eventually a *parameter file*, based on the user input *configuration* file, is written by the program. This file contains all information that the simulation software needs to perform the simulation.

There are two reasons for this step: firstly, we check for typos and other mistakes so we can be reasonably sure that the computation based on this parameter file will not fail for trivial reasons. Secondly, having all information in a text file means that by simply storing this file (and the corresponding pinning data), a run can be reproduced. Note also, that no re-compilation is required at any stage because no configuration details are hard-coded.

3.9.2.3 The computation

At the beginning of the computation the parameter file is read, the pinning potential is loaded, and tables (for infinite lattice summations, and pinning interpolation) are

[3]Python is on object oriented, interactive, interpreted language. (`http://www.python.org`)

[4]Bash is the "Bourne again shell" and available for Linux/Unix and windows operating systems.

[5]We have a selection of input formats for pinning potentials, for example a two-dimensional table in plain text, or a bitmap such as a jpeg or png-file.

precomputed. Then all requested time-steps are computed, and vortex positions are saved to disk regularly. We have developed a compression algorithm to store the vortex position data as efficiently as possible, and this is detailed in appendix A.

If requested in the parameter file, the driving force, pinning strength or temperature can change at specified time steps. No user intervention is required to perform the complete computation which is important when running jobs on computational (non-interactive) clusters.

3.9.2.4 Data analysis

A third program operates on the saved data files and allows to extract the raw stored data as well as derived observables. We have provided methods to write data to a variety of formats to be able to use different tools for data analysis. We mainly use OpenDX[6] and Xmgrace[7] to visualise static and dynamic data. For high-quality presentations and animations of the pinning surface, we use PovRay.[8]

3.9.3 Computational infrastructure

We have used the Beowulf cluster of the University of Southampton with 324 CPUs running at 1GHz and 1.5GHz. Jobs are submitted via a queuing system.

3.10 Summary

A model of the vortex state in high-temperature superconductors has been proposed and implemented efficiently. The model is based on a Langevin dynamics simulation. Vortices are considered as massless point-like particles that repel each other due to their electromagnetic interactions, and are free to move continuously in a two-dimensional area with (periodic) boundary conditions. Vortices experience an underlying pinning potential representing atomic inhomogeneities of the sample, and a Lorentz force representing a transport current. The model describes the physics of a many-body system with competing interactions, and is a good description of a system of pancake vortices (which are not coupled with the other layers) and vortices in thin film superconductors. Such a system is equivalent to the two-dimensional one-component plasma (apart from scaling factors). Using the substrate model (chapter 6) we can also model a three-dimensional layered pancake vortex system in the high anisotropy limit of zero Josephson coupling.

[6] OpenDX is an open-source project based on IBM's Visualization Data Explorer. (`http://www.opendx.org`)

[7] Xmgrace is a scriptable WYSIWYG 2D plotting tool, and a descendant of ACE/gr, also known as Xmgr. (`http://plasma-gate.weizmann.ac.il/Grace`)

[8] PovRay is a Raytracing software to create photo-realistic images of 3D-scenes. (`http://www.povray.org`)

Chapter 4

Efficient methods for handling long-range forces in particle simulations

Preface

The work described in this chapter started in the final-year project of my undergraduate degree and I have created figures 4.1, 4.2 and 4.4 during that time. In my postgraduate studies I continued and completed the investigation. The central ideas of this chapter have been published (*Fangohr, Price, Cox, de Groot, Daniell and Thomas*, 2000).

4.1 Introduction

Considerable effort has been invested in handling long-range forces for particle-particle simulations. The conventional cut-off approach truncates the potential in a single unit cell for separations greater than half the system dimension. In general, it is better to sum the potential over a number of repeats of the unit cell. Infinite summation methods include the Ewald summation (*Ewald*, 1921, *de Leeuw et al.*, 1980, *Allen and Tildesley*, 1989), multipole methods (*Greengard and Rohklin*, 1987), lattice summation methods (*Berman and Greengard*, 1994), the Lekner summation method (*Lekner*, 1989, 1991) and a novel method for logarithmic interactions (*Grønbech-Jensen*, 1996). In this paper we review some of the problems which can occur when the potential is naïvely truncated, which have not previously been widely reported in the literature. We then derive two methods which overcome these problems. The first is suitable for phenomenological studies of systems and smooths the potential within a single unit cell. The second is a new real-space

summation method appropriate for potentials governed by Bessel functions. This provides a speed-up factor of at least 20,000 compared to the current method of summing in a series of shells of increasing radius (*Ryu et al.*, 1996).

In section 4.2 we introduce our model system, which is a simulation of the vortex state in a superconductor. We discuss the problems which arise with cutting off the interaction potential in a single unit cell in section 4.3, and give a method of smoothing the potential which overcomes these problems in section 4.4. We detail the implementation of this method in section 4.5. In section 4.6 we consider an infinitely tiled periodic system and derive our new summation method. Section 4.7 describes a simulation of shearing a lattice using our new methods and contrast it with the results obtained when the potential is cut off. Two ways to speed up computations using the suggested methods are described in section 4.8, and we draw our conclusions in section 4.9.

4.2 Model system

We will consider the long-range forces which arise in the simulation of vortices in high-temperature superconductors (*Clem*, 1998). The interaction potential for vortex lines is (*Tinkham*, 1996):

$$\frac{U(r)}{c} = K_0\left(\frac{r}{\lambda}\right) \tag{4.1}$$

where λ is the penetration depth of the magnetic field, r is the distance between the particles and c is a constant. This may be approximated as

$$\frac{U(r)}{c} = \begin{cases} \sqrt{\frac{\pi\lambda}{2r}}\exp\left(-\frac{r}{\lambda}\right) & : \quad r \to \infty \\ \ln\left(\frac{\lambda}{r}\right) + 0.12 & : \quad r \ll \lambda. \end{cases} \tag{4.2}$$

Since λ in thin films can be several orders of magnitude larger than r (*Ryu et al.*, 1996), the K_0 potential has a very long range (logarithmic) character. It is therefore necessary to either (i) only consider the interaction inside a single unit cell which contains a large number of particles, or (ii) sum the interaction over periodic repeats of the unit cell. Our findings are also of relevance to the simulation of other systems governed by long-range forces such as logarithmically interacting pancake vortices and the two-dimensional one-component electron plasma (*Caillol et al.*, 1982, *de Leeuw and Perram*, 1982) as well as the interaction of electrically charged rods (*Grønbech-Jensen*, 1996). We will show results for Monte Carlo simulations, and for molecular dynamics simulations with a friction term and a random noise term

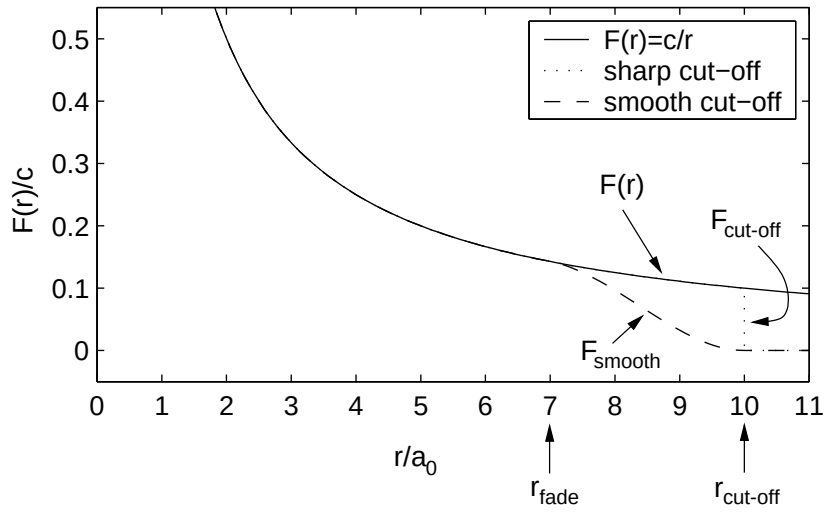

Figure 4.1: A long-range force (solid line), force cut-off at a distance $r_{\mathrm{cut-off}}$ (dotted line), and smoothed force (dashed line). Distances are measured in multiples of the ground-state lattice spacing, a_0.

(known as Langevin dynamics, section 3.1). The two-dimensional unit cell geometry can be chosen to be a rectangle, a parallelogram or a hexagon. In all cases periodic boundary conditions are employed.

4.3 Cut-off potential

The standard approach is to cut off the potential to be constant outside a circle of radius smaller or equal to $\min(L_x/2, L_y/2)$, where L_x and L_y are the lengths of the sides of the unit cell. Since the force is the gradient of the potential, it is zero outside the cut-off radius. Considering periodic boundary conditions, we then define the distance between particles, r, to be the minimum image distance (*Allen and Tildesley*, 1989).

In figure 4.1 the real force dependence $F(r)$ (solid line) is compared to that for a simulation system with a simple geometrical cut-off (dotted line). For vortices in superconductors, *Abrikosov* (1957) demonstrated theoretically that the lowest energy configuration for an infinite lattice is the hexagonal lattice, or so-called Abrikosov lattice, with an associated Abrikosov lattice energy. However, when using a sharp cut-off in our simulations we find many configurations with energies lower than the Abrikosov lattice energy.

Figure 4.2 on the following page shows the results from a Langevin dynamics simulation of a small number of particles in which the temperature in the system is cycled from 0K to half the melting temperature of the vortex solid and is then returned to 0K. The temperature is introduced via a stochastic noise term (3.4). The Delaunay triangulation of the vortex configuration at the end of the simulation is elastically deformed and shown on the right in figure 4.2. Detailed examination of the triangulation shows that the elastic deformations arise due to particles

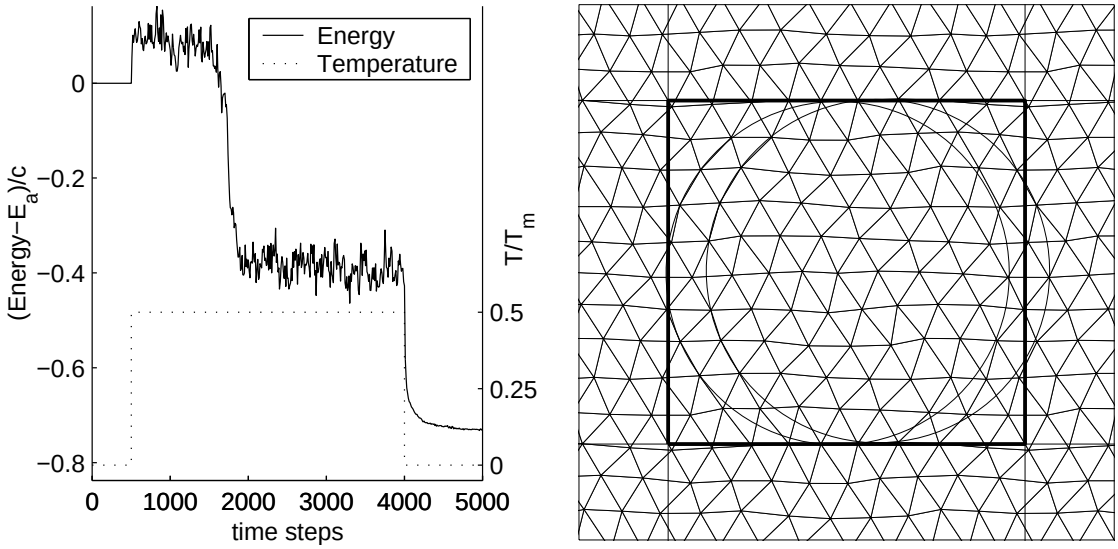

Figure 4.2: Left: Langevin dynamics simulation of 90 particles using a cut-off potential, which start in a hexagonal configuration at 0K (with Abrikosov lattice energy, E_a), are heated to half their melting temperature (T_m) and then returned to 0K. Temperature is introduced via a stochastic noise term (3.4). The system finds a new configuration with energy lower than the energy of the regular lattice. Right: Delaunay triangulation of the final configuration of the particles at time step 5000. Two cut-off circles are shown to demonstrate that particles align along these circles.

gathering on the boundaries of the cut-off circles. In this position they minimise their contribution to the energy in the system. This gives rise to the "wavy lines" visible in figure 4.2, with a curvature characterised by the cut-off radius. To demonstrate this, we have shown the cut-off circles corresponding to two of the particles. The wavy lines are less evident in larger systems, since their curvature is inversely proportional to the cut-off radius.

If the system is heated above its melting temperature and then annealed slowly, the final equilibrium state (i) has an energy lower than the Abrikosov energy, and (ii) contains topological defects. A topological defect is a particle which does not have six nearest neighbours in the Delaunay triangulation. We have repeated these results for molecular dynamics and Monte Carlo simulations with up to 2000 particles. The result in figure 4.3 for a Monte Carlo simulation of a system annealed from a liquid state exhibits low energy and contains defects. We have verified that our results are independent of the geometry of the unit cell (rectangular, parallelogram, or hexagonal).

These problems are clearly artificial, and are caused by imposing a sharp cut-off on the very long range nature of the interaction. It is possible that these finite size effects disappear for much larger systems, which — depending on the penetration

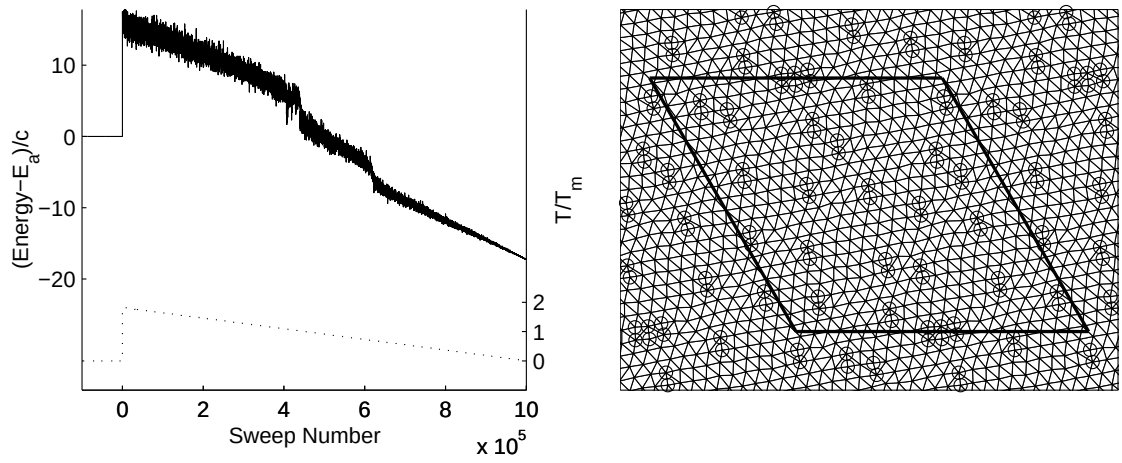

Figure 4.3: Monte Carlo simulation of 432 particles using a conventional cut-off potential. The system starts in a regular hexagonal Abrikosov lattice and is heated above its melting point to approximately $2T_m$ then annealed slowly to zero temperature in steps of $0.01T_m$ each step consisting of 5000 Monte Carlo-sweeps. Left: The energy of the system drops below the Abrikosov lattice energy, E_a. Right: Delaunay triangulation of the final disordered configuration. The topological defects are circled.

depth, λ — would require systems with several hundred thousand particles before the effects of this problem began to become less significant. Methods to deal with such large systems with the Bessel function interaction potential are currently being developed (*Cox et al.*, 2001), but here we focus on system sizes ≤ 3000 particles which is feasible with today's technologies.

In studies of high temperature superconductors, interest has recently developed in the formation of topologically ordered states which exhibit quasi-long range translational order: the so-called Bragg glass. These states occur when the vortices are weakly pinned and have been investigated both theoretically and experimentally (for example *Giamarchi and Le Doussal*, 1995, *Kokkaliaris et al.*, 1999). Other studies have focused on the structural properties of the dynamics of vortex systems (for example *Higgins and Bhattacharya*, 1996, *Spencer and Jensen*, 1997). In both cases it is important that the ground state for an unpinned system should be a hexagonal lattice without topological defects. Furthermore, for the calculation of numerical phase diagrams as a function of disordering pinning, it is vital that the disorder is not introduced by the model itself.

We therefore propose two methods which avoid the problems described above. The first involves modifying the potential near to the cut-off, and allows qualitative simulation of small systems using only a single unit cell. The second is a fast summation method which allows the infinitely tiled periodic system to be considered and enables quantitative simulations to be performed.

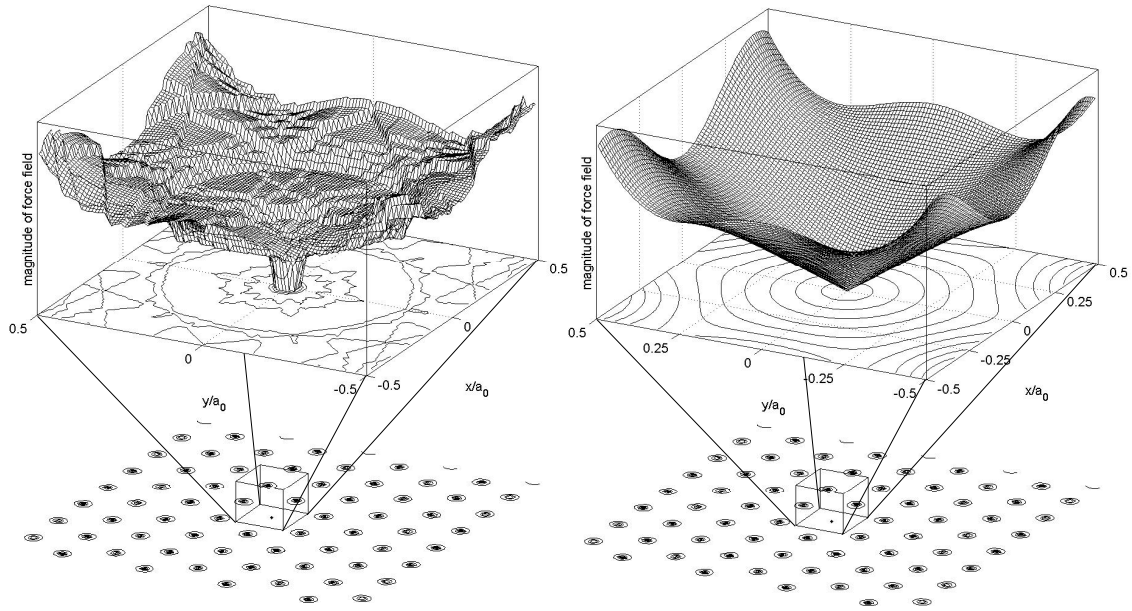

Figure 4.4: The magnitude of the force field that a particle at position (0,0) experiences from a system of 418 particles using (left) the sharp cut-off and (right) the smooth cut-off. Smoothing the potential removes the discontinuities in the force field.

4.4 Smoothed potential

In figure 4.4 (left) we show the force field experienced by a vortex due to its surrounding particles in a hexagonal configuration. The discontinuities are caused by the artificial step in the force function shown in figure 4.1 on page 51. It is natural to introduce a smoothed potential, which reduces the force smoothly to zero over a region from r_{fade} to $r_{\text{cut-off}}$. We impose $\mathcal{C}^1$ continuity of the force at $r = r_{\text{fade}}$ and $r = r_{\text{cut-off}}$, *i.e.* we require the derivative of the force to be continuous at at $r = r_{\text{fade}}$ and $r = r_{\text{cut-off}}$. The smoothed potential is shown in figure 4.1 (dashed line), with the resulting smooth force field in figure 4.4 (right). The smoothing distance $r_{\text{cut-off}} - r_{\text{fade}}$ is a free parameter which should be kept as small as possible to maintain the original force over the largest possible range. Numerical experiments show that three lattices spacings is sufficient. Figure 4.5 shows the results of a Monte Carlo simulation using a similarly smoothed energy. Simulations using this modified potential do not find configurations below the Abrikosov energy and topological defects only occur when the system is annealed very rapidly.

The interpretation is that due to the slow force change at the cut-off (enforced by the derivative being zero) a particle pair separated by a distance of $\approx r_{\text{cut-off}}$ experiences continuous and small changes in force if the relative displacement of the particles is perturbed. This is in contrast to the large discontinuous fluctuations that occur when the sharp cut-off is being used, which can enable the system to

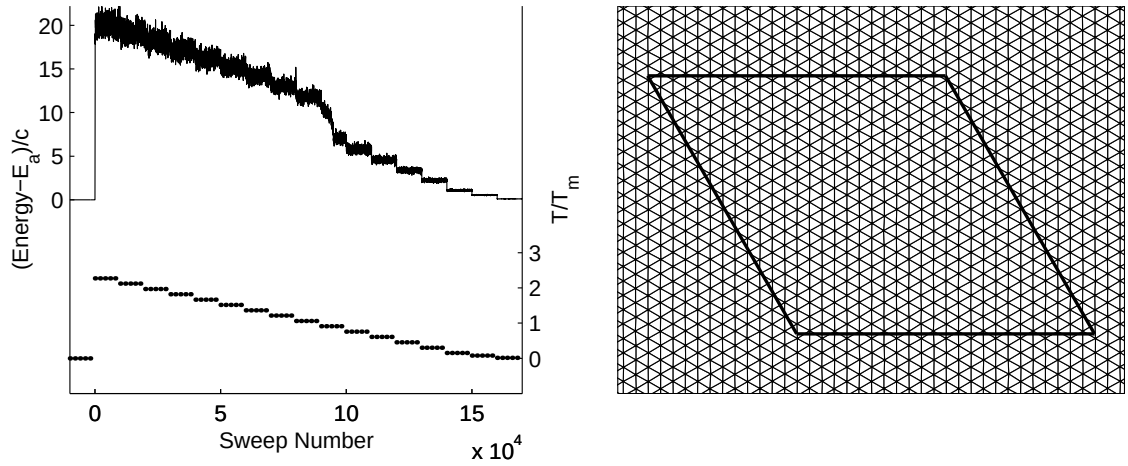

Figure 4.5: Monte Carlo simulation of 432 particles using a potential smoothed over three lattice spacings. Left: The energy of the system never drops below the Abrikosov lattice energy, E_a. Right: Delaunay triangulation of the final configuration shows the system has a hexagonal ground state.

discover configurations with energies less than the Abrikosov energy. We have also used interpolating polynomials of higher order and an exponential function in the smoothing region: in all cases the system does not discover energy states below the Abrikosov energy.

It is important to consider whether the modification of the original force with the smooth cut-off affects the system's behaviour. Applying a cut-off to the long-range interaction is a major change of the long-range interaction. However, introducing the smoothing distance and altering the force in the region between $r_{\rm fade}$ and $r_{\rm cut-off}$ cannot be worse than using a slightly smaller system with $r'_{\rm cut-off} = r_{\rm fade}$. The enormous advantage of using a smooth cut-off is that the structural properties of the system can be simulated correctly and that the lowest energy configuration is identical to the known ground state. For studies of the dynamics of vortices, recent results show that the precise details of the long-range particle interaction are not crucial (*Zhu et al.*, 1999), and this is in agreement with our results (for example figure 6.11) which show no differences between using an infinite lattice summation and using a smooth cut-off. We therefore recommend using the smoothed potential instead of the sharp cut-off.

4.5 Implementation of smooth cut-off

We now describe how to implement a smooth cut-off using a third order polynomial for the force $F(r)\frac{\mathbf{r}}{|\mathbf{r}|} = -\nabla U(r)$, and a fourth order polynomial for the energy $U(r)$.

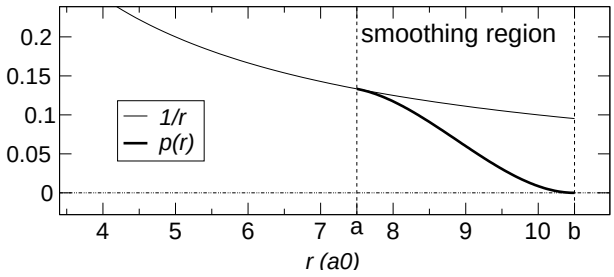

Figure 4.6: Demonstrating the shape of the interpolating polynomial $p(r)$ (thick line) which smoothly reduces the vortex-vortex interaction force $F(r)$ to zero. For clarity we have chosen $F(r) = 1/r$. The interpolation starts at the fading distance $a = 7.5a_0$ and reduces the interaction force to zero at the cut-off distance $b = 10.5a_0$, where a_0 is the average vortex lattice spacing.

For short-ranged interactions it is sufficient to use an interaction $\hat{F}(r)$ which is equal to $F(r)$ for $r \leq b$ and zero otherwise:

$$\hat{F}(r) = \begin{cases} F(r) & : \quad r \leq b \\ 0 & : \quad r > b. \end{cases} \tag{4.3}$$

However, to avoid the artificial configurations described above we reduce the long-range force $F(r)$ smoothly to zero near the cut-off distance b as shown in figure 4.6. One needs to introduce another distance, a, and a polynomial $p(r)$, such that $a < b$ and that $p(r)$ interpolates between $F(a)$ at a and and zero at b:

$$\hat{F}(r) = \begin{cases} F(r) & : \quad r \leq a \\ p(r) & : \quad a < r \leq b \\ 0 & : \quad r > b. \end{cases} \tag{4.4}$$

It is required that $\hat{F}(r)$ has $\mathcal{C}^1$ continuity at a and b, and its gradient at b is zero:

$$F(a) = p(a), \tag{4.5}$$

$$p(b) = 0, \tag{4.6}$$

$$\left.\frac{\mathrm{d}F}{\mathrm{d}r}\right|_{r=a} = \left.\frac{\mathrm{d}p}{\mathrm{d}r}\right|_{r=a}, \tag{4.7}$$

$$\left.\frac{\mathrm{d}p}{\mathrm{d}r}\right|_{r=b} = 0. \tag{4.8}$$

We have used a third order polynomial

$$p(r) = \sum_{i=0}^{3} c_i r^i = c_3 r^3 + c_2 r^2 + c_1 r + c_0 \tag{4.9}$$

and the coefficients c_i are completely determined by equations (4.5) to (4.8). Writing $F'(r)$ for $\frac{\mathrm{d}F}{\mathrm{d}r}(r)$ one finds

$$\begin{pmatrix} c_3 \\ c_2 \\ c_1 \\ c_0 \end{pmatrix} = \frac{1}{(a-b)^3} \begin{pmatrix} F'(a)a - F'(a)b - 2\,F(a) \\ -F'(a)a^2 + 3\,F(a)(a+b) - aF'(a)b + 2\,F'(a)b^2 \\ (2\,F'(a)a^2 - aF'(a)b - 6\,F(a)a - F'(a)b^2)\,b \\ -F'(a)b^2a^2 + 3\,F(a)ab^2 + F'(a)ab^3 - b^3F(a) \end{pmatrix}. \quad (4.10)$$

The cut-off distance, b, is determined by geometrical constraints, *i.e.* half the system size, or by the computational resources available. We choose the distance $b - a$ over which the interaction is reduced to zero to be three lattice spacings, so that $a = b - 3a_0$. Figure 4.6 shows a schematic plot of the smooth cut-off and the interpolating polynomial.

To compute the similarly smoothed potential energy of the system, it is required to integrate $-p(x)$ to represent the smoothed interaction potential for $a < r < b$. The integration constant is determined by requiring continuity of the interaction potential at $r = a$.

4.6 Fast infinite summation

An alternative approach to modifying the potential is to sum the potential function over periodic repeats of the unit cell, which provides the best representation of the system given only a finite number of particles. We write the potential (4.1) in the form (*Ryu et al.*, 1996):

$$\frac{U(|\mathbf{r}|)}{c} = K_0^*\left(\frac{|\mathbf{r}|}{\lambda}\right) = \sum_{m_x,m_y} K_0\left(\frac{|\mathbf{r}| + L_x m_x \hat{\mathbf{x}} + L_y m_y \hat{\mathbf{y}}}{\lambda}\right), \quad (4.11)$$

where m_x and m_y are integers and L_x and L_y are the lengths of the edges of the simulation cell. This is truncated such that $m_x^2 + m_y^2 \leq N_m^2$; we sum the potential in shells of increasing radius, N_m, until it has converged.

In order to be able to compare our findings with the results of *Ryu et al.* (1996), we follow their choice of parameter values. We use a value for the penetration depth, λ, at 0K of 7700Å for $Mo_{77}Ge_{23}$. We will return to the temperature dependence of λ later. In figure 4.7, we show the exponentially fast convergence of the energy between two particles in a simulation of 300 vortices in the Abrikosov lattice state, as more image cells are included. We also show the time taken to perform this calculation on a 450 MHz Pentium II using Compaq (Digital) Visual Fortran under

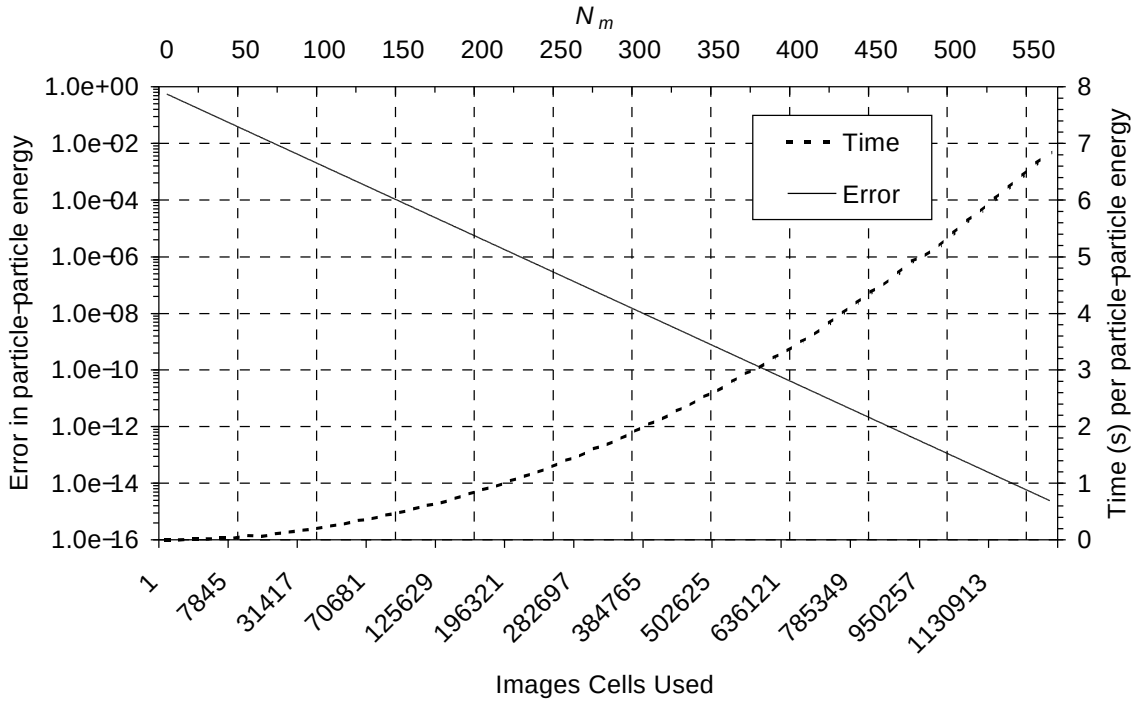

Figure 4.7: Fractional error $(E_\infty - E_n)/E_\infty$ and time taken to compute the energy E_n between two particles separated by a single lattice spacing in an infinitely tiled periodic system when n image cells are used. Here, E_∞ is estimated by allowing the summation to converge to machine accuracy.

Windows NT 4.0. For the particle-particle energy to converge to a relative error better than 1×10^{-8} requires $N_m \sim 300$, which takes approximately $\pi N_m^2 \approx 300,000$ calls to the K_0 function. This ensures that the total system energy is accurate to better than 0.01%.

We now derive a new method to perform this infinite summation. In figure 4.8 we have:

$$\begin{aligned} Z^2 &= (m_x L_x)^2 + (m_y L_y)^2 \\ z^2 &= (x_i - x_j)^2 + (y_i - y_j)^2 \\ \theta &= \tan^{-1}\left(\frac{x_i - x_j}{y_i - y_j}\right) + \frac{\pi}{2} \\ \varphi &= \tan^{-1}\left(\frac{m_y L_y}{m_x L_x}\right). \end{aligned} \tag{4.12}$$

We define

$$\phi = \theta + \varphi$$

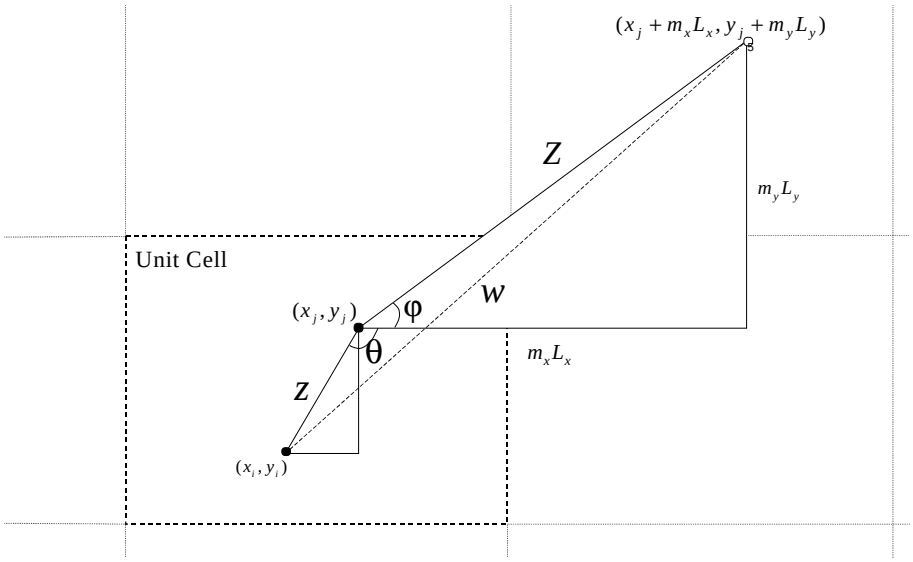

Figure 4.8: Two particles in a unit cell with infinite periodic repeats. Z is the distance from particle i to its own mirror image, z is the distance between i and j, and w is the distance between i and the mirror image of j.

which yields

$$w^2 \;=\; Z^2 + z^2 - 2zZ\cos(\phi). \tag{4.13}$$

We may use the Gegenbauer addition formulae (*Watson*, 1944) to write

$$K_0\left(\frac{w}{\lambda}\right) = \sum_{k=-\infty}^{\infty} K_k\left(\frac{Z}{\lambda}\right) I_k\left(\frac{z}{\lambda}\right)\cos(k\phi) \tag{4.14}$$

for the energy between a particle i and one of the periodic images of j, where I_k and K_k are modified Bessel functions. This formula requires $z \leq Z$, which is automatically satisfied since z is the minimum image distance between i and j. We can therefore write the total energy (4.11) of two particles i and j summed over all periodic images in the form:

$$K_0^*\left(\frac{|\mathbf{r}|}{\lambda}\right) = K_0^*\left(\frac{w}{\lambda}\right) = K_0\left(\frac{z}{\lambda}\right) + \sum_{\substack{m_x,m_y \\ \text{not } m_x=m_y=0}} \sum_{k=\infty}^{\infty} K_k\left(\frac{Z}{\lambda}\right) I_k\left(\frac{z}{\lambda}\right)\cos(k\phi), \tag{4.15}$$

where the case $m_x = m_y = 0$, for which $z \not< Z$, is the contribution to the energy from the unit cell which must be explicitly included as a separate term. Further

re-arrangement and use of (4.13) gives

$$K_0^*\left(\frac{w}{\lambda}\right) = K_0\left(\frac{z}{\lambda}\right) + \sum_{k=-\infty}^{\infty} I_k\left(\frac{z}{\lambda}\right)\left[c_k\cos(k\theta) - s_k\sin(k\theta)\right] \tag{4.16}$$

where

$$\begin{aligned} c_k &= \sum_{\substack{m_x,m_y \\ \text{not } m_x=m_y=0}} K_k\left(\frac{Z}{\lambda}\right)\cos(k\varphi) \\ s_k &= \sum_{\substack{m_x,m_y \\ \text{not } m_x=m_y=0}} K_k\left(\frac{Z}{\lambda}\right)\sin(k\varphi). \end{aligned} \tag{4.17}$$

Equations (4.16) and (4.17) have the remarkable property that the coefficients corresponding to the infinite summation over the periodic repeats of the unit cell can be pre-computed. This reduces the double summation in (4.11) to a single summation. Furthermore, due to the exponential convergence of the Gegenbauer addition formulae, the sum may be truncated at $k_{\text{trunc}} \sim 5 - 20$ terms. A further factor of two in performance can be obtained by using symmetry to convert the summation from $k = -\infty \ldots \infty$ to the range $k = 0 \ldots \infty$.

The form (4.16) closely resembles a Fourier type summation method, yet the whole calculation proceeds in real space in contrast to the Ewald summation method (*Olive and Brandt*, 1998).

The convergence of the energy between two particles in the Abrikosov lattice is identical to the convergence shown in figure 4.7 as we add more terms to the calculation of the coefficients c_k and s_k. We have chosen the case of two nearest neighbours, which yields the slowest convergence of (4.16) since z takes its smallest value.

In a superconductor, λ is a function of the temperature. For our model system ($Mo_{77}Ge_{23}$) $\lambda(T) = \lambda(0)/(1 - T/T_c)^{1/2}$ (*Ryu et al.*, 1996), where $T_c = 5.63$K is the critical temperature at which the material loses its superconducting properties. Hence the coefficients c_k and s_k need to be re-computed at each temperature. As the temperature increases additional image cells need to be included in both (4.11) and the pre-computation (4.17). The crucial difference, however, between (4.11) and (4.16) is that the time taken to evaluate the energy using (4.16) remains virtually constant once the coefficients are available, whereas the na"ıve summation requires considerable numbers of additional image cells to converge to the solution. In figure 4.9 we show the speedup of our method when computing the energy between

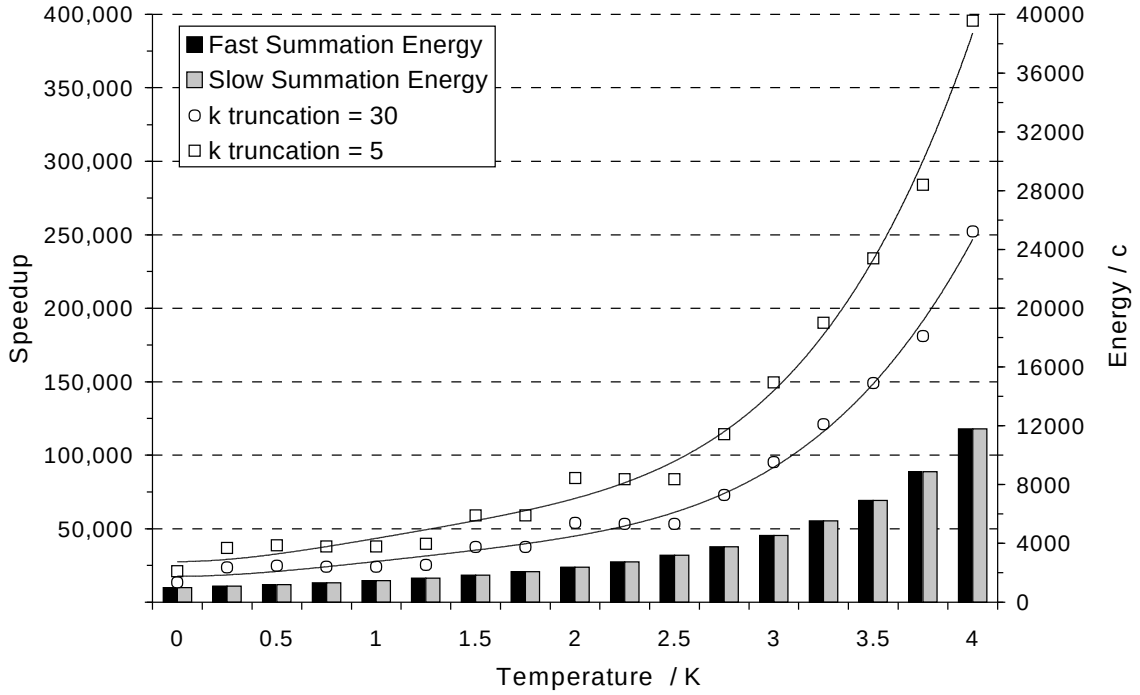

Figure 4.9: Speedup of fast infinite summation method over naïve implementation when the relative error in the energy between each pair of particles is fixed to be 1×10^{-5}: both methods yield identical results.

two particles at a fixed accuracy of 1×10^{-5} (relative to the energy computed to machine accuracy by either method). In all cases the resulting energies are shown to be identical to the stated accuracy. At 0K and using 5 terms in the truncation of (4.16), we have a speedup of 20,000 over the naïve summation method. This rises to 400,000 for temperatures approaching T_c. If the particle energy is required to be accurate to 1×10^{-8}, then, using 30 coefficients, the speedups are between 50,000 (T = 0K) and 1,000,000 ($T \approx T_c$).

Since the coefficients c_k and s_k depend on λ (and hence temperature); the method may appear to be costly if the temperature is changed at every Langevin dynamics or Monte Carlo step. We now discuss several ways to overcome this. Firstly, it is possible to perform Monte Carlo simulations at a small number of temperatures and use the data from these to obtain information about the behaviour of the system as a continuous function of temperature (*Ferrenberg and Swendsen*, 1988, 1989). Thus improving the sophistication of the analysis of the results can reduce the number coefficients c_k and s_k which need to be pre-calculated. Secondly it is possible to compute the c_k and s_k at a small set of temperatures and use interpolation to derive their values at other temperatures. Finally, since only $\sim 5 - 20$ coefficients are needed, it is straightforward to compute once and store on disk the

values of c_k and s_k for each temperature to be explored. These values will be re-used a large number of times in a typical set of numerical simulations.

We implement (4.16) using a recurrence relation (*Press et al.*, 1992) for the trigonometric terms and a vendor-optimised vector Bessel function. Goertzel's algorithm (*Goertzel*, 1958) could be employed for additional efficiency, though the improvement is likely to be marginal. The remarkable speedup obtained is due to the fixed work equivalent to roughly five calls to a Bessel function routine required for (4.16), compared to $\sim 100,000$ calls required for (4.11) (at 0K). The five calls are: two to initialise the Bessel recurrence, one to evaluate the contribution from the unit cell, and the equivalent of roughly a further two for the remaining trigonometric terms. Our infinite summation is correspondingly five times slower than using the smoothed potential in a single unit cell, which requires evaluation of a single Bessel function or a polynomial. This is confirmed by experiments. For simulations using the fast infinite lattice summation, results are similar to those of figure 4.5. The infinite lattice summation method is suitable for quantitative studies of superconductors.

4.7 Results

In the previous sections we have demonstrated that the phenomenological potential and the infinitely summed potential ensure that the Abrikosov lattice is the minimum energy configuration for our system. We now show that the incorrect handling of the long-range potential seriously affects the elastic properties of a lattice.

We have considered a simulation of shearing of a hexagonal lattice, which is a simplified version of the simulations required to perform current-voltage characterisations. Inset (a) in figure 4.10 shows a Delaunay triangulation for half the simulation cell demonstrating the experimental set-up: a shearing force is applied to the central row of particles marked by black points, and the particles marked by open circles are not allowed to move in the x-direction. The main diagram shows the resulting change in energy as a response to the shearing force. The upper part of the figure shows data for the smooth cut-off, and the lower part shows the results for the sharp cut-off. The smooth cut-off and the infinite lattice summation produce the expected behaviour: with increasing shear stress the energy increases. The slope of the energy-change as a function of the displacement characterises the shear elastic modulus of the crystal. Inset (b1) shows a triangulation of a system which has been slightly tilted by the applied force. In contrast, employing the sharp cut-off, the energy decreases for applied shear stress, *i.e.* the material appears to

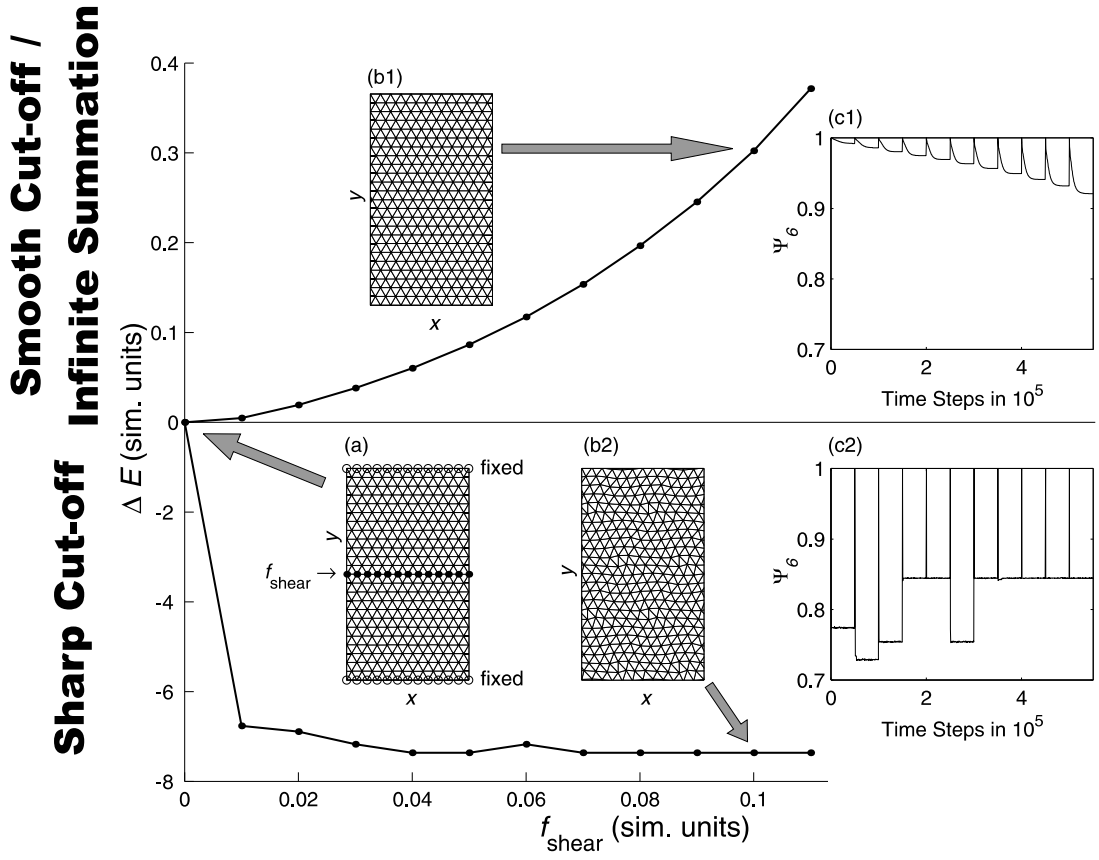

Figure 4.10: Change in energy, ΔE, (in simulation units) as a function of a shearing force, $f_{\rm shear}$, (in simulation units) for the smooth and the sharp cut-off. For the infinite lattice summation we obtain qualitatively similar results. Insets (a), (b1) and (b2) show different snap shots of vortex configurations. Insets (c1) and (c2) show the local hexagonal order, Ψ_6, as the experiment progresses (see text for details).

collapse after applying a shearing force! We show the triangulation of the particle configuration after shearing in inset b2.

Insets (c1) and (c2) show the time evolution of the local hexatic order (section 3.8.7),

$$\Psi_6 = \frac{1}{n_{\rm bond}} \left| \sum_k \exp(i6\theta_k) \right|, \tag{4.18}$$

where the sum runs over all bond angles θ_k in the Delaunay triangulation. Every 50,000 time steps the system starts as a hexagonal lattice ($\Psi_6 = 1$) and a new shearing force is applied for the next 50,000 time steps.

In (c1), which shows results computed using the smoothed potential, Ψ_6 decreases continuously until a static state is reached, reflecting the shearing of the system. The energy data in the main plot are taken from these static states. In (c2) (sharp cut-off) Ψ_6 drops suddenly to a much smaller value, representing the

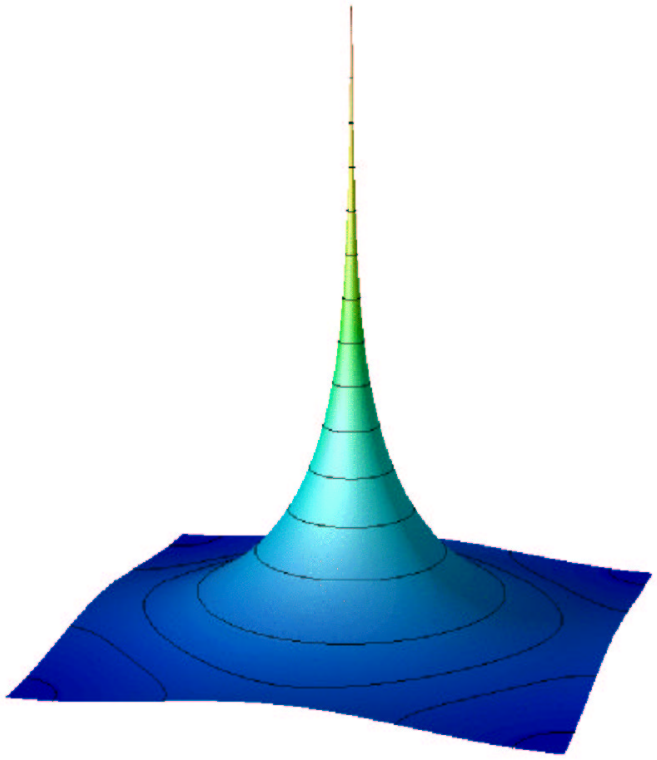

Figure 4.11: Infinite lattice interaction potential $U(\mathbf{r})$ as a function of particle-pair displacement vector $\mathbf{r} \in \mathcal{S}$ within the simulation cell $\mathcal{S}$. For $\mathbf{r} \to \mathbf{0}$ the particles approach each other and feel a strong repulsive force, which is reflected in the divergence in the centre (at $\mathbf{r} = 0$). Note that the isolines are not equally spaced, which reveals the periodicity of the system close to the corners.

sudden change to configurations similar to those shown in (b2). Thus, using a sharp cut-off, the mechanical properties of the lattice are severely affected by the incorrect handling of the long-range potential: this would seriously affect numerical simulations aimed at studying elastic properties of the vortex state in superconductors. The smooth cut-off and the infinite lattice summation produce the correct physical behaviour and can be used in more complex numerical simulations for phenomenological (smoothed potential) or quantitative (infinite summation) studies of the vortex state.

In comparative studies, we have found that it makes no difference whether the infinite lattice summation or the smooth cut-off is used for our simulations (for example, figure 6.11 on page 103 shows the agreement of data computed with either method).

4.8 Efficiency improvements

We describe how to further speed up particle simulations when using an infinite lattice summation (section 4.8.1) and a cut-off (section 4.8.2).

4.8.1 Look-up table for infinite lattice summation

For every interacting particle-pair $(\mathbf{r}_i, \mathbf{r}_j)$ with $i \neq j$, the infinite lattice summation can be seen as computing the interaction between two lattices that are displaced

relative to each other by the displacement vector $\mathbf{r} = \mathbf{r}_i - \mathbf{r}_j$, where the unit cell for the displaced lattices is the simulation cell. The displacement vector $\mathbf{r}$ will always be located within the simulation cell $\mathcal{S} = [-L_x/2, L_x/2] \times [-L_y/2, L_y/2] \subset \mathbb{R}^2$.

We can use this property, and pre-compute a look-up table for (4.16) for all $\mathbf{r} \in \mathcal{S}$. We know that the interaction potential $U(\mathbf{r})$ diverges[1] at $\mathbf{r} = \mathbf{0}$, but varies slowly and smoothly for all other $\mathbf{r} \in \mathcal{S}$. Due to the strong repulsion, particles will not come close to each other so that it is not necessary to pay special attention to the divergence.

Figure 4.11 shows the infinite lattice interaction potential $U(\mathbf{r})$ with $\mathbf{r} \in \mathcal{S}$ for a logarithmic particle interaction as described by *Grønbech-Jensen* (1996), which shows qualitatively the same features as the infinite-lattice interaction potential for K_0, only with the central divergence decaying slower with increasing $\mathbf{r}$. The figure demonstrates the regularity of this function for $\mathbf{r} \neq \mathbf{0}$.

Such a smooth function (apart from $\mathbf{r} = \mathbf{0}$) can easily be interpolated by a two-dimensional look-up table using bi-linear or bi-cubic interpolation for intermediate positions. In the beginning of a simulation, we have a small overhead to compute the look-up table which can be done within a couple of minutes (for 600 particles, 2000 table-entries per area occupied by one particle, on a 700 MHz PIII). However, subsequently we profit strongly from the look-up table: it is (i) about as fast as the smooth cut-off, and (ii) we can pre-compute the table with a high accuracy without slowing down the subsequent main computation.

4.8.2 Neighbour list for smooth cut-off

Having confirmed that using a (smooth) cut-off is an appropriate method to study a system, one can consider to cut off the interaction not at the largest possible value (*i.e.* half the simulation cell size), but for example at a distance of 10 lattice spacings. It is advisable to perform finite size scaling to ensure that this does indeed not affect the system. Having done so, we can keep a neighbour list for every particle which keeps all particles within the cut-off range and particles just outside the cutoff range. This method is known as a Neighbour-list or Verlet-list (*Verlet*, 1967).

The left plot in figure 4.12 demonstrates the concept of the skin layer. In the very first time-step, we create the neighbour lists. Subsequently, in every time step

[1] We do not take into account here the attraction that real vortices experience when their cores start to overlap.

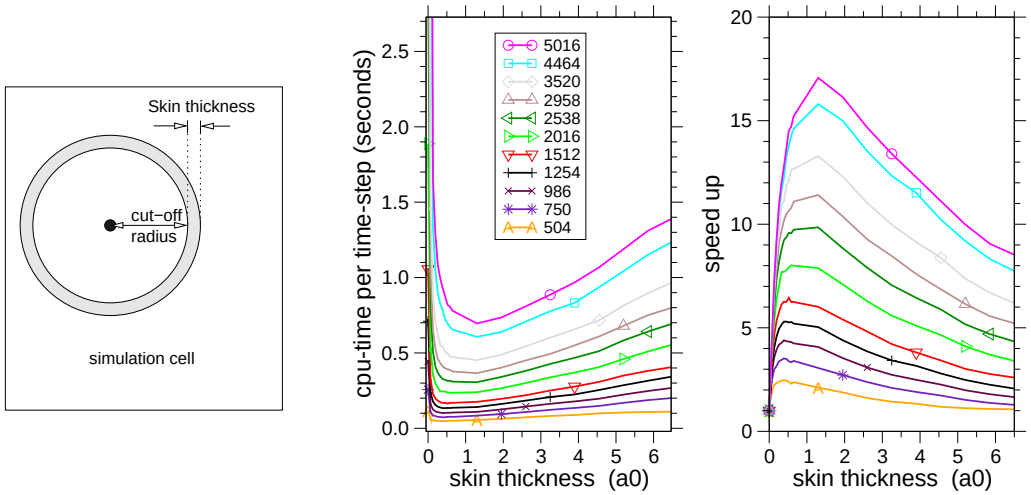

Figure 4.12: *Left:* For the neighbour look-up, we keep for each particle a list containing all other particles inside the cut-off circle and inside the skin-layer (shaded in gray). *Middle:* Performance results for a cut-off at $6.5a_0$, where a_0 is the average particle spacing. The thickness of the skin-layer has been varied from 0 to $6.5a_0$. Each line is for another number of particles, as indicated in the legend. *Right:* Speed-up relative to using no neighbour list. The optimum skin thickness varies with the system size, and shifts from $\approx 0.4a_0$ for 504 particles to $\approx 1.5a_0$ for 5016 particles.

n, we find the maximum displacement Δr^n

$$\Delta r^n = \max_i |\dot{\mathbf{r}}_i^n \Delta t| \tag{4.19}$$

where $\dot{\mathbf{r}}_i^n$ is the velocity of particle i in time-step n. We recompute the neighbour list when

$$\sum_n \Delta r^n \geq d_{\text{skin}} \tag{4.20}$$

where d_{skin} is the thickness of the skin-layer. To compute the interaction of a particle with all others, we now only consider particles within the cut-off circle and within the skin-layer, and these can be looked up quickly from the neighbour list.

Apart from the re-computation of the neighbour list, the time complexity scales linear with the number of particles for a given cut-off and a fixed thin thickness. The performance data shown in figure 4.12 help us to chose the optimum skin-thickness: if the skin-layer is too thick, then many unnecessary interaction computations are attempted with the particles in the skin-layer. On the other hand, if the skin-layer is too thin, then the neighbour list needs to be updated very frequently, which is quite expensive. The data show that even for small systems there is a performance gain using the neighbour look-up, and for large systems it can be substantial. Even if the cut-off is chosen to be half the system size, there is still a performance increase

by using a thin skin-layer in comparison to not using a neighbour list.

4.9 Conclusions

For particle-particle simulations using long-range interactions subject to periodic boundary conditions, a sharp cut-off for the interaction energy (or force) can yield misleading results. We have considered the case of superconductors, in which the potential is governed by a Bessel function. Monte Carlo and molecular dynamics simulations are often used to study phase diagrams numerically and it is vital that the phase behaviour of the system is not affected by the model itself. We find that using a sharp cut-off the system can find irregular lattice configurations with an energy below the theoretical ground state of a regular hexagonal lattice. Therefore, the (dynamical) phase diagram of the system under investigation can be dramatically affected by incorrect handling of the long-range potential.

We have presented two methods which overcome these problems. The first is suitable for phenomenological studies of systems and uses a smoothed potential, but still truncates the interaction over a single unit cell. Annealing a system governed by this modified potential yields a perfect hexagonal lattice which is the global energy minimum. This is the least computationally expensive option and is applicable to any potential. The second method sums the interaction over the infinitely tiled unit cell and is suitable for quantitative system studies. Previous methods for performing this, add the tiled images in a series of shells of increasing radius. We have shown that with the pre-computation of a set of Fourier type coefficients, the whole infinite summation can be computed using a summation which converges exponentially fast and results in a speed-up of between 20,000 and 1,000,000 over the naïve summation, depending on the range of the interaction and the desired accuracy. The derivation of the summation proceeds in real space, and the results converge exactly to those obtained from other summation methods. This is roughly five times as slow as using the smoothed potential, but is the most accurate method for systems of finite size. Both methods can be made faster by using looking look-up tables for the interaction (infinite lattice summation) and for neighbours (smooth cut-off). The suggested methods have been used in chapter 5 and 6 of this report, and in a number of other works (*Price et al.*, 2000, *Fangohr et al.*, 2001a, *Molinari et al.*, 2001, *Fruchter*, 2002b,a, *Grigorenko et al.*, 2002).

Chapter 5

Two-dimensional studies: The critical transverse force in weakly pinned driven vortex systems

Preface

The work described in this chapter has been published in *Fangohr, de Groot and Cox* (2001b). For this report we have slightly extended the introduction, and shorted section 5.2 as it duplicates information given already in Chapter 3. For clarity, section 5.4.7 is extended compared to the published version.

5.1 Introduction

The vortex state is dominated by the competition of ordering and disordering interactions. Vortex-vortex repulsion tends to order the system whereas thermal fluctuations and pinning from material imperfections introduce disorder into the vortex lattice. Recently, interest has developed in the nature of the non-equilibrium states and dynamical phases in the presence of a Lorentz force driving the system. There is evidence from experiments (*Bhattacharya and Higgins*, 1993, *Yaron et al.*, 1994, *Hellerqvist et al.*, 1996, *Pardo et al.*, 1997), simulations (*Jensen et al.*, 1988, *Koshelev and Vinokur*, 1994, *Moon et al.*, 1996, *Ryu et al.*, 1996, *Olson et al.*, 1998b) and theory (*Koshelev and Vinokur*, 1994, *Giamarchi and Le Doussal*, 1996, *Balents et al.*, 1998) that for small driving forces the vortex system is disordered and shows turbulent plastic flow, and that for larger driving forces the system becomes ordered and shows elastic flow (see section 2.5 for details). For the ordered system *Koshelev and Vinokur* (1994) proposed that the vortices may form a moving hexagonal crystal. Subsequently, *Giamarchi and Le Doussal* (1996) predicted that

this highly driven phase may be a topologically ordered moving glass (the moving Bragg glass) in which vortices move in elastically coupled static channels like beads on a string (figure 2.10 on page 19). It was also suggested (*Balents et al.*, 1997, 1998, *Le Doussal and Giamarchi*, 1998, *Scheidl and Vinokur*, 1998) that the motion of vortices in different channels may be decoupled (the moving transverse glass) and thus shows smectic order (figure 2.11). In computer simulations (*Moon et al.*, 1996, *Ryu et al.*, 1996, *Olson et al.*, 1998b) and in experiments (*Pardo et al.*, 1998, *Troyanovski et al.*, 1999) both the moving transverse glass (MTG) with de-coupled channels and the moving Bragg glass (MBG) with coupled channels have been observed.

A remarkable property of the moving glass (with either coupled or de-coupled channels) is that, in the presence of random pinning and once the static channels are established, the application of a small force transverse to the direction of motion does not result in transverse motion (*Giamarchi and Le Doussal*, 1996, *Le Doussal and Giamarchi*, 1998) as described in section 2.6. Only if a critical transverse force has been exceeded, is the system transversely depinned. Computer simulations have demonstrated the existence of such a critical transverse force for random pinning (*Moon et al.*, 1996, *Ryu et al.*, 1996, *Kolton et al.*, 1999, *Olson and Reichhardt*, 2000), and for periodic pinning (*Reichhardt and Nori*, 1999, *Marconi and Domínguez*, 1999).

In this work we use a more realistic representation of random pinning in high purity single crystals used in fundamental studies of vortex dynamics; we investigate regimes with a high density of vortices with long-range logarithmic vortex-vortex interaction potentials as in *Kolton et al.* (1999) and we employ a weak smoothly varying pinning potential rather than many strong point-like pins as in *Moon et al.* (1996), *Ryu et al.* (1996), *Kolton et al.* (1999) and *Olson and Reichhardt* (2000). We find and explain that the magnitude of the critical transverse force is of the order of 10% of the static depinning force in the regime investigated, in contrast to previous works (*Moon et al.*, 1996, *Ryu et al.*, 1996, *Olson and Reichhardt*, 2000) which report it to be $\approx 1\%$. We report on novel results for the critical transverse force in the presence of weak pinning which (i) verify the theory of *Giamarchi and Le Doussal* (1996) and (ii) provide the first numerical data which may be compared directly with current experimental efforts to demonstrate the existence of the critical transverse force.

In section 5.2 we describe our method, and in section 5.3 the random pinning potential we have used. Section 5.4 presents the results, and we summarise our

conclusions in section 5.5.

5.2 Langevin dynamics simulation

We model the vortex motion of a two-dimensional system with over-damped Langevin dynamics. The total force acting on vortex i is given by

$$\mathbf{F}_i = -\eta \mathbf{v}_i + \mathbf{F}^{\mathrm{L}} + \mathbf{F}_i^{\mathrm{vv}} + \mathbf{F}_i^{\mathrm{vp}} + \mathbf{F}_i^{\mathrm{therm}} = \mathbf{0}, \tag{5.1}$$

where η is the viscosity coefficient, $\mathbf{v}_i$ the velocity, $\mathbf{F}^{\mathrm{L}}$ the Lorentz force, $\mathbf{F}_i^{\mathrm{vv}}$ the vortex-vortex interaction, $\mathbf{F}_i^{\mathrm{vp}}$ the vortex-pinning interaction, and $\mathbf{F}_i^{\mathrm{therm}}$ a stochastic noise term to model temperature. The vortex-vortex interaction force appropriate for rigid vortices in thin films and pancakes in decoupled layers of layered materials is effectively (section 2.3.3)

$$\mathbf{F}_i^{\mathrm{vv}} = 2\epsilon_0 s \sum_{j \neq i} \frac{\mathbf{r}_i - \mathbf{r}_j}{|\mathbf{r}_i - \mathbf{r}_j|^2}. \tag{5.2}$$

ϵ_0 is given in (2.4) and s the length of the vortex. We employ periodic boundary conditions and cut off the logarithmic vortex-vortex repulsion potential at half the system size. It is important to reduce the vortex-vortex interaction near the cut-off distance smoothly to zero (section 4.3). We investigate systems with a magnetic induction of $B = 1$ T and a penetration depth of $\lambda = 1400$Å which yields a vortex density of $\approx 10/\lambda^2$. System sizes from 100 to 3000 vortices have been investigated. Forces are expressed in units of the force, f_0, that two vortices separated by λ experience.

5.3 Random pinning

We use a random pinning potential that varies smoothly on a length scale of $\lambda/25$, which is of the order of the coherence length ξ. This is a representation of random pinning on the atomic length scale (for example due to oxygen vacancies or small clusters of oxygen vacancies) since the vortex cores effectively smooth the pinning potential over a length scale of the core diameter 2ξ. Figure 5.1 (a) demonstrates the construction of the pinning potential in one dimension. Figure 5.1 (b) shows a part of the pinning structure used for the two dimensional system. The root mean square value of the corresponding pinning forces is denoted by $F_{\mathrm{rms}}^{\mathrm{vp}}$.

This choice of the pinning potential is more realistic for high-quality single crystal samples than the pinning of few, relatively strong point-like pinning centres. We demonstrate the different shapes of the pinning potential in figure 5.2.

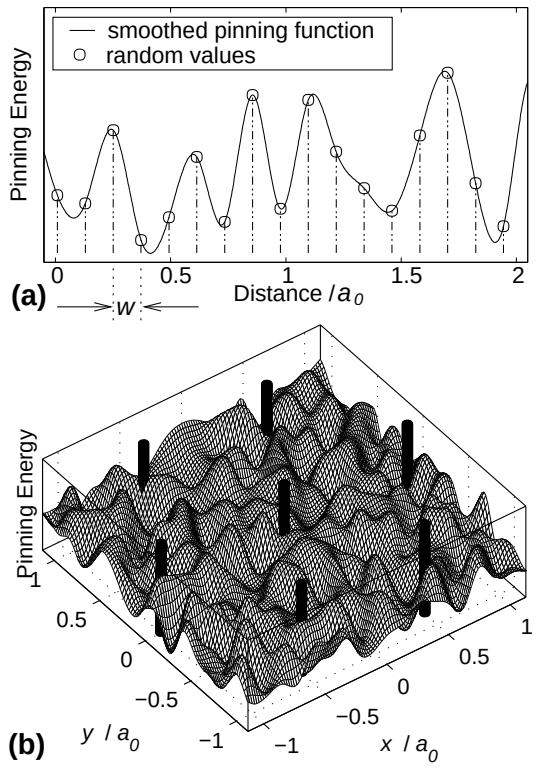

Figure 5.1: A sample pinning potential. Distances are given in multiples of the vortex lattice spacing, a_0. *(a)* Demonstration of construction of the pinning potential in one dimension: firstly, we assign random pinning energies at discrete sites (shown as open circles) with spacing w. Secondly, we interpolate between those sites using cubic splines to obtain an effectively continuous pinning potential. This results in a random pinning potential with a short-range correlator $\overline{V(r)V(r')} = g(r - r')$ of range w. We follow an analogous procedure in two dimensions. *(b)* A part of a pinning potential as used in the simulations. The seven black cylinders indicate vortex lines separated by a_0 to demonstrate the length scale.

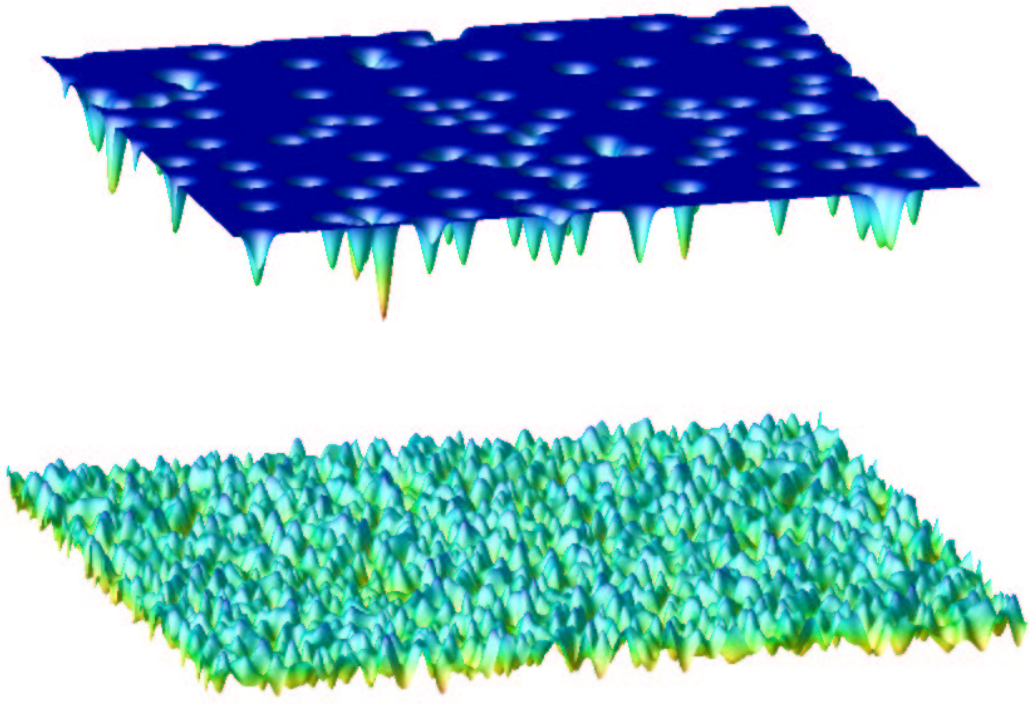

Figure 5.2: Comparison of different pinning potentials. *Top:* Point-like pinning centres as employed by most other simulations of the vortex state. Parameters taken from *Olson et al.* (1998b), *Olson and Reichhardt* (2000). *Bottom:* Smoothly varying pinning potential as used in this work. Both plots show an area which is occupied by ≈ 90 vortices.

5.4 Results

5.4.1 Simulation scenario

Initially, we anneal the vortex system in the presence of random pinning from a molten state to zero temperature. Then a driving force is applied which is increased every $4 \cdot 10^4$ time steps. With increasing driving force we find a pinned system, turbulent plastic flow and finally the moving Bragg glass (see figure 2.13 on page 21 for a phase diagram, and figure 2.10 for the moving Bragg glass).

For sufficiently strong pinning there is an intermediate regime between turbulent plastic flow and the moving Bragg glass (MBG), in which the vortex motion in different channels is decoupled (*Fangohr et al.*, 2001a). This is called the moving transverse glass (MTG) because the transverse order remains (see figure 2.11). We find a critical transverse force for both the MBG and the MTG. Here, we report on the small pinning strengths at which only the MBG is observed in our simulations.

A representation of the time-averaged paths of the vortices in the moving Bragg glass phase is shown in figure 5.3. A snap-shot of vortex positions in one time-step is shown in figure 5.4. These simulation results agree very well with the prediction shown in figure 2.10 on page 19.

To find the critical transverse force we start with a MBG driven by a constant force $F_{\mathrm{x}}^{\mathrm{L}}$ in the x-direction and slowly increase the transverse force $F_{\mathrm{y}}^{\mathrm{L}}$ in the y-direction, until the system starts moving transversely. The lower ends of the bars shown in figure 5.5 to 5.8 represent the largest probed transverse force which did not yield any transverse motion, and the upper ends of the bars show the smallest transverse force that could depin the system transversally.

5.4.2 Finite-size effects

Figure 5.5 on page 74 shows that there is a decrease in the ratio of the critical transverse force $F_{\mathrm{y}}^{\mathrm{c}}$ to the static depinning force $F_{\mathrm{x}}^{\mathrm{c}}$ for system sizes below 1000 vortices. However, for larger systems this ratio remains constant, showing that the observed $F_{\mathrm{y}}^{\mathrm{c}}$ is not a finite-size effect. We have increased the cut-off with the system size to ensure that effects due to the long-range interactions between the additional particles in the simulation are taken into account, which contrasts to a similar finite-size study (*Olson and Reichhardt*, 2000) where the cut-off for the vortex-vortex interaction was kept constant and the results were reported to be independent of the system size.

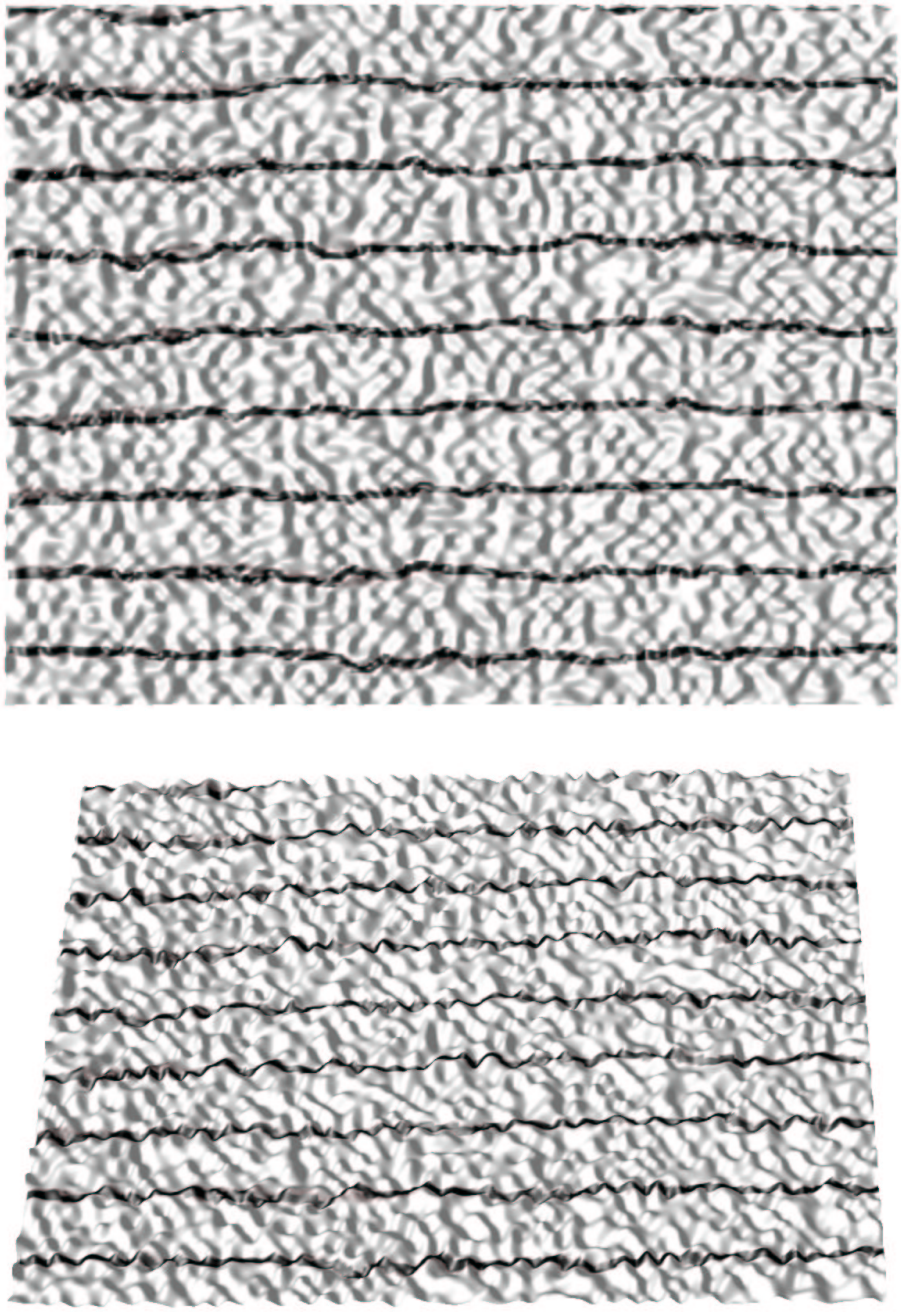

Figure 5.3: The moving Bragg glass. *Top:* The rendered wavy surface represents the pinning potential shown in figure 5.1 on page 71 and in the lower plot of figure 5.2. The surface is coloured in black where there is a high probability of finding a vortex and white where the probability is zero. The driving force F_x^L is acting from the left to the right, and vortices follow on average the direction of the force, but the paths in which they move show a certain roughness. These data are consistent with the prediction shown in figure 2.10 on page 19. *Bottom:* Same as the top-image, but from a slightly changed viewpoint. This projection allows to see where vortices travel "in" the pinning potential. It can be seen that vortices avoid areas with a high pinning potential if possible.

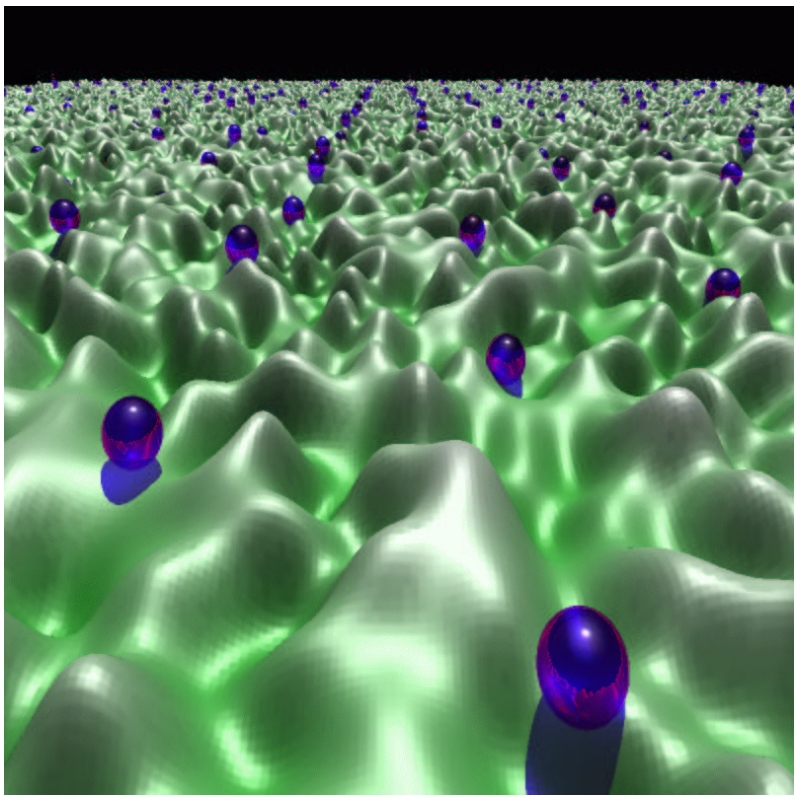

Figure 5.4: Vortices are represented by spheres, and are plotted on top of the pinning potential. Shown is one time step of a moving Bragg glass. Note that the vortices align in the viewing direction which coincides with the direction of the driving force, which is in agreement with figure 2.10.

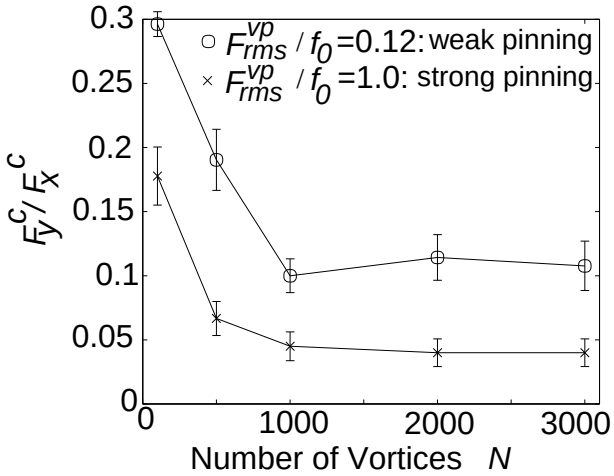

Figure 5.5: The ratio of the critical transverse force $F_{\mathrm{y}}^{\mathrm{c}}$ to the static depinning force $F_{\mathrm{x}}^{\mathrm{c}}$ for various numbers of vortices, N. The lower curve is for strong pinning with $F_{\mathrm{rms}}^{\mathrm{vp}}/f_0 = 1.0$ and the upper curve is for weak pinning with $F_{\mathrm{rms}}^{\mathrm{vp}}/f_0 = 0.12$.

5.4.3 Magnitude of critical transverse force

Previous estimates (*Moon et al.*, 1996, *Ryu et al.*, 1996, *Olson and Reichhardt*, 2000) for the ratio $F_{\mathrm{y}}^{\mathrm{c}}/F_{\mathrm{x}}^{\mathrm{c}}$ give a value ≈ 0.01. We find $F_{\mathrm{y}}^{\mathrm{c}}/F_{\mathrm{x}}^{\mathrm{c}} \approx 0.1$ and identify two reasons for this order of magnitude discrepancy. Firstly, we study the weak pinning regime in which the hexagonal structure of the *static* vortex system (*i.e.* without an applied driving force) is not completely destroyed due to the vortex pinning, whereas previous studies focused on the strongly pinned regime in which the *static* system is strongly disordered. Both systems — with weak and strong pinning — move elastically and show topological order under the influence of the driving force in the x-direction. The critical force required to depin the static system, $F_{\mathrm{x}}^{\mathrm{c}}$, is greater for the strongly pinned system which shows disorder, because a disordered system can adapt better to the pinning potential. However, the force required to depin the moving system transversely, the critical transverse force $F_{\mathrm{y}}^{\mathrm{c}}$, depends less strongly on the pinning strength because the elastically moving system is topologically ordered for either pinning strength. Thus, the ratio $F_{\mathrm{y}}^{\mathrm{c}}/F_{\mathrm{x}}^{\mathrm{c}}$ is higher for weak pinning. We demonstrate this in figure 5.5 on the preceding page where we show that the change from strong to weak pinning increases the ratio $F_{\mathrm{y}}^{\mathrm{c}}/F_{\mathrm{x}}^{\mathrm{c}}$ by a factor 2 to 3. Secondly, the pinning potentials employed by *Moon et al.* (1996), *Ryu et al.* (1996) and *Olson and Reichhardt* (2000) consist of (strong) point-like randomly distributed pins (as shown in the top of figure 5.2), which we find increase the static depinning force $F_{\mathrm{x}}^{\mathrm{c}}$ by another factor 2 to 3 compared with using a smoothly varying pinning potential (bottom in figure 5.2). We would thus get to the same order of magnitude for the ratio $F_{\mathrm{y}}^{\mathrm{c}}/F_{\mathrm{x}}^{\mathrm{c}}$ as *Moon et al.* (1996), *Ryu et al.* (1996) and *Olson and Reichhardt* (2000) if we used the simulation scenario they employed. We find that for different random pinning configurations the critical transverse force can vary up to a factor 2 in the weak pinning limit.

5.4.4 Critical transverse force can be an order parameter

Figure 5.6 on the next page shows the variation of F_{y}^{c} as a function of the pinning strength for systems driven with a constant driving force $F_{\mathrm{x}}^{\mathrm{L}} = 0.3 f_0$ in the x-direction. The absence of transverse barriers for zero pinning strength shows that it is not the (periodic) boundary conditions which result in a critical transverse force. With increasing pinning strength, F_{y}^{c} increases linearly until it starts to decay for pinning strengths of $F_{\mathrm{rms}}^{\mathrm{vp}} \approx 0.25 f_0$ and reaches zero at $F_{\mathrm{rms}}^{\mathrm{vp}} \approx 0.35 f_0$. The decay of the F_{y}^{c} is caused by the strength of the pinning producing turbulent plastic flow of the vortices: in this region the MBG breaks down. This is demonstrated by the second curve in figure 5.6 which shows that the fraction of vortices that are

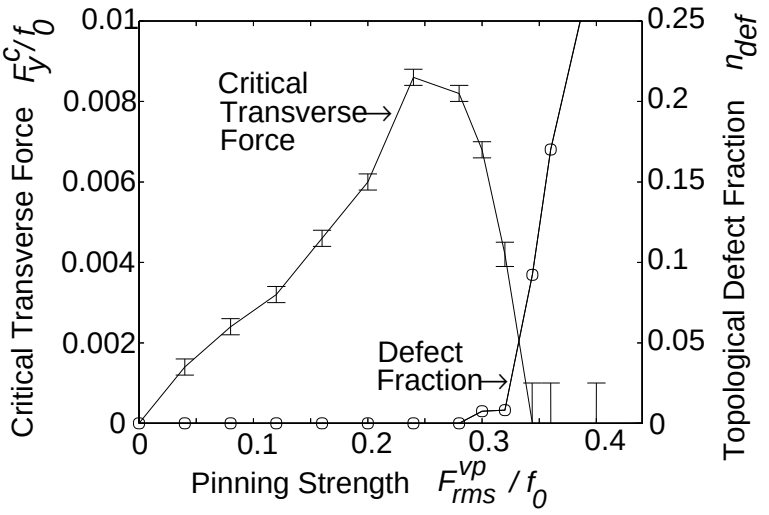

Figure 5.6: Critical transverse force and topological defect fraction n_{def} as a function of pinning strength. The critical transverse force reduces to zero where the system changes from elastic flow to turbulent plastic flow and the number of topological defects increases rapidly.

topological defects, n_{def}, increases rapidly for pinning strengths greater than $0.325 f_0$. We define a topological defect to be a vortex which does not have six nearest neighbours in the periodic Delaunay triangulation of the vortex positions. The slight increase of n_{def} for pinning strengths $0.3 f_0$ and $0.325 f_0$ is due to strong temporary deformations of the MBG such that pairs of topological defects appear next to each other and disappear after a few time steps. This indicates the weakness of the MBG, but not its breakdown (because the system shows elastic motion). In contrast, the transition to turbulent plastic flow is accompanied by a proliferation of topological defects. This confirms theoretical expectations (*Le Doussal and Giamarchi*, 1998) that the critical transverse force, F_{y}^c, can be used as an order parameter for the moving glass, which, in the weak pinning regime, is represented by the MBG. The data shown in figure 5.6 are obtained for a system of 576 vortices. For larger systems we get qualitatively the same curves, with a slightly reduced height of F_{y}^c.

5.4.5 Dependence on longitudinal velocity of moving Bragg glass

Le Doussal and Giamarchi (1998) predicted that the critical transverse force, $F_{\mathrm{y}}^{\mathrm{c}}$, depends on the longitudinal velocity, v_{x}, in a way that F_{y}^c decays with increasing v_{x}. For an isotropic system one expects that the critical "transverse" force $F_{\mathrm{y}}^{\mathrm{c}}$ for a static system is the same as the critical force (acting in any direction) that is required to depin the system. Our computations confirm that in particular $F_{\mathrm{y}}^{\mathrm{c}} = F_{\mathrm{x}}^{\mathrm{c}}$ for a static system. However, as soon as the system of vortices is depinned and moves elastically in the x-direction, the critical transverse force reduces to much smaller

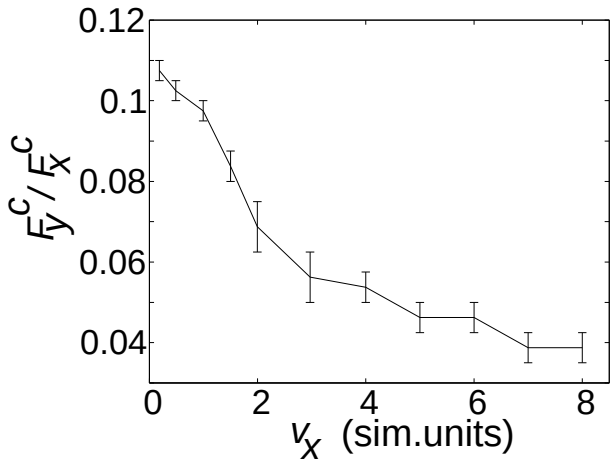

Figure 5.7: Critical transverse force F_{y}^{c} normalised by the static depinning force F_{x}^{c} for various longitudinal velocities v_{x} in the moving Bragg glass regime.

values because the system is not sticking to the pinning potential, but is depinned in the x-direction.

Figure 5.7 shows results of our simulations using a pinning strength of $F_{\mathrm{rms}}^{\mathrm{vp}} = 0.12 f_0$ and a system size of 1200 vortices. We could not resolve the smallest velocities because these are computationally expensive, and we have omitted the datum at $v_{\mathrm{x}} = 0$. The curve starts for small v_{x} with a $F_{\mathrm{y}}^{\mathrm{c}}$ of $\approx 10\%$ of the static depinning force $F_{\mathrm{x}}^{\mathrm{c}}$. With increasing v_{x}, we find that F_{y}^{c} decreases quickly up to velocities of approximately 2 simulation units, and then F_{y}^{c} decreases less strongly for larger velocities. Our findings are compatible with the prediction that the critical transverse force decays for higher velocities as additional dynamic disorder weakens the transverse barriers (*Le Doussal and Giamarchi*, 1998).

The velocities given here in simulation units are directly comparable with the data shown in *Fangohr et al.* (2001a) and comparable with the phase-diagram[1] in figure 2.13, where 0.1 represents a small velocity for the system, and 10 is large. Figure 5.7 suggests therefore that small driving forces are most appropriate for an experimental verification of the critical transverse force, because F_{y}^{c} will be large and easier to detect.

It is worth noting that using a system size of less than 1000 vortices (figure 5.5) gives qualitatively different results; for such small systems the $F_{\mathrm{y}}^{c}(v_x)$ in figure 5.7 remains constant above a small velocity of $v_x \approx 0.3$ simulation units, which is a finite size effect.

[1]Note that due to the scaling chosen (3.37), for forces much larger than the depinning force, $\tilde{v} \approx \tilde{F}^{\mathrm{drive}}$. This is especially the case for driving forces large enough to result in a moving Bragg glass.

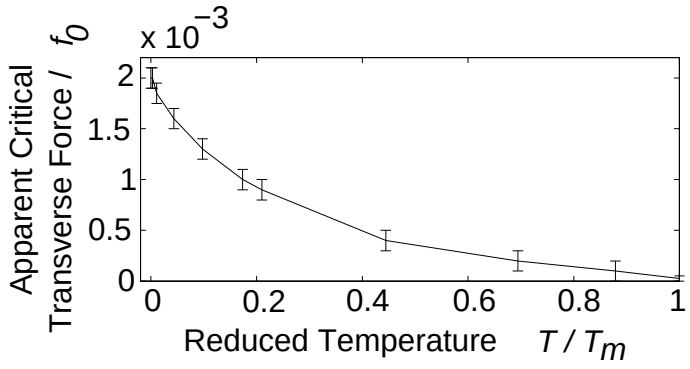

Figure 5.8: Apparent critical transverse force as a function of reduced temperature T/T_m.

5.4.6 Finite temperatures

For finite temperatures it is predicted (*Le Doussal and Giamarchi*, 1998) that there is no true critical transverse force but all transverse stimuli result in a small response in the transverse motion of the system, as shown in figure 2.14 on page 22. However, there is a transverse force at which the transverse velocity increases much stronger than linearly with the transverse drive. This transverse force is the *apparent* critical transverse force, and can be seen in figure 2.14 where the slope of the $T>0$-curve increases to approach the $T=0$-curve.

Data on the apparent critical transverse force in figure 5.8 show that it decays with increasing temperature and vanishes at the melting temperature of the system. The depinning force of the static system, $F_{\mathrm{x}}^{\mathrm{c}}$, decays similarly with increasing temperature, such that $F_{\mathrm{x}}^{\mathrm{c}}/F_{\mathrm{y}}^{\mathrm{c}} \approx \text{const}$.

5.4.7 Experimental verification

The existence of a critical transverse force has yet to be confirmed experimentally. The required experiments are complicated to perform as one has to measure a very small transverse voltage resulting from the application of small transverse currents. Additionally, at finite temperatures no true critical transverse force is expected, but only an "apparent" critical transverse force (section 5.4.6). The samples in question have complicated current-voltage characteristics. Writing $\mathbf{V} = (V_{\mathrm{x}}, V_{\mathrm{y}})$ for the longitudinal and transverse components of the measured voltage, and $\mathbf{I} = (I_{\mathrm{x}}, I_{\mathrm{y}})$ for the applied currents, this means that

$$\mathbf{V} = \mathbf{V}(\mathbf{I}) \tag{5.3}$$

is a nontrivial vector-valued function.

Thus, it is hard to say whether a small transverse voltage is a signature of transverse barriers, or whether at such a small current this is the normal response. In order to resolve this issue we define the new observable, σ, to be the differential

transverse resistance $R_{\mathrm{y}}^{\mathrm{diff}} = \frac{\mathrm{d}v_{\mathrm{y}}}{\mathrm{d}F_{\mathrm{y}}^{\mathrm{L}}}$ normalised by the longitudinal resistance $R_{\mathrm{x}} = \frac{v_{\mathrm{x}}}{F_{\mathrm{x}}^{\mathrm{L}}}$:

$$\sigma = \frac{R_{\mathrm{y}}^{\mathrm{diff}}}{R_{\mathrm{x}}} = \frac{\frac{\mathrm{d}V_{\mathrm{y}}}{\mathrm{d}I_{\mathrm{y}}}}{\frac{V_{\mathrm{x}}}{I_{\mathrm{x}}}}. \tag{5.4}$$

The experimentally measured voltage, V, is proportional to the vortex velocity, v, and the applied current, I, is proportional to the driving force, F, in the simulation. The differential resistance can be measured either by taking numerically the derivative of the resistance, or by applying an ac-current with a dc-offset using lock-in techniques.

We will now prove that the current-voltage characteristic $\mathbf{V}(\mathbf{I})$ cannot be isotropic, if $\sigma < 1$. If $\mathbf{V}(\mathbf{I})$ is anisotropic then there are transverse barriers and hence a critical transverse force (assuming the sample has no extended defects or other intrinsic anisotropy within the layers).

Proof: Assume that the current voltage relation $\mathbf{V}(\mathbf{I})$ is isotropic. It can then be written as

$$V_i = I_i \rho(I) \qquad \text{with} \qquad i = \mathrm{x}, \mathrm{y} \tag{5.5}$$

where we use the notation $I = |\mathbf{I}| = \sqrt{I_\mathrm{x}^2 + I_\mathrm{y}^2}$. The resistivity function $\rho(I)$ is non-negative, and monotonically increasing with I. Therefore,

$$\frac{\partial \rho}{\partial I}(I) \geq 0. \tag{5.6}$$

We find

$$\begin{aligned} R_\mathrm{y}^\mathrm{diff} = \frac{\mathrm{d}V_\mathrm{y}}{\mathrm{d}I_\mathrm{y}} &\overset{(5.5)}{=} \rho(I) + I_\mathrm{y} \frac{\mathrm{d}\rho}{\mathrm{d}I_\mathrm{y}}(I) && (5.7)\\ &= \rho(I) + I_\mathrm{y} \frac{\partial \rho}{\partial I}(I) \frac{\partial I}{\partial I_\mathrm{y}} && (5.8)\\ &= \rho(I) + I_\mathrm{y} \frac{\partial \rho}{\partial I}(I) \frac{I_\mathrm{y}}{I} && (5.9)\\ &= \rho(I) + \frac{I_\mathrm{y}^2}{I} \frac{\partial \rho}{\partial I}(I) && (5.10) \end{aligned}$$

where in (5.9) we have used

$$\frac{\partial I}{\partial I_\mathrm{y}} = \frac{\partial}{\partial I_\mathrm{y}} \sqrt{I_\mathrm{x}^2 + I_\mathrm{y}^2} = \frac{I_\mathrm{y}}{I} \tag{5.11}$$

Eventually,

$$\sigma = \frac{\frac{\mathrm{d}V_\mathrm{y}}{\mathrm{d}I_\mathrm{y}}}{\frac{V_\mathrm{x}}{I_\mathrm{x}}} = \frac{\rho(I) + \frac{I_\mathrm{y}^2}{I} \frac{\partial \rho}{\partial I}(I)}{\rho(I)} = 1 + \frac{\frac{I_\mathrm{y}^2}{I} \frac{\partial \rho}{\partial I}(I)}{\rho(I)} \geq 1 \tag{5.12}$$

Thus, $\sigma \geq 1$ for an isotropic $\mathbf{V}(\mathbf{I})$. On the contrary, if $\sigma < 1$, then the current voltage relation must be anisotropic. □

To assist in the experimental demonstration of the existence of the critical transverse force, we provide in figure 5.9 data on σ. We use central differences to approximate the differential transverse resistance numerically

$$R_\mathrm{y}^\mathrm{diff} = \frac{\mathrm{d}v_\mathrm{y}}{\mathrm{d}F_\mathrm{y}^\mathrm{L}} \approx \frac{v_\mathrm{y}(F_\mathrm{y}^\mathrm{L} + \Delta) - v_\mathrm{y}(F_\mathrm{y}^\mathrm{L} - \Delta)}{2\Delta} \tag{5.13}$$

where Δ is a small change in force. We compute $\sigma = R_\mathrm{y}^\mathrm{diff}/R_\mathrm{x}$, which is a function

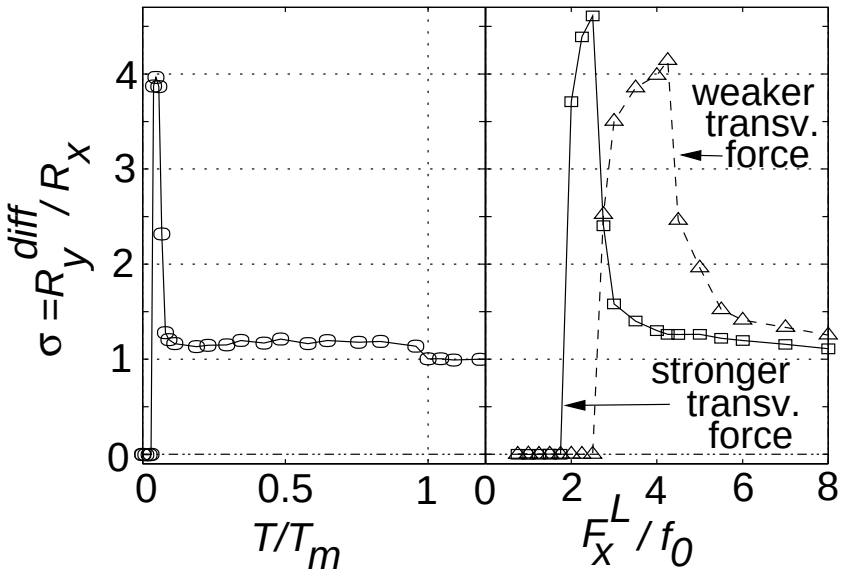

Figure 5.9: Differential resistance in transverse direction normalised by resistance in longitudinal direction as a function of reduced temperature (left) and of strength of the longitudinal driving force (right). See text for details.

of temperature, T, and both components, $F_{\rm x}^{\rm L}$ and $F_{\rm y}^{\rm L}$, of the driving force: $\sigma = \sigma(T, F_{\rm x}^{\rm L}, F_{\rm y}^{\rm L})$. We choose a small transverse force, $F_{\rm y}^{\rm L}$, and keep it constant for each curve in figure 5.9. In the left plot we show $\sigma(T, F_{\rm x}^{\rm L}{=}1f_0, F_{\rm y}^{\rm L}{=}0.00225f_0)$, *i.e.* we vary the temperature T. And in the right plot we show two curves with slightly different transverse forces at zero temperature: $\sigma(T{=}0, F_{\rm x}^{\rm L}, F_{\rm y}^{\rm L}{=}0.00225f_0)$ and $\sigma(T{=}0, F_{\rm x}^{\rm L}, F_{\rm y}^{\rm L}{=}0.00275f_0)$, *i.e.* we vary the longitudinal driving force $F_{\rm x}^{\rm L}$. Note that for all data shown in figure 5.9, $R_{\rm x}$ in (5.4) is virtually constant because we are in the free-flow regime. Thus, σ is essentially a normalised $R_{\rm y}^{\rm diff}$.

In the left plot in figure 5.9 the constant longitudinal force $F_{\rm x}^{\rm L} = 1f_0$ results in a velocity of $v_{\rm x} \approx 1$ simulation unit, and the transverse force $F_{\rm y}^{\rm L}{=}0.00225f_0$ is chosen to be slightly smaller than the critical transverse force at $T = 0$ for these simulations. The plot shows that for very small temperatures $\sigma \approx 0$. This means that an increase in the transverse force does not result in an increase in transverse motion, and at this temperature the apparent critical transverse force is larger than the applied transverse force $F_{\rm y}^{\rm L}{=}0.00225f_0$.

With increasing temperature, σ shows a significant peak. Here, an increase in the transverse force results in a strong increase in the transverse velocity, and this is where the system starts quickly moving transversely, and the applied transverse force is greater than the apparent critical transverse force.

For a further increase in temperature, σ comes down to $\sigma \approx 1.2$, before it drops

to 1.0 at the melting temperature T_m. The reason for $\sigma \approx 1.2$ for intermediate temperatures is that even after transverse depinning, the moving system feels some transverse pinning up to transverse forces many times larger than the critical transverse force: *Olson and Reichhardt* (2000) have shown that the transversely depinned system moves in an oscillating pattern: when the vortices have moved one lattice spacing in the transverse direction, they are pinned again for a short time, or at least slowed down. On average, the vortices move slower because of this repeated interruption of their transverse motion.

This remaining transverse pinning reduces with increasing transverse drive, $F_{\mathrm{y}}^{\mathrm{L}}$, and therefore v_{y} increases stronger than linearly with $F_{\mathrm{y}}^{\mathrm{L}}$, and $\sigma = (\mathrm{d}v_{\mathrm{y}}/\mathrm{d}F_{\mathrm{y}}^{\mathrm{L}})/R_{\mathrm{x}} \approx 1.2 > 1$.

The right plot in figure 5.9 shows zero temperature data for various longitudinal driving forces $F_{\mathrm{x}}^{\mathrm{L}}$ and two different constant transverse forces $F_{\mathrm{y}}^{\mathrm{L}} = 0.00225 f_0$ and $F_{\mathrm{y}}^{\mathrm{L}} = 0.00275 f_0$. For small $F_{\mathrm{x}}^{\mathrm{L}}$ the system does not move transversely and $\sigma = 0$. When $F_{\mathrm{x}}^{\mathrm{L}}$ increases, it increases the velocity, v_{x}, of the system and thus reduces the critical transverse force (as shown in figure 5.7). Therefore, for sufficiently large $F_{\mathrm{x}}^{\mathrm{L}}$ the system starts moving transversely and σ shows a peak which decays to 1.0 for larger $F_{\mathrm{x}}^{\mathrm{L}}$. The slow decay of σ is due to remaining transverse pinning above the transverse depinning force (*Olson and Reichhardt*, 2000). The magnitude of the constant transverse driving force $F_{\mathrm{y}}^{\mathrm{L}}$ determines the position of the peak of σ, as the two curves in the right plot in figure 5.9 demonstrate. In experimental work, the presence of a critical transverse force should manifest itself in σ changing as shown in figure 5.9 on the page before.

5.5 Conclusions

We have investigated numerically the critical transverse force of two-dimensional vortex systems in the presence of a random pinning potential. We find a critical transverse force for both the moving Bragg glass and the moving transverse glass, but not for turbulent plastic flow. We study in more detail the weak pinning limit in which only the moving Bragg glass with coupled vortex channels can be found.

The ratio of the critical transverse force to the static depinning force depends on the random pinning and can be as large as of the order of 10% at zero temperature for a smoothly varying pinning potential. For individual stronger point-like pins, this ratio is smaller.

We have performed a finite size study including up to 3000 vortices which reveals that the critical transverse force is overestimated for systems with less than 1000

vortices, but remains constant for larger systems. This is in contrast to an earlier study where the cut-off distance was not increased with system size but kept at a constant value, and where no size-dependence of the critical transverse force was observed (*Olson and Reichhardt*, 2000).

We find that the critical transverse force increases with increasing pinning strength up to a value at which the elastic motion changes to turbulent plastic flow and the critical transverse force goes rapidly to zero. By comparing these data with other observables, we conclude that the critical transverse force is indeed an order parameter of the moving glass, as predicted in *Le Doussal and Giamarchi* (1998).

The critical transverse force is inversely proportional to the longitudinal velocity and is compatible with recent predictions (*Le Doussal and Giamarchi*, 1998). At finite temperatures, the apparent critical transverse force decays with increasing temperature and vanishes at the melting temperature of the system. Our results suggest that in an experimental search for the critical transverse current, low temperatures and small longitudinal driving forces (which, however, will have to be large enough to cause elastic motion) should be used.

We suggest measuring the differential transverse resistance normalised by the longitudinal resistance to decide whether transverse barriers are observed in experiments. We have simulated such an experiment and provide the dependence of this observable on temperature and on the longitudinal driving force, which can be compared directly with experimental results.

Chapter 6

Three-dimensional studies: The electromagnetically interacting pancake system

Preface

The work presented in this chapter started as a collaboration with Matthew J. W. Dodgson. We later realised that Alexei E. Koshelev was working on a similar model, and started to collaborate (*Fangohr, Koshelev and Dodgson*, 2002).

6.1 Introduction

In chapter 5 we have investigated the behaviour of two-dimensional vortex systems. In this chapter we extend our model, and investigate the three-dimensional case in the absence of pinning (with the exception of section 6.4.9 where we introduce random pinning).

Vortex lines within the layered high-temperature materials, such as BSCCO and YBCO, can be understood as (wiggling) stacks of pancake vortices (*Artemenko and Kruglov*, 1990, *Feigel'man et al.*, 1990, *Buzdin and Feinberg*, 1990, *Clem*, 1991, *Blatter et al.*, 1994). The pancakes are located in the superconducting layers and interact with each other via two mechanisms: (i) electromagnetic interaction and (ii) Josephson coupling. The electromagnetic interaction is due to interaction of supercurrents circulating around each pancake, whereas the Josephson coupling results from a phase shift of the superconducting wave function between the layers.

To be able to understand the phase diagram of high temperature superconductors, we need to gain an insight into the behaviour of this vortex matter under a variety of experimental conditions. In moderately anisotropic materials, such as

YBCO, the short-range Josephson coupling is the dominating inter-layer interaction, and the vortices can be described as elastic strings or as pancakes coupled between neighbouring layers (*Ryu et al.*, 1992, *Ryu and Stroud*, 1996, *Nordborg and Blatter*, 1997, *Wilkin and Jensen*, 1997b,a, *Nordborg and Blatter*, 1998, *van Otterlo et al.*, 1998, *Olson et al.*, 2000b). In very anisotropic materials on the other hand, such as BSCCO, the Josephson coupling is weak, and the long-range electromagnetic interaction between the pancakes has to be taken into account.

As a first step, we consider very anisotropic materials in the absence of Josephson coupling, and neglect pinning. The electromagnetic coupling alone is a complicated problem and the phase diagram of the system cannot be computed solely by analytical methods.

The challenge for a numerical investigation is that the interlayer interaction between pancakes extends over a range of $2\lambda/s \sim 100 - 150$ layers, where λ is the London penetration depth and s the layer spacing.

In principle, one can stack a set two-dimensional pancake systems on top of each other, and introduce additional interlayer interactions. Several groups have modelled the three-dimensional vortex state in this way (*Kolton et al.*, 2000a,b, *Olson and Grønbech-Jensen*, 2000, *Olson et al.*, 2000a, 2001) in the limit of zero Josephson coupling, in order to study the dynamics of such a system in the presence of pinning. However, because every pancake in one layer interacts with all other pancakes in its own layer and all pancakes in all other layers, these numerical investigations have been performed on small systems using about 10 layers and of the order of 100 vortices per layer.

With today's computational resources it is not feasible to fully compute such a system because the necessary computational effort grows quadratically with the number of layers.

Dodgson, Koshelev, Geshkenbein and Blatter (2000b) showed that the problem of the long-range electromagnetic interactions between the layers can be overcome by exploiting it and by applying a mean-field approach in the c-direction (perpendicular to the layers). One averages the pancake positions over all layers, and computes a "substrate" potential which pancakes in each layer feel as the cumulative effect from attraction of pancakes in all other layers (see figure 6.1 on the following page). Pancakes within one layer interact directly with each other, whereas the interaction with pancakes in other layers is mediated via the substrate potential. Thus, each layer is treated individually, until a new substrate potential can be computed. This process is iterated, until the substrate has converged to a steady solution.

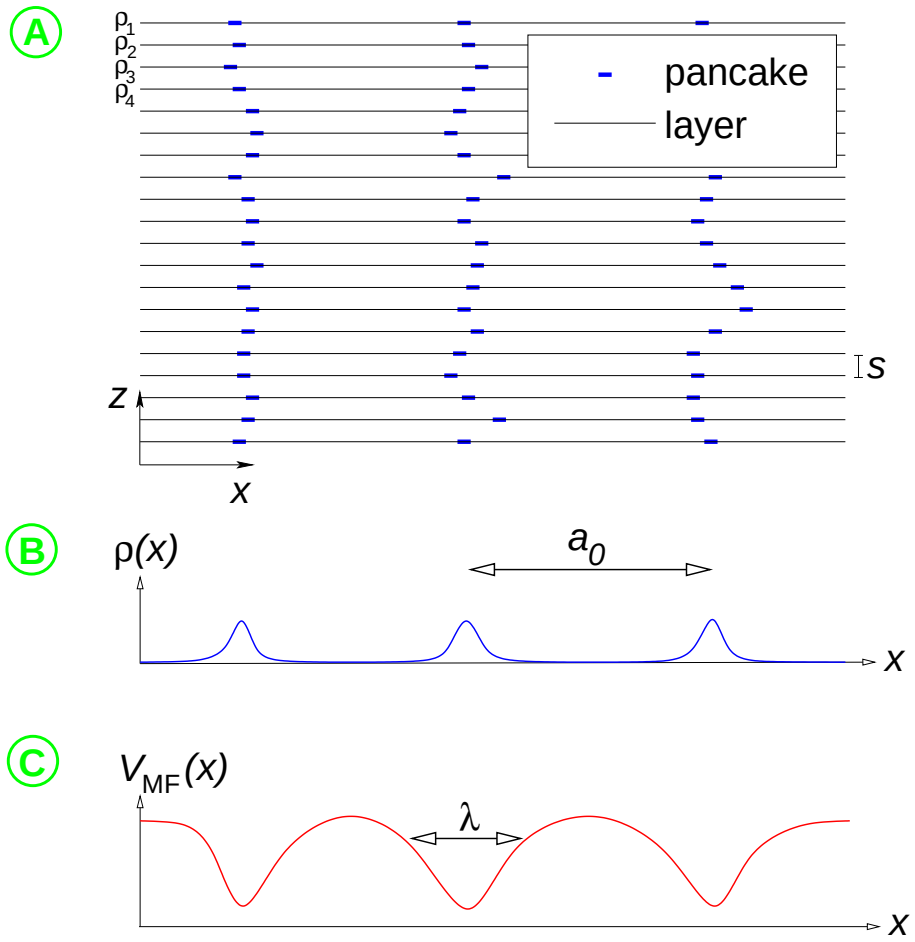

Figure 6.1: Schematic representation of the substrate model for a system with one-dimensional layers. *(A)* The pancake positions, $\rho_n(x)$, in each layer n, are *(B)* averaged over the layers in order to obtain the averaged pancake density, $\rho(x)$. From the average pancake density, $\rho(x)$, we compute *(C)* the substrate potential, $V_{\mathrm{MF}}(x)$, which is smeared over a length of the order of λ. The vortex lattice spacing is a_0 and s is the layer spacing.

In this chapter, we present the first numerical implementations of this substrate model and show results which we compare with the semi-analytic approximations given by *Dodgson et al.* (2000b).

We express magnetic induction in units of $B_\lambda \equiv \Phi_0/\lambda^2$, where Φ_0 is the magnetic flux quantum and λ is the penetration depth, such that the average pancake-spacing in a hexagonal lattice is $a_0 = \sqrt{\frac{2}{\sqrt{3}}}\lambda \approx 1.07\lambda$ at $B = B_\lambda$. Temperature T is expressed in reduced units t as a multiple of the pre-factor $2\epsilon_0 s$ of the logarithmic pancake-pancake interaction

$$t \equiv \frac{1}{\Gamma} \equiv \frac{k_{\mathrm{B}}T}{2\epsilon_0 s}, \tag{6.1}$$

where $\epsilon_0 = \Phi_0^2/(4\pi\mu_0\lambda^2)$, μ_0 is the vacuum permeability, and s is the layer spacing. This allows to compare our results with outcomes from two-dimensional one-component Coulomb plasma simulations (*de Leeuw and Perram*, 1982, *Caillol et al.*,

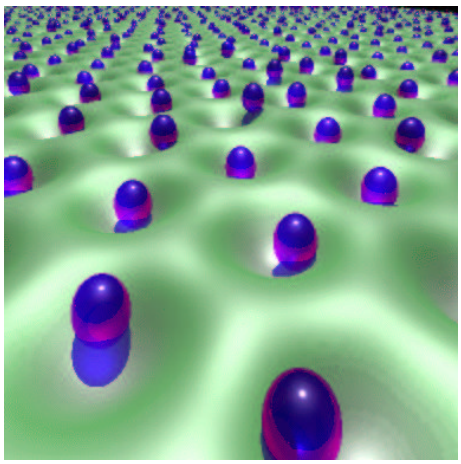

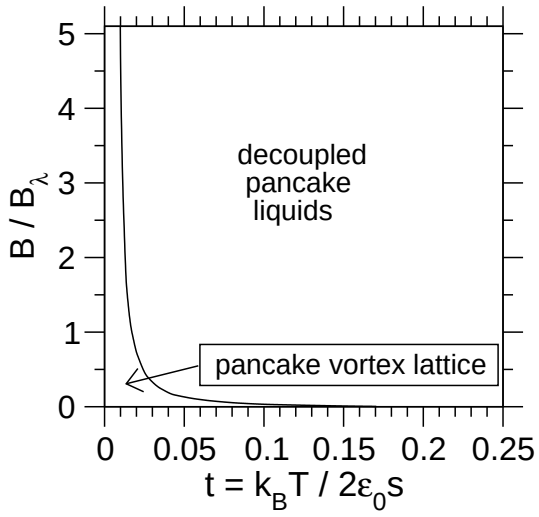

Figure 6.2: *Left:* Snapshot of the pancakes (visualised by spheres) placed onto the substrate potential (visualised as a surface) at $B = B_\lambda$ and $t = 1/59 \approx 0.017$ just below the melting transition, demonstrating how the substrate potential constrains the pancakes' motion. *Right:* The phase diagram computed using the substrate method. The transition line divides the system into a three-dimensional pancake lattice below the line and decoupled two-dimensional pancake liquids above the line.

1982, *Choquard*, 1983), where frequently $\Gamma = 1/t$ is used to express temperatures.

We summarise this chapter in figure 6.2. On the left plot the central idea is visualised: pancakes experience attractive inter-layer interactions through the substrate potential which stabilises the pancake crystal. On the right we show the computed phase diagram for the layered pancake system. At low fields B, the electromagnetic attraction of range $\lambda \gg s$ between pancakes in different layers stabilises the three-dimensional pancake vortex lattice. Increasing the magnetic field decreases the relative strength of the inter-layer coupling. At high fields, $B \gg B_\lambda$, the long-range repulsive interaction within the layer dominates, and the three-dimensional pancake lattice melts into decoupled two-dimensional liquids.

6.2 Mean field approach (Substrate model)

6.2.1 The mean-field inter-layer coupling

The in-layer energy $\mathcal{E}^{\rm in}$ and the inter-layer energy $\mathcal{E}^{\rm inter}$ of a system of electromagnetically interacting pancakes in a layered superconductor is, respectively,

$$\mathcal{E}^{\rm in} = \sum_n E_n^{\rm in} = \sum_n \frac{1}{2} \sum_j \sum_{j' \neq j} U(\mathbf{R}_j^n - \mathbf{R}_{j'}^n, 0) \tag{6.2}$$

and

$$\mathcal{E}^{\rm inter} = \sum_n E_n^{\rm inter} = \sum_n \frac{1}{2} \sum_{n' \neq n} \sum_j \sum_{j'} U(\mathbf{R}_j^n - \mathbf{R}_{j'}^{n'}, n - n'). \tag{6.3}$$

Indices n and n' count over layers, and j and j' over pancakes in the layers, $\mathbf{R}_j^n$ is the (two-dimensional) position of pancake j in layer n, and $U(\mathbf{R}, n)$ is the coupling energy for two pancakes separated by a vector $(\mathbf{R}, z)$, where $z = ns$, with s being the layer spacing. The z-axis is chosen perpendicular to the layers.

The in-layer pancake interaction is (*Clem*, 1991)

$$U(\mathbf{r}, 0) = 2\epsilon_0 s \left(\left(1 - \frac{s}{2\lambda} \right) \ln \left(\frac{L}{r} \right) + \frac{s}{2\lambda} \int_r^\infty {\rm d}r' \frac{\exp(-r'/\lambda)}{r'} \right) \tag{6.4}$$

and the inter-layer interaction ($n \neq 0$) is

$$U(\mathbf{r}, n) = -\frac{\epsilon_0 s^2}{\lambda} \left(\exp\left(-\frac{ns}{\lambda} \right) \ln \left(\frac{L}{r} \right) - \int_r^\infty {\rm d}r' \, \frac{\exp(-\sqrt{r'^2 + (ns)^2}/\lambda)}{r'} \right), \tag{6.5}$$

where L is the size of the system. Using

$$\rho_n(\mathbf{r}) = \sum_j \delta(\mathbf{r} - \mathbf{R}_j^n) \tag{6.6}$$

we rewrite

$$\mathcal{E}^{\rm inter} = \frac{1}{2} \sum_n \sum_{n' \neq n} \int {\rm d}^2 r \, {\rm d}^2 r' \, \rho_n(\mathbf{r}) \rho_{n'}(\mathbf{r}') U(\mathbf{r} - \mathbf{r}', n - n'). \tag{6.7}$$

We separate pancake density fluctuations from the layer-average density

$$\rho(\mathbf{r}) \equiv \langle \rho_n(\mathbf{r}) \rangle, \tag{6.8}$$

$$\rho_n(\mathbf{r}) = \rho(\mathbf{r}) + \delta\rho_n(\mathbf{r}), \tag{6.9}$$

and obtain from (6.7)

$$\begin{aligned} \mathcal{E}^{\rm inter} = & \frac{1}{2} \sum_n \sum_{n' \neq n} \int {\rm d}^2 r {\rm d}^2 r' U(\mathbf{r} - \mathbf{r}', n - n') \\ & \times \left[\rho(\mathbf{r}) \rho(\mathbf{r}') + 2\rho(\mathbf{r}') \delta\rho_n(\mathbf{r}) + \delta\rho_n(\mathbf{r}) \delta\rho_{n'}(\mathbf{r}') \right], \end{aligned} \tag{6.10}$$

where we have used

$$\sum_n \sum_{n' \neq n} \int \mathrm{d}^2 r \mathrm{d}^2 r' U(\mathbf{r} - \mathbf{r}', n - n') \rho(\mathbf{r}') \delta\rho_n(\mathbf{r}) \tag{6.11}$$

$$= \sum_n \sum_{n' \neq n} \int \mathrm{d}^2 r \mathrm{d}^2 r' U(\mathbf{r} - \mathbf{r}', n - n') \rho(\mathbf{r}) \delta\rho_{n'}(\mathbf{r}'). \tag{6.12}$$

In the mean field approach we neglect the last term in (6.10), and obtain the mean field interlayer energy $\mathcal{E}^{\mathrm{MF}}$ from (6.10)

$$\mathcal{E}^{\mathrm{MF}} = \sum_n E_n^{\mathrm{MF}} \tag{6.13}$$

$$= \sum_n \frac{1}{2} \sum_{n' \neq n} \int \mathrm{d}^2 r \mathrm{d}^2 r' U(\mathbf{r} - \mathbf{r}', n - n') \left[\rho(\mathbf{r}) \rho(\mathbf{r}') + 2\rho(\mathbf{r}') \delta\rho_n(\mathbf{r}) \right]$$

$$= \frac{1}{2} \sum_n \int \mathrm{d}^2 r \, V_{\mathrm{MF}}(\mathbf{r}) \rho(\mathbf{r}) + \sum_n \int \mathrm{d}^2 r \, V_{\mathrm{MF}}(\mathbf{r}) \delta\rho_n(\mathbf{r}) \tag{6.14}$$

$$\overset{(6.9)}{=} -\frac{1}{2} \sum_n \int \mathrm{d}^2 r \, V_{\mathrm{MF}}(\mathbf{r}) \rho(\mathbf{r}) + \sum_n \int \mathrm{d}^2 r \, V_{\mathrm{MF}}(\mathbf{r}) \rho_n(\mathbf{r}). \tag{6.15}$$

The last term in (6.15) describes fluctuations in the fixed substrate potential V_{MF},

$$V_{\mathrm{MF}}(\mathbf{r}) = \int \mathrm{d}^2 r' \left[\sum_{n \neq 0} U(\mathbf{r} - \mathbf{r}', n) \right] \rho(\mathbf{r}') \tag{6.16}$$

$$= \int \mathrm{d}^2 r' \mathcal{U}(\mathbf{r} - \mathbf{r}') \rho(\mathbf{r}') \tag{6.17}$$

$$\equiv (\mathcal{U} * \rho)(\mathbf{r}) \tag{6.18}$$

with

$$\mathcal{U}(\mathbf{r}) \equiv \sum_{n \neq 0} U(\mathbf{r}, n). \tag{6.19}$$

$\mathcal{U}(\mathbf{r})$ is the interaction potential of a pancake separated by $\mathbf{r}$ from a stack of pancakes minus the interaction of the (missing) pancake in the same layer. We show in appendix B that

$$\mathcal{U}(\mathbf{r}) = 2\epsilon_0 s K_0 \left(\frac{r}{\lambda} \right) - U(\mathbf{r}, 0), \tag{6.20}$$

with K_0 being a modified Bessel function of the second kind. Ignoring terms of the order of $s/2\lambda$, the pancake-pancake repulsion (6.4) simplifies to

$$U(\mathbf{r}, 0) = 2\epsilon_0 s \ln \left(\frac{L}{r} \right). \tag{6.21}$$

6.2.2 Algorithm

1. Assume initial pancake densities $\rho_n(\mathbf{r})$, for example a hexagonal lattice in each layer n.
2. Average the pancake density $\rho_n(\mathbf{r})$ over all layers to obtain $\rho(\mathbf{r})$, (6.8).
3. Compute the substrate potential $V_{\mathrm{MF}}(\mathbf{r})$, (6.18) by convoluting the substrate interaction kernel $\mathcal{U}(\mathbf{r})$, (6.20), with the average pancake density $\rho(\mathbf{r})$

$$V_{\mathrm{MF}}(\mathbf{r}) = (\mathcal{U} * \rho)(\mathbf{r}). \tag{6.22}$$

4. For each layer n compute the pancake distribution $\rho_n(\mathbf{r})$ using Langevin dynamics simulations. The total energy for layer n contains the direct pancake-pancake interaction within the layer (6.2)

$$E_n^{\mathrm{in}} = \frac{1}{2}\sum_j \sum_{j' \neq j} U(\mathbf{R}_j^n - \mathbf{R}_{j'}^n, 0), \tag{6.23}$$

and the relevant interaction with pancakes in other layers via the substrate potential (6.15)

$$\begin{aligned} E_n^{\mathrm{MF}} &\overset{(6.15)}{=} \underbrace{-\frac{1}{2}\int \mathrm{d}^2 r\, V_{\mathrm{MF}}(\mathbf{r})\rho(\mathbf{r})}_{E^{\mathrm{coup}}} + \int \mathrm{d}^2 r\, V_{\mathrm{MF}}(\mathbf{r})\rho_n(\mathbf{r}) \\ &\overset{(6.6)}{=} -E^{\mathrm{coup}} + \sum_j V_{\mathrm{MF}}(\mathbf{R}_j^n), \end{aligned} \tag{6.24}$$

E^{coup} is constant for a given $\rho(\mathbf{r})$ and can therefore be ignored within the Langevin dynamics simulation as it only shifts the energy scale.

5. Go to 2, until V_{MF} (or ρ) has converged.

Since the substrate potential V_{MF} in equation (6.24) in step 4 is the same for all layers, we can compute $\rho_n(\mathbf{r})$ for many Langevin-dynamics time-steps rather than for many layers. Therefore, in order to obtain the averaged pancake density $\rho(\mathbf{r})$ in step 2, we average over time-steps computed in one layer rather than averaging over layers.

Using the substrate potential, we reduce the solution of the three-dimensional problem to performing one two-dimensional simulation in the presence of the iteratively refined substrate potential. However, employing this mean field approach, we lose the ability to compute spatial correlations in the c-direction perpendicular to the layers.

6.3 Numerical implementation

6.3.1 Computation of the substrate potential

We have already developed a simulation of the two-dimensional vortex state (chapter 3), and have to extend it to contain the substrate potential. The substrate can be seen as an additional pinning potential (which, however, stabilises the hexagonal vortex system). We are left with the challenge of computing the substrate potential (6.17)

$$\begin{aligned} V_{\mathrm{MF}}(\mathbf{r}) &= (\mathcal{U} * \rho)(\mathbf{r}) && (6.25)\\ &= \int \mathrm{d}^2 r'\, \mathcal{U}(\mathbf{r}-\mathbf{r}')\rho(\mathbf{r}') && (6.26)\\ &\overset{(6.20),(6.21)}{=} \int \mathrm{d}^2 r'\, 2\epsilon_0 s \left[K_0\left(\frac{|\mathbf{r}-\mathbf{r}'|}{\lambda}\right) + \ln\left(\frac{|\mathbf{r}-\mathbf{r}'|}{L}\right)\right] \rho(\mathbf{r}'). && (6.27) \end{aligned}$$

To compute this, we need a pancake density $\rho(\mathbf{r})$, which we can obtain by creating a two-dimensional histogram of pancake positions. The histogram allows us to compute $\rho(\mathbf{r})$ at discrete positions

$$\mathbf{r}_{ij} = i\boldsymbol{\Delta}\mathbf{x} + j\boldsymbol{\Delta}\mathbf{y}, \tag{6.28}$$

where $i \in [-N_x/2, N_x/2-1]$ and $j \in [-N_y/2, N_y/2-1]$. N_x is the even number of points in the x-direction in the histogram, and N_y is defined accordingly for the y-direction. The kernel (6.20) for the convolution is derived analytically, and can thus be evaluated for all required $\mathbf{r}_{ij}$. We can then compute (6.26) numerically

$$\begin{aligned} V_{\mathrm{MF}}(\mathbf{r}) &= \int \mathrm{d}^2 r'\, \mathcal{U}(\mathbf{r}-\mathbf{r}')\rho(\mathbf{r}') \\ &\approx \sum_i \sum_j \Delta x \Delta y\, \mathcal{U}(\mathbf{r}-\mathbf{r}'_{ij})\rho(\mathbf{r}'_{ij}) && (6.29) \end{aligned}$$

and thus evaluate $V_{\mathrm{MF}}(\mathbf{r})$ at positions $\mathbf{r}_{ij}$ for a look-up table.
There are two problems with equation (6.29):

1. The convolution requires a large number of operations. To evaluate $V_{\mathrm{MF}}(\mathbf{r})$ for one $\mathbf{r}$ using (6.29), requires of the order of $N_x N_y$ operations. Thus, the total effort to compute V_{MF} for all $\mathbf{r}_{ij}$ scales as $\mathcal{O}(N_x^2 N_y^2)$ (assuming we evaluate V_{MF} on the mesh given by the $\mathbf{r}_{ij}$). For $N_x = N_y = 1000$, this is a number of operations of the order of 10^{12}, which takes about a day to compute on a modern workstation.

2. The kernel shows a spherical symmetry, *i.e.* $\mathcal{U}(\mathbf{r}) = \mathcal{U}(r)$, and the data $\rho(\mathbf{r})$ are periodic. To preserve the spherical symmetry, a cut-off for the kernel would have to be introduced at a distance of the length of half the simulation cell. (Otherwise the rectangular symmetry of the simulation cell would be visible artificially in the convolution). Since we want to compare runs at different field strengths, the size of the simulation cell changes with the magnetic field, and thus the cut-off would have to change. A changing cut-off would prevent the comparison of results at different field strengths.

Both problems can be overcome by performing the convolution (6.25) in Fourier-space and exploiting the convolution theorem.

We define the forward Fourier transform operator $\mathcal{F}$, and use the short-hand notation $\hat{f}(q)$ for a Fourier-transformed function $f(x)$, with $i = \sqrt{-1}$

$$\hat{f}(q) = \mathcal{F}\{f(x)\} = \int_{-\infty}^{\infty} \mathrm{d}x \quad f(x) \exp(-iqx) \tag{6.30}$$

and the inverse Fourier transform

$$f(x) = \mathcal{F}^{-1}\{\mathcal{F}\{f(x)\}\} = \int_{-\infty}^{\infty} \frac{\mathrm{d}q}{2\pi} \quad \mathcal{F}\{f(x)\} \exp(iqx). \tag{6.31}$$

The convolution theorem reads

$$\mathcal{F}\{(a * b)(x)\} = \mathcal{F}\{a(x)\}\mathcal{F}\{b(x)\} \quad \Longleftrightarrow \quad \widehat{(a * b)}(q) = \hat{a}(q)\hat{b}(q) \tag{6.32}$$

We label the discrete Fourier transform operator with a subscript D to distinguish it from the analytical transform, and make use of (6.32) by re-writing (6.25) as

$$V_{\mathrm{MF}}(\mathbf{r}) = \mathcal{F}_{\mathrm{D}}^{-1} \left\{ \mathcal{F}_{\mathrm{D}}\{\rho(\mathbf{r})\} \mathcal{F}_{\mathrm{D}}\{\mathcal{U}(\mathbf{r}\} \right\}. \tag{6.33}$$

This solves problem 1, as the computational effort for a discrete (fast) Fourier transform is $\mathcal{O}(N \ln(N))$ where $N = N_x N_y$ is the total number of points in the matrix.

Problem 2 can be solved by using the *analytical* Fourier transform $\hat{\mathcal{U}}(\mathbf{q})$ of the kernel in (6.33):

$$\begin{aligned}\hat{\mathcal{U}}(\mathbf{q}) = \mathcal{F}\{\mathcal{U}(\mathbf{r})\} &= \mathcal{F}\{K_0(\mathbf{r})\} - \mathcal{F}\{\mathbf{r}\} \\ &= 4\pi\epsilon_0 s \frac{1}{\lambda^{-2} + q^2} - 4\pi\epsilon_0 s \frac{1}{q^2} \\ &= -4\pi\epsilon_0 s \frac{\lambda^{-2}}{q^2(q^2 + \lambda^{-2})} \end{aligned} \tag{6.34}$$

Eventually, we compute

$$V_{\mathrm{MF}}(\mathbf{r}) = \mathcal{F}_{\mathrm{D}}^{-1}\big\{ \underbrace{\mathcal{F}_{\mathrm{D}}\{\rho(\mathbf{r})\}}_{\rho(\mathbf{q})} \hat{\mathcal{U}}(\mathbf{q}) \big\} \tag{6.35}$$

$$= \int \frac{\mathrm{d}^2 q}{(2\pi)^2}\, \hat{\mathcal{U}}(\mathbf{q}) \rho(\mathbf{q}) \exp(i\mathbf{q}\cdot\mathbf{r}) \tag{6.36}$$

which is fast and overcomes the need for a cut-off. We have introduced the abbreviation $\rho(\mathbf{q}) = \mathcal{F}_{\mathrm{D}}\{\rho(\mathbf{r})\}$ to keep the notation efficient. Appendix C contains more technical information on performing the discrete Fourier transforms (6.35) numerically. Equation (6.34) diverges for $q \to 0$ but we can set $\hat{\mathcal{U}}(0)$ arbitrarily, for example $\hat{\mathcal{U}}(0) = 0$, as this fixes only the absolute value of the energy V_{MF}.

We have used three different methods for computing $V_{\mathrm{MF}}(\mathbf{r})$ numerically.

6.3.2 The full method

The "full method" computes the substrate potential V_{MF} using the full spectrum $\rho(\mathbf{q})$ of Fourier-components of the average pancake density $\rho(\mathbf{r})$ as shown in (6.36). In our simulations we use a resolution of roughly 100^2 grid-cells per pancake in order to compute $\rho(\mathbf{r})$ as an average over time-steps. This results in reciprocal lattice vectors up to magnitudes of about $100Q_0$, where $Q_0 = 4\pi/(\sqrt{3}a_0)$, because $|\mathbf{Q}_{\max}|/Q_0 \approx 2\pi/(\Delta x Q_0) \approx a0/\Delta x \approx 100$. The necessary discrete Fourier-transform of $\rho(\mathbf{r})$, and the inverse transform of $V_{\mathrm{MF}}(\mathbf{q}) = \hat{\mathcal{U}}(\mathbf{q})\rho(\mathbf{q})$ can be done efficiently using an implementation of the Fast Fourier Transform (*Frigo and Johnson*, 1998).

We pre-compute the substrate potential $V_{\mathrm{MF}}(\mathbf{r})$ on a mesh and interpolate subsequently for intermediate pancake positions while performing Langevin-dynamics time-steps in the fixed substrate. We compute a new substrate every 200,000 time-steps. It is important to average over so many time-steps to reduce density fluctuations (due to poor statistics) in the pancake histogram, which would result in a deformed substrate potential.

Note that $\rho(\mathbf{r})$ and $\rho(\mathbf{q})$ are discretised out of numerical necessity to compute a histogram but not for conceptual reasons.

6.3.3 The Fourier-filtered method

The average density $\rho(\mathbf{r})$ must be a periodic function if we are in the solid phase, and can be represented by a discrete set of Fourier components. Therefore, the second method uses only a subset $\mathbf{Q}_\mu \subset \mathbf{q}$ of the Fourier components $\mathbf{q}$ to represent $\rho(\mathbf{q})$:

$$\rho^{\mathrm{FF}}(\mathbf{q}) = \sum_\mu \rho_{\mathbf{Q}_\mu} \delta^2(\mathbf{q} - \mathbf{Q}_\mu) \tag{6.37}$$

where the $\mathbf{Q}_\mu$-vectors are the reciprocal lattice vectors which we determine from the maxima of the structure factor, and

$$\rho_{\mathbf{Q}} =< \frac{(2\pi)^2}{L_x L_y} \sum_j \exp(-i\mathbf{R}_j^c \cdot \mathbf{Q}) >_c \tag{6.38}$$

with $L_x L_y$ being the area of the simulation cell. We average over a set of configurations c of pancake positions $\mathbf{R}_j^c$ (*i.e.* time-steps) to compute $\rho_{\mathbf{Q}}$.

Using

$$\rho^{\mathrm{FF}}(\mathbf{r}) = \int \frac{\mathrm{d}^2 q}{(2\pi)^2}\ \rho^{\mathrm{FF}}(\mathbf{q}) \exp(i\mathbf{q}\cdot\mathbf{r})$$

to present $\rho(\mathbf{r})$, we Fourier-filter $\rho(\mathbf{r})$, and keep only the relevant components for the computation of the periodic substrate. We can write

$$V_{\mathrm{MF}}^{\mathrm{FF}}(\mathbf{r}) \overset{(6.36)}{=} \int \frac{\mathrm{d}^2 q}{(2\pi)^2}\ \hat{\mathcal{U}}(\mathbf{q}) \rho^{\mathrm{FF}}(\mathbf{q}) \exp(i\mathbf{q}\cdot\mathbf{r}) \tag{6.39}$$

$$\overset{(6.37)}{=} \frac{1}{(2\pi)^2} \sum_\mu \hat{\mathcal{U}}(\mathbf{Q}_\mu) \rho_{\mathbf{Q}_\mu} \exp(i\mathbf{Q}_\mu \cdot \mathbf{r}) \tag{6.40}$$

$$\overset{(6.34)}{=} \frac{-4\pi\epsilon_0 s}{(2\pi)^2} \sum_\mu \frac{\lambda^{-2} \rho_{\mathbf{Q}_\mu} \exp(i\mathbf{Q}_\mu \cdot \mathbf{r})}{Q_\mu^2(\lambda^{-2} + Q_\mu^2)}. \tag{6.41}$$

This is equivalent to using the full-method, but setting $\rho(\mathbf{q}) = 0$ if $\mathbf{q} \notin \{\mathbf{Q}_\mu\}$.

The advantage of the Fourier-filtered method is that we need to average over less iterations before we can compute a new pancake density, and subsequently a new substrate, because the substrate is per construction periodic. Using the Fourier-filtered method we use 500 time-steps for each substrate iteration.

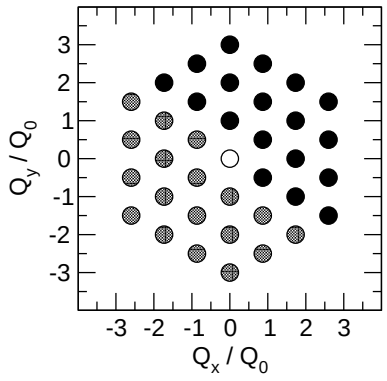

Figure 6.3: Set of $\mathbf{Q}_\mu$-vectors up to third order (*i.e.* three "shells" around the origin) in reciprocal space used in the reduced-Q Fourier-filtered method to compute (6.41). Due to the reality of $\rho(\mathbf{r})$ we have $\rho(\mathbf{q}) = \bar{\rho}(-\mathbf{q})$ and it is therefore sufficient to compute only half of the 36 terms containing $\rho_{\mathbf{Q}_\mu}$ in (6.41).

It turns out that it is not necessary to take the average (6.38) over different configurations but it is sufficient to use just one configuration (*i.e.* one time-step):

$$\rho_{\mathbf{Q}} = \frac{(2\pi)^2}{L_x L_y} \sum_j \exp(-i\mathbf{R}_j \cdot \mathbf{Q}). \tag{6.42}$$

Nevertheless, we run a simulation for 500 time-steps with the same fixed substrate potential to reduce re-computation of $\rho_{\mathbf{Q}}$, and to give the pancakes some time to explore the system with a new substrate potential.

6.3.4 The reduced-Q (Fourier-filtered) method

In addition to Fourier-filtering $\rho(\mathbf{r})$ we can speed up the computation further because close to the melting temperature, $\rho_{\mathbf{Q}_\mu}$ decays quickly for higher-order $\mathbf{Q}_\mu$ due to the Debye-Waller factor. We can estimate the reduction of $\rho_{\mathbf{Q}}$ due to the Debye-Waller factor

$$\exp\left(-\frac{<u^2>Q^2}{4}\right) = \exp\left(-\frac{1}{4}\frac{<u^2>}{a_0^2}\frac{16\pi^2 Q^2}{Q_0^2}\right) \tag{6.43}$$

with $Q_0 = 4\pi/(\sqrt{3}a_0)$. Depending on $<u^2>$ we can ignore all $\rho(\mathbf{Q}_\mu)$ with $|\mathbf{Q}_\mu| > Q'$. For all but the smallest fields, we find that close to the melting transition $<u^2>/a_0^2 \approx 0.02 - 0.03$ (see inset of figure 6.14), and it is sufficient to include up to 3^{rd}-order vectors $\mathbf{Q}_\mu$ in the summation in (6.41) as shown in figure 6.3.

For the reduced-Q Fourier-filtered method it is more efficient to evaluate (6.41) for each pancake position occurring in the Langevin dynamics simulation rather than pre-computing V_{MF} on a mesh.

We demonstrate the equivalence of the full and the Fourier-filtered method for the determination of the instability line in section 6.4.1, and we compare with the reduced-Q Fourier-filtered method in section 6.4.5.

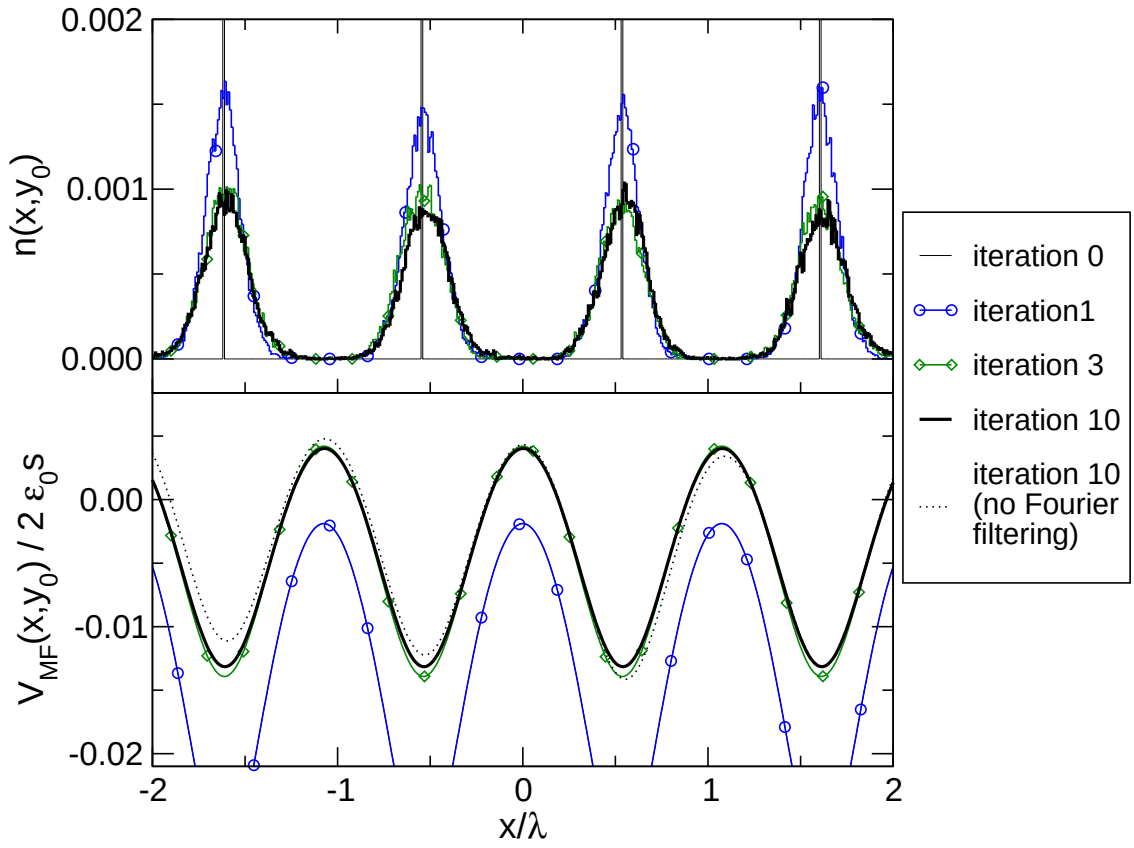

Figure 6.4: Convergence to pancake lattice at $B = B_\lambda$ and $t = 1/59 \approx 0.017$. *Top:* pancake histogram $n(x, y_0)$ taken along $y = y_0$. *Bottom:* substrate potential $V_{\mathrm{MF}}(x, y_0)$.

6.4 Results

6.4.1 Convergence

As described in section 6.2.2, we start each run with a hexagonal pancake distribution corresponding to zero temperature.

6.4.1.1 Convergence to solid state

Figure 6.4 shows results for the Fourier-filtered method at $B = B_\lambda$ and at a temperature $t = 1/59 \approx 0.017$. The top plot shows a one-dimensional slice of the two-dimensional pancake histogram $n(x, y_0)$ taken along x at $y = y_0$. The histogram relates to the pancake density via $n(x, y) = \rho(x, y)\Delta x \Delta y$ where Δx and Δy are the spacings of the grid used to create the histogram. For the 0^{th} substrate-iteration we set the histogram to have narrow and high peaks at the pancake equilibrium positions corresponding to delta-peaks in a zero-temperature pancake density $\rho(\mathbf{r})$. Based on this initial pancake distribution, we compute the substrate potential, $V_{\mathrm{MF}}(\mathbf{r})$, for the first substrate-iteration, of which a one-dimensional slice at $y = y_0$ is shown in the lower part of figure 6.4. Using this substrate potential,

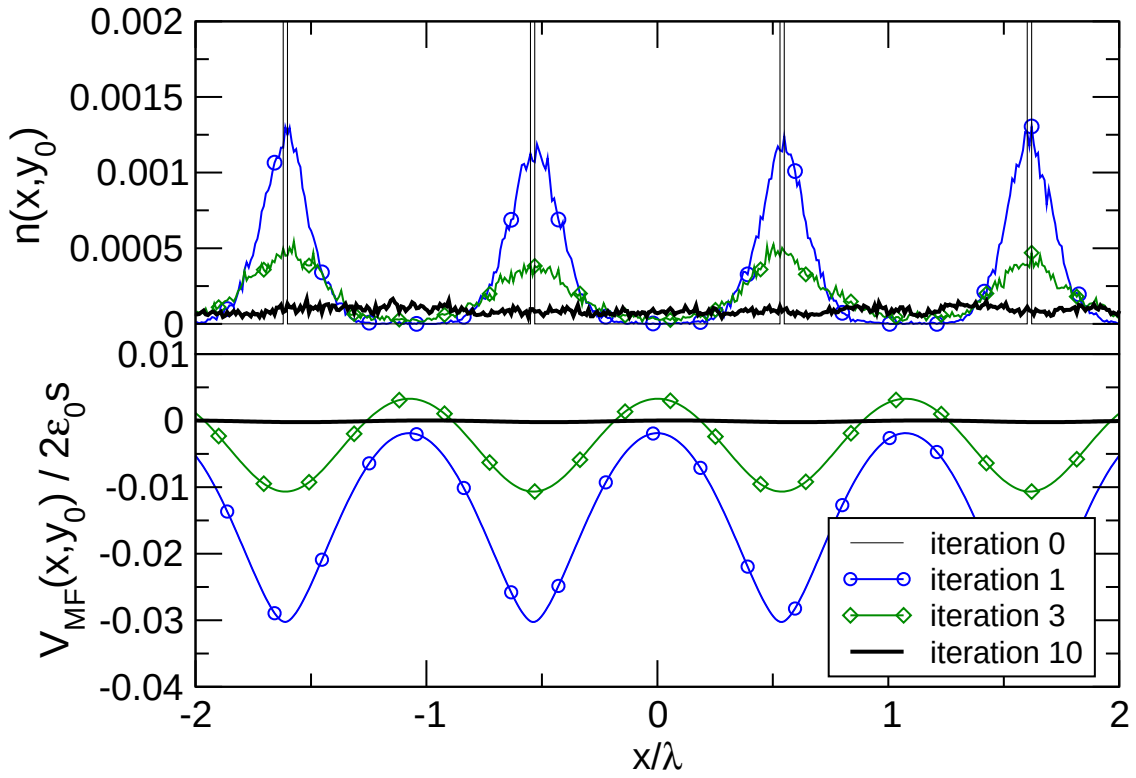

Figure 6.5: Convergence to pancake liquid. As figure 6.4 but at $t = 1/50 = 0.02$ above the melting temperature at $B = B_\lambda$.

we run the Langevin dynamics simulation for 200,000 steps which results in the histogram for iteration 1 as shown in the upper plot of figure 6.4. Based on these data, we compute the substrate potential for iteration 2. We iterate the substrate re-computation until the substrate potential has reached a steady state (typically after 10 substrate-iterations). The figure demonstrates that the system converges quickly to a pancake solid at this temperature below melting.

The dotted line in the lower part of figure 6.4 shows for comparison a substrate potential for iteration 10 computed using the full method. While the amplitude and width of the wells (and thus the resulting force) are virtually identical to the Fourier-filtered data, the magnitude of the substrate from the full method varies slightly. This is due to (long wavelength) density fluctuations in the histogram data and reduces further if one uses more time-steps for each substrate iteration.

6.4.1.2 Convergence to liquid state

Figure 6.5 shows data for $B = B_\lambda$ and a higher temperature $t = 1/50 = 0.02$ which is above the melting temperature. Here, the pancake distribution broadens and consequently the substrate potential flattens quickly within the first few substrate

iterations. Eventually, the system has become a disordered liquid with an approximately constant pancake density and the substrate is virtually flat, as shown for iteration 10. We conclude that for this temperature and magnetic field the pancake lattice is unstable with respect to melting into a pancake liquid.

Figure 6.6 on the next page shows the first four substrate-iterations for a system above the melting temperature using the full method. While using the Fourier-filtered method the substrate shows (per definition) a perfect periodicity (see figure 6.2 on page 87), the full method allows irregularities in the substrate potential. Also visible are the long-wavelength fluctuations of the substrate as mentioned in section 6.4.1.1.

For figure 6.4, 6.5 and 6.6 we have used 200,000 time-steps for each substrate-iteration in order to be able to compare the full and the Fourier-filtered method, but it would be sufficient to use far fewer time-steps per substrate-iteration for the Fourier-filtered methods. For production purposes, we use the reduced-Q Fourier-filtered method and update the substrate every 500 time-steps (section 6.3.3). Although more substrate-iterations than with the full method are required before the system reaches a steady state, the reduced-Q Fourier-filtered approach is more efficient. The full method and both Fourier-filtered methods find that at $B = B_\lambda$ the pancake lattice becomes unstable for $0.017 \leq t \leq 0.018$.

6.4.2 Comparison Monte-Carlo and Langevin dynamics

Recently, we learned that Alexei E. Koshelev (AEK) had started investigating the same system numerically. We decided to join forces and collaborate. AEK wrote a Monte-Carlo simulation, and this allows us to compare data from the Monte-Carlo simulation, which is based on energy evaluations, with data from our Langevin dynamics simulation, which is based on force calculations. As an example, figure 6.7 on page 100 shows how the substrate fluctuates, comparing data from both methods. The results in this figure are representative of the excellent agreement between the results of both methods.

6.4.3 Finite size scaling

Figure 6.8 on page 100 shows how the instability temperature varies as a function of system size. For small numbers of vortices, N_p, the temperature oscillates slightly and for larger systems it becomes constant. Most importantly, there is no general trend visible although the data ranges from $N_\mathrm{p} = 90$ to $N_\mathrm{p} = 1512$. This insensitivity to the system size demonstrates the local nature of the transition from solid to liquid.

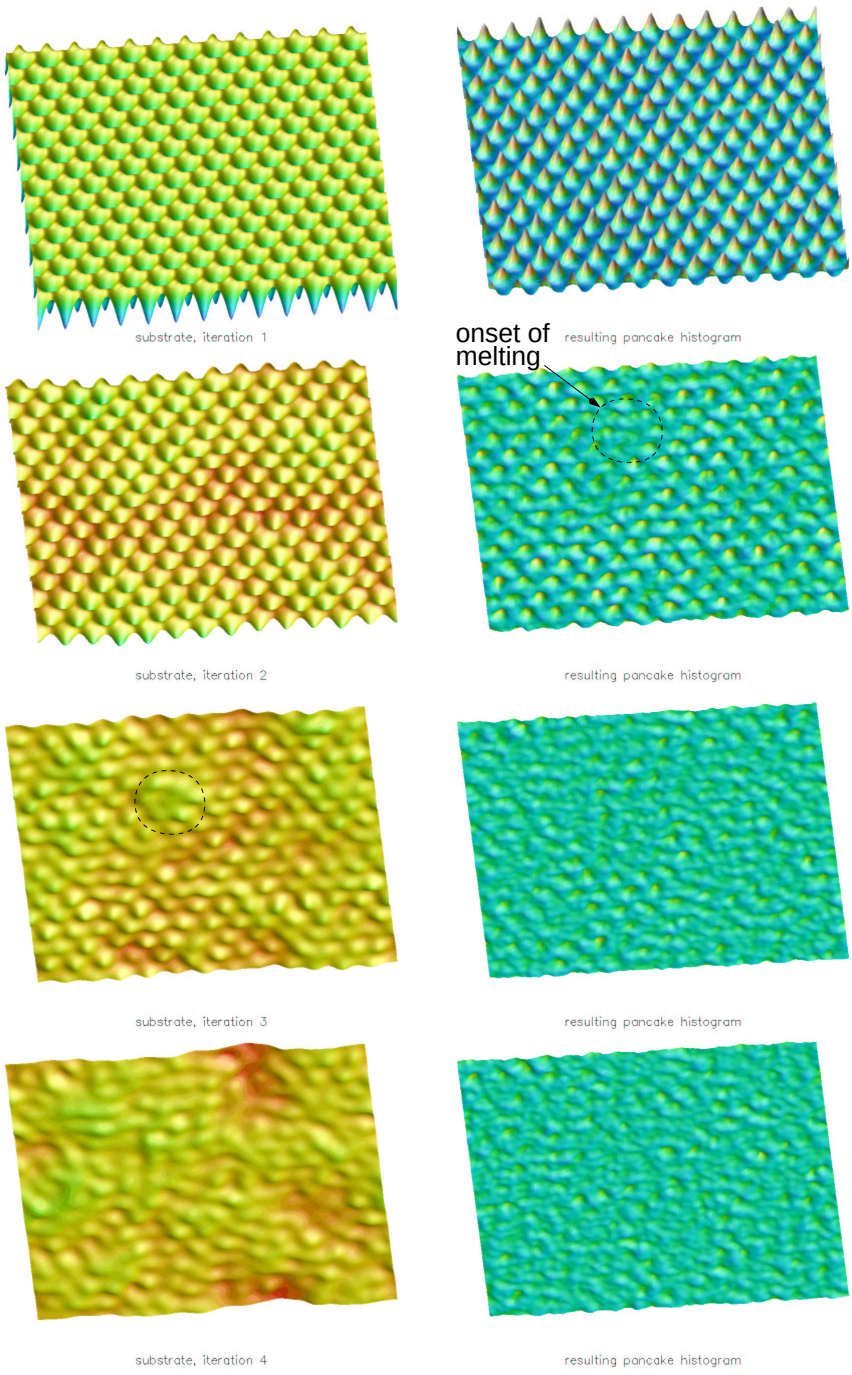

Figure 6.6:
The melting process computed using the full method for the substrate potential. Each row shows one substrate iteration with the substrate potential V_{MF} on the left, and the resulting pancake density ρ on the right. The initial substrate potential as shown in the upper left corner, is computed based on a hexagonal delta-peak pancake density, corresponding to the zero-temperature situation. When running the Langevin simulation, the pancakes fluctuate in the (strong) substrate potential, and this is reflected in the pancake density on the right, and in the second row which shows a flatter substrate potential (which is based on ρ as shown in the upper right corner.) The resulting pancake density after the second substrate-iteration shows an irregularity (indicated by circle). This is reflected in the substrate potential of the third iteration, which still shows regular patters. Both, the substrate and the pancake density, in the fourth iteration do not represent a solid anymore.

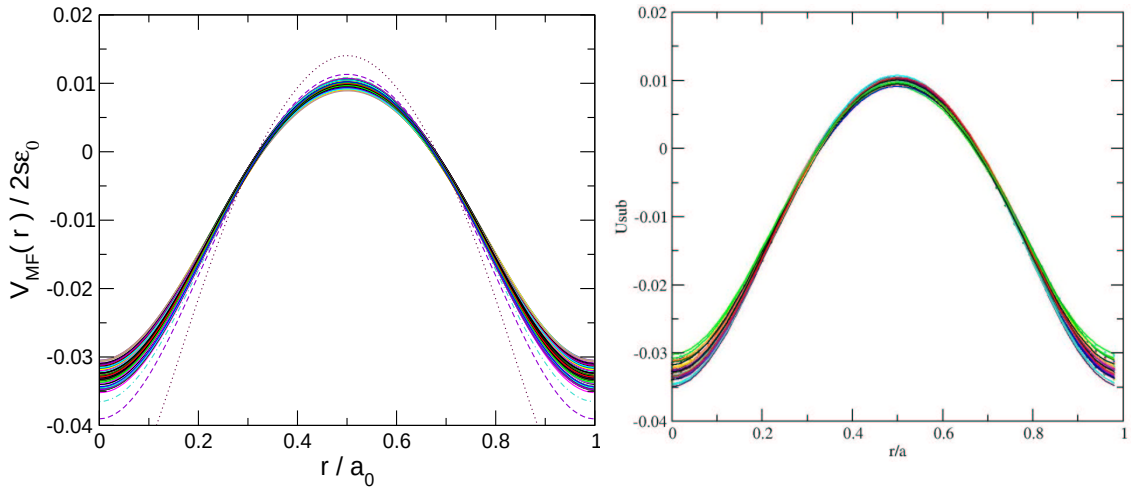

Figure 6.7: Comparison of the Monte-Carlo and the Langevin dynamics method for the computation of the substrate potential using the reduced-Q Fourier-filtered method. Both plots show $V_{\mathrm{MF}}(r)/2\epsilon_0 s$. *Left:* Results from Langevin dynamics simulations for 100,000 time-steps, one line for 500 time-steps. *Right:* Results from a Monte-Carlo simulations of 100,000 sweeps, one line for every 2000 sweeps. The agreement of the data is excellent. The anomalous curves (dotted, dashed, dash-dotted) in the Langevin plot on the left are the first three substrate-iterations which are not shown for the Monte-Carlo data.

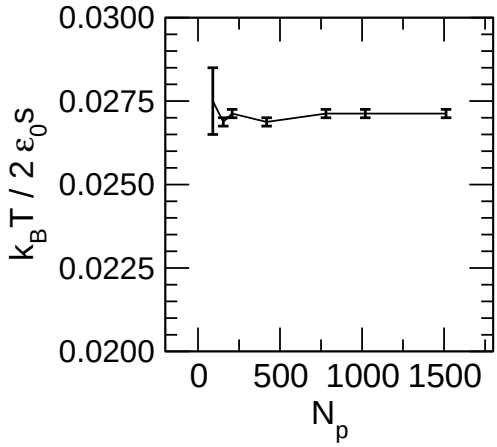

Figure 6.8: Finite-size investigation of instability temperature at $B = 0.398 B_\lambda$. The lower end of each error bar shows the highest temperature probed for which the system remains a solid, and the higher end of each bar shows the lowest temperature at which we found the system to melt into a liquid. The error bar at $N_{\mathrm{p}} = 90$ is bigger, because for this small pancake number, the system switches between solid and liquid state for a range of temperatures around the melting temperature. Note, that the temperature axis does not start from zero: for $N_{\mathrm{p}} = 1020$ the error bar shown corresponds to a relative error of less than 1%.

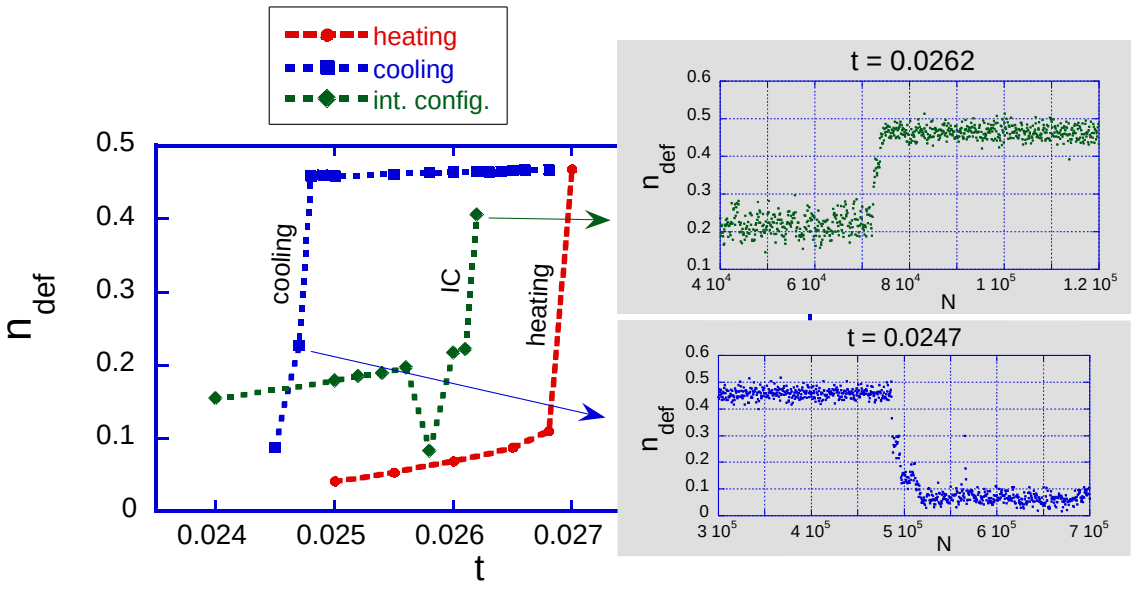

Figure 6.9: Example of a hysteresis loop obtained by heating a crystal (circles) and cooling a liquid (squares) at $B \approx 0.4 B_\lambda$. The crystal melts at $t = 0.027$, while the liquid freezes at $t = 0.0247$. Rhombs represent results obtained by simulations starting from an intermediate defective configuration with $n_{\rm def} \approx 0.17$, and this configuration melts at $t = 0.0262$, which we take as an estimate for the thermodynamic melting temperature. The insets on the right show dependencies of the defect concentration on the Monte-Carlo sweep N at the temperatures where the intermediate configuration melts (top) and the liquid configuration freezes (bottom).

6.4.4 Hysteresis loop and melting temperature

In section 6.4.1 we have determined the instability temperature by starting the simulation from a hexagonal crystal configuration for each temperature value. Here we describe another approach where we subsequently increase the temperature in one long simulation until the system melts. Data from such a Monte-Carlo run are shown in figure 6.9. By subsequent cooling of the liquid configuration, we can determine a freezing temperature. The Langevin dynamics method yields similar results. Animations of the freezing and melting process (computed with Langevin dynamics) can be found[1] in *Fangohr et al.* (2002).

The thermodynamic melting temperature is the temperature for which the free energy $F = U - TS$ of the liquid and the solid state cross, and will be located between the freezing temperature and the instability temperature. We therefore know in which range the thermodynamic melting temperature is located. We have used an empirical method to obtain a better estimate of the melting temperature:

[1]There is a webpage specified in reference [32] given in the caption of figure 7 of this paper http://xxx.lanl.gov/abs/cond-mat/0210580 which shows animations at different fields and temperatures.

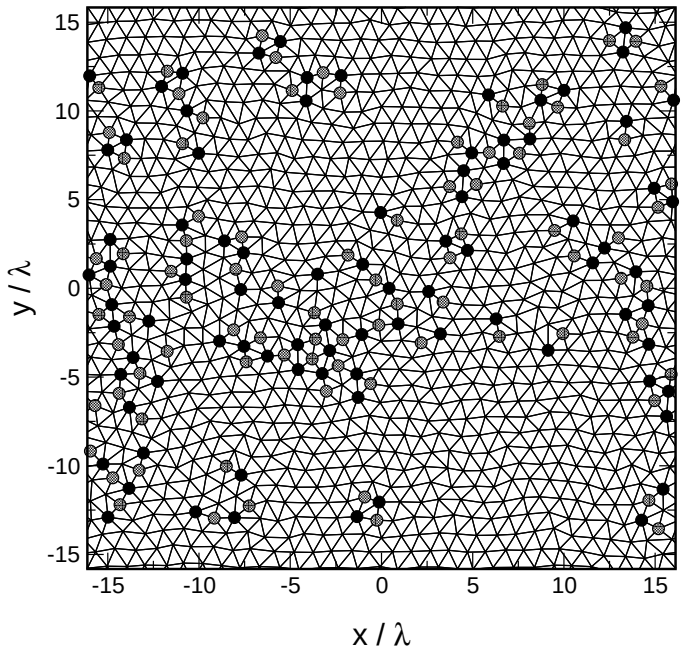

Figure 6.10: The intermediate configuration. Taken from a Langevin dynamics simulation at the very moment the system started melting. Circles mark topological defects, *i.e.* vortices with 5 nearest neighbours (black) and 7 nearest neighbours (gray). The defect density is $n_{\rm def} = 0.1709$.

Firstly, we create a configuration of vortices which is close to melting, and which we call "intermediate configuration" (IC) because it is not fully molten, but it is not a solid either. An example is shown in figure 6.10. To create this intermediate configuration, we run a two-dimensional simulation (*i.e.* without the substrate potential) which we start from a hexagonal lattice configuration. We increase the temperature to a value just above the two-dimensional melting temperature $T_{\rm m}^{\rm 2d}$. As the number of simulated time-steps increases, the system will become more and more disordered due to the thermal fluctuations, and eventually start to melt. At that point the structure factor peaks start decaying strongly, and the defect fraction increases similarly. We take the vortex positions from this time-step, and store them in a file. This is the intermediate configuration as shown in figure 6.10.

Secondly, we use the intermediate configuration as the starting condition for a set of runs in the three-dimensional system (*i.e.* with the substrate). In comparison to the two-dimensional system which we used to create the intermediate configuration, the substrate potential stabilises the vortices but at the same time we study higher temperatures which compensate for this. For each field value, we probe different temperatures between the freezing temperature and the instability temperature, starting from the intermediate configuration. Figure 6.9 (rhombs) shows how these runs either melt (for $t \geq 0.0262$) or stay solid (for $t < 0.0262$). We take this transition point (here at $t_{\rm IC} = 0.0262$) as the best estimate for the thermodynamic melting temperature.

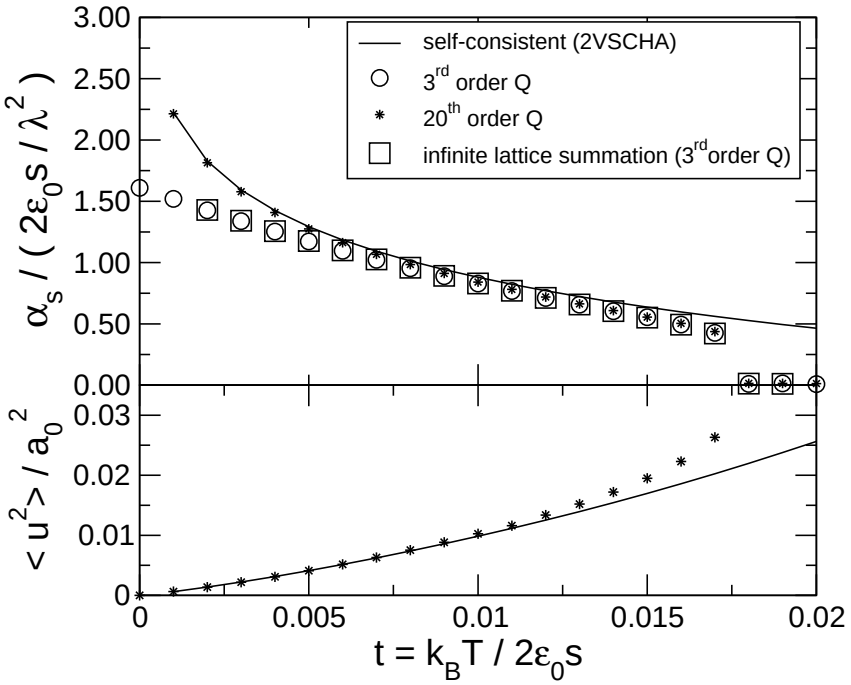

Figure 6.11: *Top:* The substrate curvature $\alpha_{\rm s}$ at $B = B_\lambda$. Shown is our numerical solution using the Fourier-filtered method with Q-vectors up to $20^{\rm th}$ order (stars), and up to $3^{\rm rd}$ order (circles) in comparison with the 2VSCHA from *Dodgson et al.* (2000b) (solid line). We have also shown results for $Q_{\rm max} = 3Q_0$ using an infinite lattice summation for the in-layer interaction (squares). *Bottom:* The pancake fluctuation width $<u^2>$ (stars) in comparison with the 2VSCHA result (solid line).

Although it is hard to formally justify this approach, we argue that the intermediate configuration is as close to melting as possible, such that it is very sensitive as to whether the environment (substrate and temperature) favour a liquid or a solid state.

6.4.5 Substrate curvature α

We can quantify the strength of the substrate potential with

$$\alpha_{\rm s} = \frac{1}{N_{\rm p}} \sum_j \frac{\partial^2}{\partial x^2} V_{\rm MF}(\mathbf{R}_j - \mathbf{R}_j^0). \tag{6.44}$$

This is the curvature of the potential evaluated at deviations $\mathbf{R}_j - \mathbf{R}_j^0$ from the equilibrium lattice positions $\mathbf{R}_j^0$ and averaged over pancake positions $\mathbf{R}_j$. The second derivative can be taken analytically from (6.41).

Figure 6.11 shows in the upper plot how $\alpha_{\rm s}$ varies with temperature. The solid line is the semi-analytical prediction using a two-vertex self-consistent harmonic approximation (2VSCHA) (*Dodgson et al.*, 2000a) which includes cubic anharmonicities, and is taken from *Dodgson et al.* (2000b). All other data are simulation results

from the Fourier-filtered method. The stars show α_s computed using the reduced-Q Fourier-filtered method with $\mathbf{Q}_\mu$-vectors up to 20^{th} order. For low temperatures the data nearly coincide with the 2VSCHA-solution. Close to melting, the 2VSCHA-α_s is larger than the numerical result. The circles show results using $\mathbf{Q}_\mu$-vectors up to 3^{rd} order, as shown in Fig 6.3. Close to the transition from solid to liquid around $t \approx 0.0175$ these data agree perfectly with the higher-order data. At lower temperatures the 3^{rd} order results deviate from the 20^{th} order because $<u^2>$ becomes smaller in the Debye-Waller factor (6.43). However, as long as we are interested in temperatures close to the transition, the 3^{rd} order approach is sufficient.

The square boxes are computed using the 3^{rd} order approach, but instead of smoothly reducing the pancake interaction (Section 4.4) at a distance of $7a_0$, we use an infinite lattice summation technique for the logarithmic interaction (*Grønbech-Jensen*, 1996). This demonstrates that it is sufficient to use a (smooth) cut-off for the in-layer pancake interactions.

6.4.6 Pancake fluctuation width

We compute the average pancake fluctuation width $<u^2>$ by fitting to a distribution where each pancake is normally smeared around its equilibrium position $\mathbf{R}_j^0$

$$\rho(\mathbf{r}) = \frac{1}{2\pi\sigma^2} \sum_j \exp\left(-\frac{|\mathbf{r} - \mathbf{R}_\mathbf{j}^\mathbf{0}|^2}{2\sigma^2}\right). \tag{6.45}$$

The Fourier transform of $\rho(\mathbf{r})$ is

$$\begin{aligned} \rho(\mathbf{q}) &= \exp\left(\frac{-\sigma^2 q^2}{2}\right) \sum_j \exp(-i\mathbf{q}\cdot\mathbf{R}_j^0) \\ &= (2\pi)^2 n_0 \exp\left(\frac{-\sigma^2 q^2}{2}\right) \sum_\mu \delta^2(\mathbf{Q}_\mu + \mathbf{q}). \end{aligned}$$

The Fourier components $\rho(\mathbf{Q}_\mu)$ have the Debye-Waller factor as an envelope, and by fitting a Gaussian to it, we can determine $<u^2> = 2\sigma^2$. We use the standard Levenberg-Marquardt algorithm to find σ^2 numerically (*Press et al.*, 1995).

The lower part of figure 6.11 shows computed values for $<u^2>$. We express $<u^2>$ in units of a_0^2 and it increases from 0 at zero temperature towards 0.028 close to the transition, which corresponds to a Lindemann number $c_\text{L} \approx 0.168$ at $B = B_\lambda$. In agreement with an over-estimation of α_s by the 2VSCHA, $<u^2>$ is underestimated in comparison with the numerical results close to the melting transition.

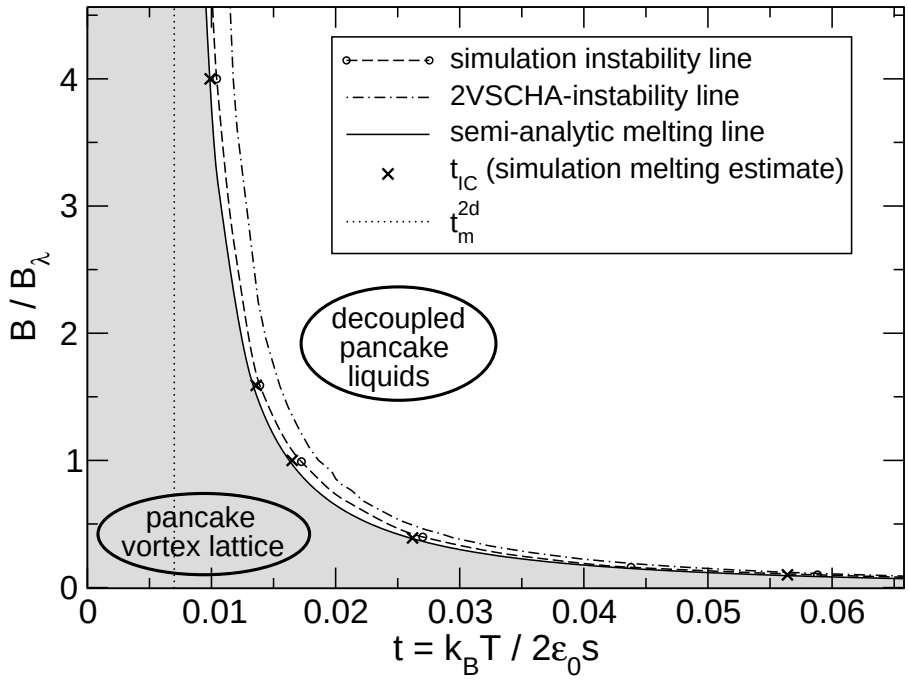

Figure 6.12: Phase diagram of the electromagnetically coupled three-dimensional pancake system. Numerically computed instability line (circles on dashed line) in comparison with instability line from 2VSCHA (dash-dotted line). Also shown is an estimate for the melting line (*Dodgson et al.*, 2000b) to be compared with the crosses which show the temperatures at which the intermediate configuration melts. We have shaded the solid phase underneath the semi-analytical melting line in gray. The melting temperature $t_{\mathrm{m}}^{\mathrm{2d}}$ of a two-dimensional system is shown by a dotted line.

6.4.7 Phase diagram

As demonstrated in section 6.4.1, we can determine for each parameter pair (B, T) whether the pancake system remains a three-dimensional pancake lattice, or whether it is unstable towards the liquid phase which consists of decoupled two-dimensional liquids and is sometimes called pancake gas, even though there are still very strong in-plane correlations in the decoupled layers. In the absence of Josephson coupling, a line-like liquid regime is expected only at extremely small magnetic fields (*Blatter et al.*, 1996).

We investigate the parameter space in the $B - T$-plane, and plot an instability line into the phase diagram of the system, which is shown in Fig 6.12 (circles on dashed line). We have also shown an estimate of the instability line that has been computed using the two-vertex self-consistent harmonic approximation (2VSCHA, dash-dotted) for the substrate model (*Dodgson et al.*, 2000b). Since in this work we explicitly compute the pancake positions without using approximations (within the substrate model), we expect our result to be more accurate than the 2VSCHA.

It can be seen that the 2VSCHA slightly overestimates the temperature for the instability line but predicts the field-dependence rather well.

Melting occurs when the free energy $F = U - TS$ of the liquid and the solid state cross, and this happens below the instability temperature and above the freezing temperature (section 6.4.4). We have shown the melting line computed using a semi-analytical approach (*Dodgson et al.*, 2000b) for the substrate model (solid line) and the temperatures t_{IC} at which the intermediate configuration melts, which is our best estimate of the melting temperature. The data are in good agreement.

For increasing fields B, the substrate becomes weaker and weaker and the melting temperature drops. In the limit of $B \to \infty$ we recover a two-dimensional system with logarithmic interactions for which melting has been estimated (*de Leeuw and Perram*, 1982, *Caillol et al.*, 1982, *Choquard*, 1983) to occur at $\Gamma_{\mathrm{m}}^{\mathrm{2d}} \approx 140 \pm 10 \Leftrightarrow t_{\mathrm{m}}^{\mathrm{2d}} \approx 0.007$, which is consistent with our results.

At low fields the pancake stacks are widely separated and interact only weakly with each other. In this limit the system melts below the evaporation transition of an isolated stack of pancakes (*Clem*, 1991, *Bulaevskii et al.*, 1991) at $\Gamma = 4 \Leftrightarrow t = 0.25$. In agreement with this, we find that the transition line approaches $t \approx 0.25$ for $B \to 0$ (see figure 6.2).

6.4.8 Latent heat and jump in entropy

We compute the latent heat per pancake, L_{p}, by taking the difference of the internal energy between the solid and the liquid phase at the melting temperature T_{m} (and we use $T_{\mathrm{m}} = T_{\mathrm{IC}}$)

$$L_{\mathrm{p}} = \frac{1}{N_{\mathrm{p}}} \left(U_{\mathrm{liquid}} - U_{\mathrm{solid}} \right) \tag{6.46}$$

$$= \frac{1}{N_{\mathrm{p}}} \left(E_{\mathrm{liquid}}^{\mathrm{in}} - \left(E_{\mathrm{solid}}^{\mathrm{in}} + E^{\mathrm{coup}} \right) \right). \tag{6.47}$$

The internal energy U of one layer in the solid phase consists of the in-plane energy E^{in} (6.23) and the inter-layer coupling energy E^{coup}, whereas $E^{\mathrm{coup}} = 0$ in the liquid phase in our model. In order to compute E^{coup} for the solid phase, we use (6.14) where the second sum vanishes due to the definition of $\delta\rho_n$:

$$E^{\mathrm{coup}} = \frac{1}{2} \int \mathrm{d}^2 r \; V_{\mathrm{MF}}(\mathbf{r}) \rho(\mathbf{r}). \tag{6.48}$$

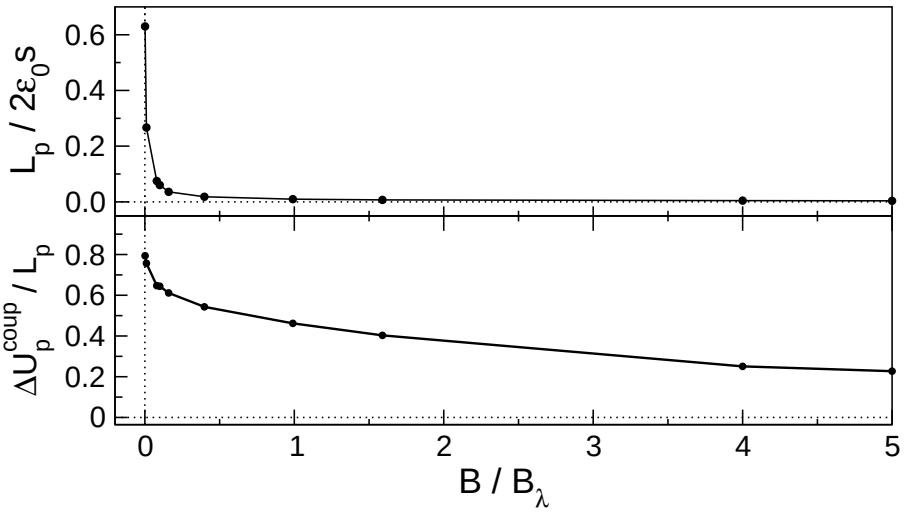

Figure 6.13: *Top:* Latent heat L_p per pancake across the melting transition as a function of field. *Bottom:* Jump in inter-layer coupling $\Delta U^\mathrm{coup} = E^\mathrm{coup}$ normalised by latent heat L_p.

For the Fourier-filtered methods

$$\begin{aligned} E^\mathrm{coup} &\overset{(6.40)}{=} \frac{1}{2}\int \mathrm{d}^2 r\, \frac{1}{(2\pi)^2}\sum_\mu \mathcal{U}(\mathbf{Q}_\mu)\rho_{\mathbf{Q}_\mu}\exp(i\mathbf{Q}_\mu\cdot\mathbf{r})\rho(\mathbf{r}) \\ &= \frac{1}{2}\frac{1}{(2\pi)^2}\sum_\mu \mathcal{U}(\mathbf{Q}_\mu)\rho_{\mathbf{Q}_\mu}\int \mathrm{d}^2 r\, \rho(\mathbf{r})\exp(i\mathbf{Q}_\mu\cdot\mathbf{r}) \\ &\overset{(6.6)}{=} \frac{1}{2}\frac{1}{(2\pi)^2}\sum_\mu \mathcal{U}(\mathbf{Q}_\mu)\rho_{\mathbf{Q}_\mu}\sum_j \exp(i\mathbf{R}_j\cdot\mathbf{Q}) \\ &\overset{(6.42)}{=} \frac{1}{2}\frac{L_x L_y}{(2\pi)^4}\sum_\mu \mathcal{U}(\mathbf{Q}_\mu)|\rho_{\mathbf{Q}_\mu}|^2. \end{aligned} \tag{6.49}$$

For the full method, we have $\rho(\mathbf{r})$ as a histogram available, and we can integrate (6.48) numerically.

The top plot of figure 6.13 shows how the latent heat per pancake, L_p, varies as a function of field. We have shown the jump in inter-layer coupling energy normalised by the latent heat in the bottom part to demonstrate the contribution of the inter-layer coupling to the latent heat. This plot shows that the substrate contribution to the latent heat dominates at low fields, and becomes less and less important towards high fields.

Figure 6.14 shows the entropy jump across the transition as a function of field, which we have computed using $\Delta S_\mathrm{p} = L_\mathrm{p}/T_\mathrm{m}$. For large B, we expect ΔS_p to approach the value for a two-dimensional system with logarithmic interactions, for which estimates range from $\approx 0.4 k_\mathrm{B}$ (*Caillol et al.*, 1982, 256 particles) to $\approx 0.17 k_\mathrm{B}$

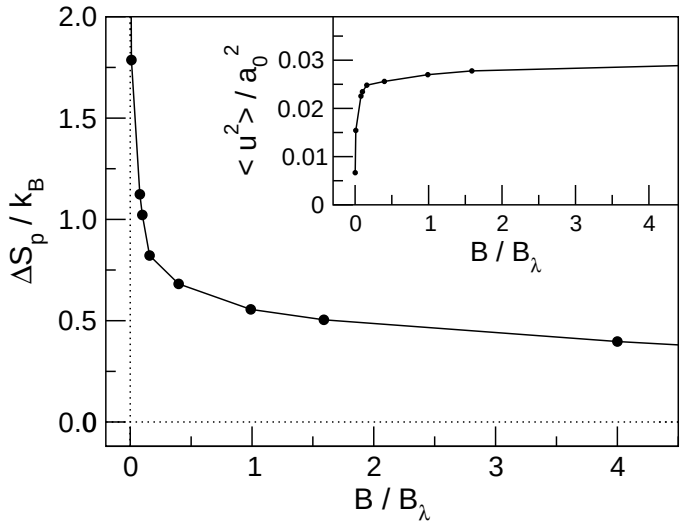

Figure 6.14: Entropy jump ΔS_p per pancake as a function of field B. Inset: Pancake fluctuation width $<u^2>$.

(*Choquard*, 1983, 511 particles) and lower.[2]

At low fields the entropy weakly diverges for $B \to 0$. We understand this as follows: the possible configurations in the liquid state scale as $\sim a_0^2/\xi^2$, where ξ^2 is the size of a pancake, and a_0^2 is the space it can occupy. For the solid state close to the transition the reduced configuration space is $\sim <u^2>/\xi^2$, because the pancake is confined to an area $\sim <u^2>$. We get thus an entropy difference $\Delta S_\mathrm{p} \sim \ln(a_0^2/<u^2>)$. Since $<u^2>$ approaches a finite field-independent value of the order of λ^2 this explains the observed divergence of ΔS_p at $B \to 0$.

The value of the entropy jump across the transition is consistent with experimental measurements in BSCCO (*Zeldov et al.*, 1995) which report for low fields values for ΔS_p up to $\approx 1.5 k_\mathrm{B}$, and *Morozov et al.* (1996) find ΔS_p up to $\approx 6 k_\mathrm{B}$. However, *Rae et al.* (1998) pointed out that for the same measurements, the real entropy jump might be higher by a factor of 2 when re-interpreting the data. They also state that in simulations, the entropy associated with additional vortex-lines in the liquid phase (due to the increased density in comparison to the solid phase) cannot be accounted for.

The pancake fluctuation width $<u^2>$ relative to the vortex lattice spacing a_0, changes as a function of field (inset figure 6.14), and decays for small fields. The reason for this is that at low fields the pancake fluctuation width is bounded by the width of the substrate potential, which is of the order of λ (see figure 6.2), while $a_0(B) = \sqrt{(2\Phi_0)/(\sqrt{3}B)} \propto 1/\sqrt{B}$ grows for decreasing B. A field-dependent ratio

[2] In preliminary results of two-dimensional melting studies with 4080 particles, *Koshelev* (2002) finds an entropy jump $\leq 0.0005 k_\mathrm{B}$.

$<u^2>/a_0^2$ has been observed before (*Ryu et al.*, 1992), and needs to be considered when using the Lindemann criterion (see footnote on page 14).

6.4.9 Phase diagram in the presence of pinning

The model we have described can be extended to study the same pancake system in the presence of pinning using either the full method or the (reduced-Q) Fourier-filtered method.

Using the full method, it is not sufficient to add random disorder to the layer simulated, because the substrate minima can follow the pancakes towards minima in the pinning potential. This would correspond to using the same (random) pinning potential in all layers, and is not representative of real samples. Instead, we have to perform a parallel simulation of p two-dimensional layers, each experiencing its own individual pinning potential in addition to a common substrate potential. After a number of time steps (or sweeps), the common substrate is re-computed using an average of the pancake density taken over the p parallel simulations. The number of necessary layers p has to be sufficiently large, maybe of the order of $p \approx 10$, to ensure that the pinning potential is sufficiently averaged over the layers. This is computationally p times as hard as performing the simulations described in the previous sections.

However, using the Fourier-filtered method, the substrate potential cannot follow pancakes to minima in the pinning potential. Instead, a displacement of a vortex from its ideal lattice position (due to the pinning potential) will result in a reduced depth of the substrate potential, in the same way that a displacement due to thermal fluctuations weakens the substrate. If our system has sufficiently many pancakes, then the average of the pancake displacements in one layer approximates well the pancake displacements averaged over different layers due to different random pinning potentials.

Initial results which were computed using the Fourier-filtered method are shown in figure 6.15. The random pinning potential is similar to the one shown in figure 5.1 on page 71, and is correlated over a length $\approx 0.07\lambda$ which is of the order of the coherence length ξ. For small fields the hexagonal pancake lattice is nearly as stable as without disordering pinning. For larger fields, the transition line from an ordered pancake lattice to a disordered system deviates from the instability line, and the transition temperature reduces to zero at $B \approx 3B_\lambda$. The shape of this disorder transition is in good agreement with theoretical predictions (section 2.4.2.1), and experimental results for BSCCO (*Cubitt et al.*, 1993, *Doyle et al.*, 1997, *Khaykovich et al.*, 1997).

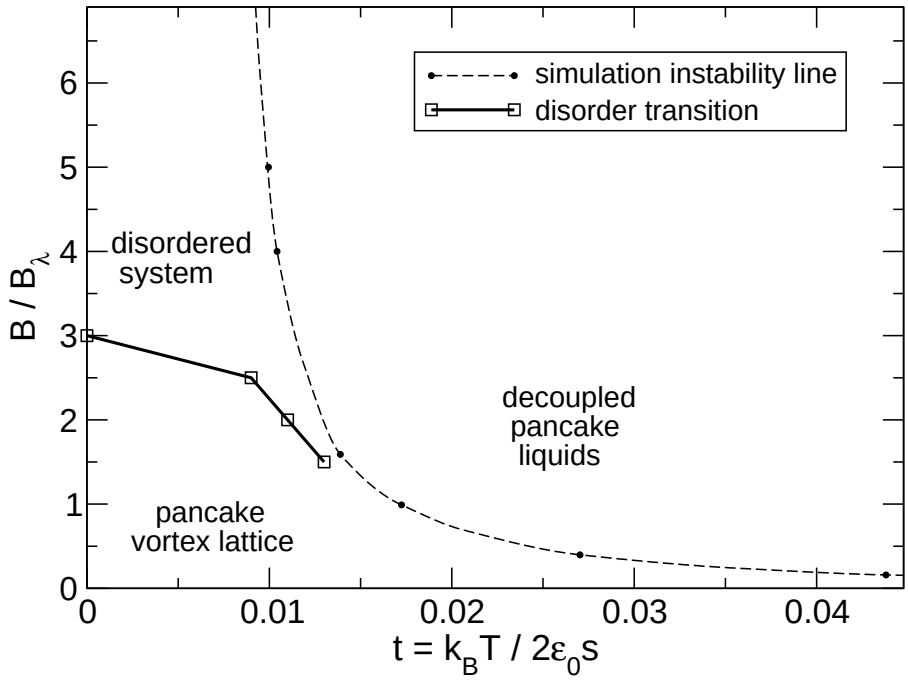

Figure 6.15: Phase diagram in presence of pinning

The transition line can be understood as follows. The pancakes experience two potentials: Firstly, the substrate potential which stabilises the hexagonal configuration. Without the substrate, the system would melt (at all fields) above the two-dimensional melting temperature (see figure 6.12). Secondly, pancakes experience the random pinning potential which tends to destroy hexagonal order because (in general) it displaces pancakes from their ideal position. We can simply superimpose these two contributions to see the effective potential, and this is shown in figure 6.16 on the following page.

For low fields, say $B \approx 0.5 B_\lambda$, the substrate is strong and the vortex spacing is large. This is the case shown in figure 6.16: While the effective pinning is slightly rough and not as regular as the substrate potential, it clearly shows the periodicity of the substrate. The random pinning might displace a pancake slightly, but the displacement distance — which is of the order of the correlation length of the random pinning — is small in comparison to the vortex lattice spacing.

Figure 6.17 shows how the effective potential changes with increasing field. At higher fields, the vortex density is higher and the substrate is weaker. Therefore, the (unchanged) random pinning is now relatively more important. Also, the displacement of a pancake due to the random pinning is still of the order of the correlation length of the random pinning, but since the vortex lattice spacing is much smaller

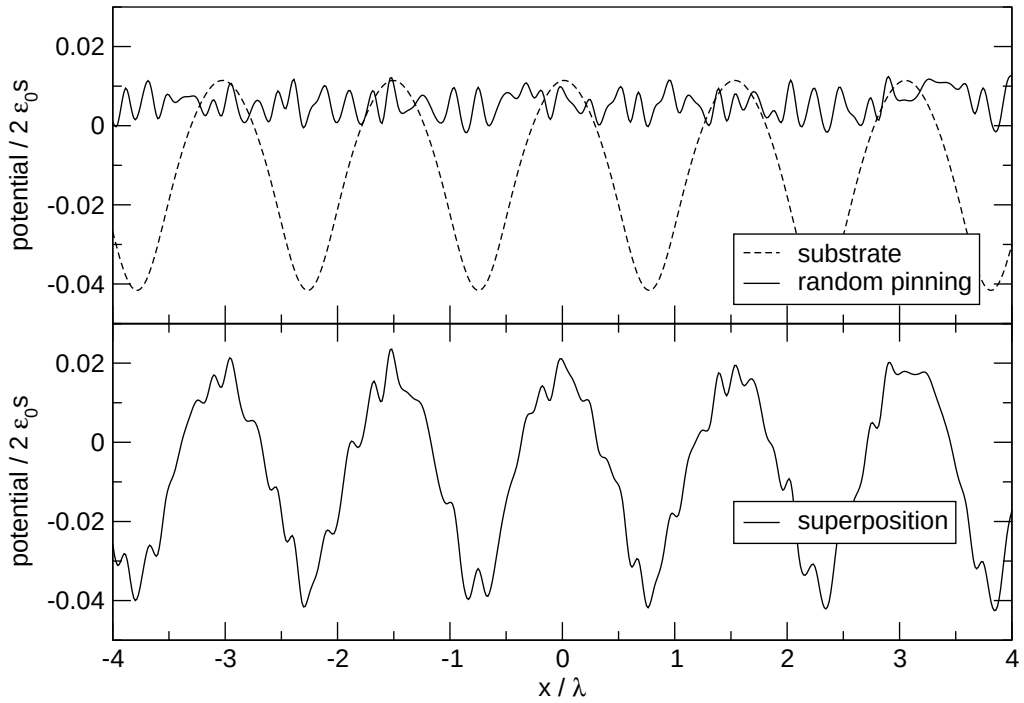

Figure 6.16: Superposition of substrate and random pinning potential. *Top:* The substrate potential (dashed) at $B = 0.5B_\lambda$ and a random disorder potential (solid line). *Bottom:* Superposition of substrate and random pinning; this is the effective potential the pancakes experience.

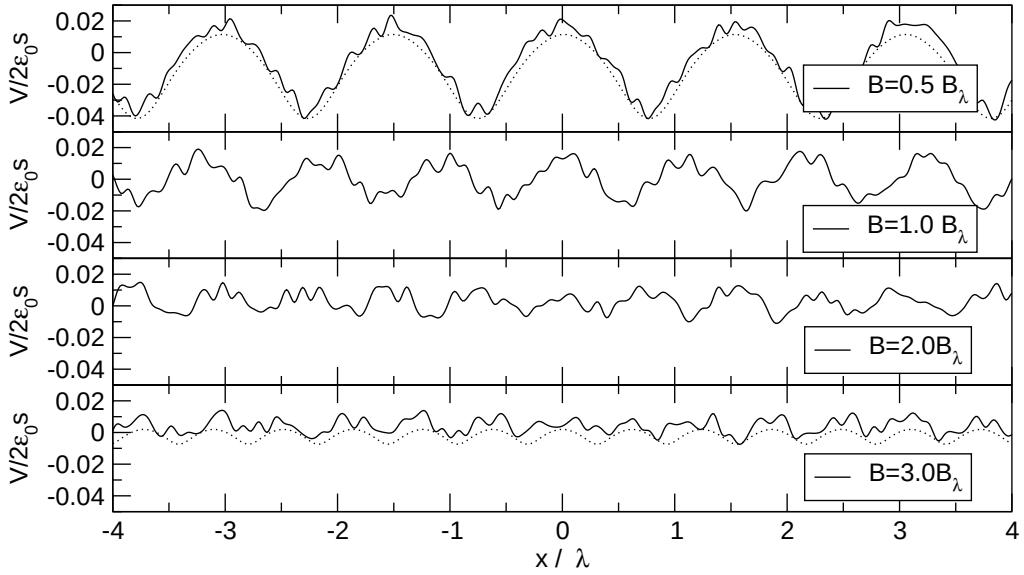

Figure 6.17: Each of the four plots shows the superposition (solid line) of the substrate potential and the random pinning potential (see figure 6.16) for increasing fields. For the first ($B = 0.5_\lambda$) and the last field ($B = 3B_\lambda$) we have also shown the substrate potential (dotted line) for clarity. The axis limits are identical for all four plots. It can be seen that the amplitude of the substrate potential decreases with increasing field (because the vortex-lattice spacing decreases), but the random pinning remains constant (no change in the atomic structure of the material as a function of field). The resulting effective potential loses its periodic nature and appears completely disordered at high fields.

at high fields, this displacement relative to the vortex lattice spacing is much higher, and can de-stabilise the hexagonal system more easily.

Increasing the field increases the relative importance of the random pinning and at some point the hexagonal configuration breaks down, resulting in the disorder transition line as shown in figure 6.15.

We cannot conclude what type of vortex solid we find for temperatures below the disorder transition line (*i.e.* Bragg glass or crystal), because we impose a hexagonal crystal structure through the Fourier-filtered substrate potential. Further studies should be able to reveal the nature of the system above the transition line (vortex glass or liquid).

6.5 Conclusions

In this chapter we have applied a numerical simulation to the suggestion of *Dodgson, Koshelev, Geshkenbein and Blatter* (2000b) to treat the three-dimensional layered pancake system with a mean field approach for the inter-layer interactions, turning the problem into solving a two-dimensional system in the presence of a self-consistent substrate potential. *Dodgson et al.* (2000b) studied this model with semi-analytical methods. The 2-vertex self-consistent harmonic-approximation (2VSCHA) was used to estimate the instability line of the pancake lattice. Also the melting line was estimated by comparing the elastic free energy of the lattice within the substrate model to the free energy of independent 2D liquids, taken from numerical simulations.

Here we have presented results from full numerical simulations of the substrate model. We have directly calculated both the instability and melting lines. We find the transition to be of first order, in agreement with theoretical expectations (section 2.4.2.1) and experimental measurements (for example *Zeldov et al.*, 1995). Our result for the instability line has a very similar field-dependence to that of the 2VSCHA, which we find to slightly overestimate the instability temperature. Our estimate of the melting line is in good agreement with the data given by *Dodgson et al.* (2000b). We compute the pancake fluctuation width $<u^2>$ and show how it varies as a function of temperature: the variation is significantly non-linear below the melting transition. We also calculate the entropy jump across the melting transition, which diverges weakly towards small fields and large melting temperatures.

While we have found a satisfying agreement between our results here and the earlier approximate work of *Dodgson et al.* (2000b), the true motivation of this

project are the possible extensions that can be studied. There is now the exciting prospect to study this pancake vortex system in the presence of pinning disorder for which we have shown initial results. Also, by extending the model to use several layers, it is possible to include Josephson coupling between them, which will fully describe an anisotropic layered high-temperature superconductor.

Chapter 7

Conclusions

7.1 Summary of main findings

We have implemented and used a numerical model of the vortex state. Vortices are represented by massless point-like particles that repel each other. The equation of motion is based on Langevin dynamics, *i.e.* vortices experience a viscous drag force proportional to their velocity and a stochastic noise force that emulates thermal fluctuations, in addition to vortex-vortex interactions, the Lorentz force, and pinning forces. The resulting set of differential equations is integrated numerically. The model is appropriate for the study of pancake vortices in high-temperature superconductors. It can also be employed to study "rigid" vortex lines in thin films and bulk material as well as the two-dimensional one component electron plasma. More generally, the model describes the statics and dynamics of a many-body system with competing interactions.

In chapter 4 we investigate a two-dimensional vortex system in the absence of pinning, and demonstrate that employing a cut-off to long-range interactions introduces disordered vortex configurations with energies below the energy of the ground state of the system, which is known to be a hexagonal lattice. We have simulated the shearing process of a two-dimensional vortex lattice, and find that using the simple cut-off the shear modulus is negative, *i.e.* the material does not act against a shearing force, but instead collapses.

These problems are numerical artefacts and severely hinder the numerical investigation of the vortex state with its subtle combination of elastic, thermal and pinning energies.

We have revealed that the reason for these artificial configurations is that the cut-off of the long-range vortex-vortex interaction introduces a variety of local energy

minima in phase space which are energetically located below the hexagonal lattice energy, and are thus quickly occupied by the simulations which aim to minimise energy. In real space there is a tendency for vortices to align along the cut-off circles.

The reported problems have been resolved by reducing the interaction smoothly over a few lattice spacings. To ensure that vortices hardly experience any difference between being in- or outside the cut-off circle, the derivative of the smooth function at the cut-off needs to be zero, which can be achieved by interpolating with a cubic polynomial. In simulations employing the modified force, the hexagonal lattice is the global energy minimum. The smooth cut-off can be applied to any long-range interaction in particle simulations.

For studies of rigid vortices in bulk material, the vortex-interaction potential is given by the modified Bessel function $K_0(r)$. We have developed a new infinite lattice summation which is at least 20,000 faster than similar methods used previously. The infinite lattice summation removes the need to cut off the interaction, and therefore overcomes the artificial configurations as well.

We have compared results from simulations using the infinite lattice summations with simulations employing a smooth cut-off and find no difference in their statistical behaviour.

In chapter 5 we apply the methods we have developed to deal with the long-range interactions, and study two-dimensional vortex systems in the presence of pinning and a Lorentz force. We drive the vortices over a weak random pinning potential, and they form a moving Bragg glass. Once the static rough channels have developed, we determine the critical transverse force by applying a small and slowly increasing transverse force until the system de-pins in the transverse direction.

We have performed a finite-size analysis, and have shown how the critical transverse force scales with system size up to 3000 vortices. We find that it decreases up to a system size of ≈ 1000 vortices, but stays constant for larger system sizes. This is in contradiction to *Olson and Reichhardt* (2000), where the critical transverse force was found to be constant for all system sizes investigated. We also find that it is important to study systems with more than 1000 vortices, as the behaviour for smaller systems can differ qualitatively.

We show how the critical transverse force varies as a function of the pinning strength, and we demonstrate that it is an order parameter of the moving glass. We find that the critical transverse force decreases with an increasing velocity of the system. Data on the apparent critical transverse force at finite temperatures have

been obtained, and these findings are in agreement with predictions from analytical work. Our results support the moving glass theory of *Giamarchi and Le Doussal* (1998).

We have also addressed the issue of the outstanding experimental verification of the critical transverse force. We introduce the quantity σ which can be obtained experimentally, and provide simulated data for σ to allow comparison with experiments. If experimental measurements showed a $\sigma < 1$, then this would prove the existence of transverse barriers, such as the critical transverse force (assuming it is a single domain sample with no twin-boundaries or other extended defects that could channel vortices). We predict, that the largest critical transverse force can be found for low temperatures and small longitudinal driving forces.

In chapter 6, we extend our model to study the vortex state in three-dimensional layered high temperature superconductors and study vortex matter in layered superconductors in the limit of zero Josephson coupling. We have applied a numerical implementation to the suggestion of *Dodgson et al.* (2000b) to exploit the long-range nature of the electro-magnetic interaction between pancake vortices in the c-direction and to employ a mean-field method. All attractive inter-layer interactions are described by a substrate potential, which pancakes experience in addition to the in-layer pancake repulsion.

For the in-layer interactions we employ our simulation of the two-dimensional vortex state, and add extra forces and energies resulting from the superimposed substrate potential. Using a time-averaged pancake density, we re-compute the substrate potential iteratively, until the self-consistent method converges, depending on temperature, either to a pancake lattice or a pancake liquid. This mean-field approach reduces the dimensionality of the problem from 3 to 2, and results in a speed-up of about 100^2 in comparison to performing the simulation in a straightforward manner by stacking two-dimensional simulations on top of each other.

Using this model, we compute the melting line and the instability line of the three-dimensional weakly coupled pancake system which we compare with semi-analytical approximations. Our numerically obtained instability line is located at slightly smaller temperatures than the approximate solution, but the methods agree well on the field-dependence of the temperature. Our melting line is in good agreement with the semi-analytic prediction.

We compute the pancake fluctuation width $<u^2>$ and demonstrate its dependence on both temperature and field. For a fixed field, we find that the variation of $<u^2>$ is non-linear below the melting transition. The ratio $<u^2>/a_0^2$ at the melting

transition is a function of the field (a_0 is the average vortex spacing), and decreases strongly for low fields. This has to be taken into account when employing the Lindemann criterion.

We also calculate the entropy jump, ΔS_p, across the melting transition, which diverges weakly towards small fields and large melting temperatures. This is in agreement with the decay of the relative pancake fluctuation width $<u^2>/a_0^2$ at small fields because qualitatively $\Delta S_\mathrm{p} \sim \ln(a_0^2/<u^2>)$.

In summary, we have found a satisfying agreement between our results as presented in this report and the earlier approximate work of *Dodgson et al.* (2000b).

The usefulness of our numerical implementation lies in its versatility: the method can be extended to include pinning effects, which cannot be achieved by analytical means. We provide results from initial computations, and find a order-disorder transition with increasing field in agreement with experimental data and analytical predictions.

The implementation of the substrate method can be extended further: by using several layers, Josephson coupling can be included between them, and this will fully describe anisotropic layered high temperature superconductors.

7.2 Suggested future work

It would be interesting to carry further the work presented in chapter 6, and to investigate the three-dimensional vortex state in the presence of random pinning in depth.

The detailed shape of the disorder transition line, its connection to the melting line and its dependence on the pinning strength are obvious questions to follow. In order to be able to better compare our results with experiments, we suggest to combine these studies with dynamic simulations in which we determine the critical force required to de-pin a (two-dimensional) vortex system in the presence of the same pinning as used for the phase-diagram studies. Doing so, one could relate a critical current to the magnetic induction at which we expect the order-disorder line.

In the limit of high fields, the individual layers are virtually decoupled and behave like two-dimensional systems with logarithmic repulsion. This limiting case of the substrate model has not been fully understood: the transition temperature has been predicted by computer simulations 20 years ago, to be $t_\mathrm{m}^\mathrm{2d} \approx 1/142 \approx 0.007$. This value is compatible with more recent investigations by ourselves, and *Koshelev* (2002). However, the order of the transition is not unambiguous (see section 6.4.8).

One of the challenges is the required equilibration of the defects and the diverging correlation time close to the melting transition. Recent work on a more complicated vortex system with inter-layer interactions (*Price*, 2000) suggests that using a novel Hybrid Monte-Carlo method could help to overcome these problems. The two-dimensional melting transition in the scale-free system with logarithmic interactions could be well suited to evaluate the Hybrid Monte-Carlo method in comparison to Monte-Carlo and Langevin dynamics methods, and to assist in the determination of the order of the melting transition.

Eventually, the addition of Josephson coupling to the substrate model would remove the main approximation in this method and make it suitable for a broader range of materials. It will be necessary to consider a couple of layers (≈ 4) to be able to compute the Josephson coupling between them. A multi-scale approach is required, where based on the pancake positions in the layers, the phase of the superconducting wave functions is computed. The relative phase difference determines the energy contribution due to the Josephson coupling which has to be integrated with the computation of the electromagnetic interaction.

Appendix A

Vortex state data compression

A.1 Introduction

We need to store the (three dimensional) positions of a set of particle-like vortices for many time steps to be able to post process the data at a later point. The z-position of a particle is determined by its layer, and this can easily be encoded efficiently. Thus, we have effectively sets of two-dimensional positions to deal with.

To store $N_T = 10000$ time-steps for a system with $N_v = 1000$ particles, each having $f = 2$ degrees of freedom, and using $B = 8$ byte per floating point number, we need $N_v N_T f B \approx 150$ Megabyte of disk space. It is desirable to reduce this number.

In general, it is not necessary to store the data with the same accuracy which is used in the computation (8 byte per floating point number), and for different investigations, different precision may be acceptable. Thus, we are looking for a compression scheme with an adjustable accuracy.

A.1.1 Test data

Figure A.1 shows four different sets of test data which are used to evaluate the compression algorithms. The first three sets are simulation results from runs with 598 vortices confined in a simulation cell of size 8.027×7.859 simulation units. We have taken 100 time steps out of much longer simulations, and every 10^{th} time step has been stored and plotted.

A.1.2 Absolute and relative error

In order to represent a real number $x \in \mathbb{R}$ we use an approximation $\tilde{x}$ which is in general not equal to x. Instead, there is a small deviation. The *absolute* error ϵ is

$$\epsilon(x) = |\tilde{x} - x| \tag{A.1}$$

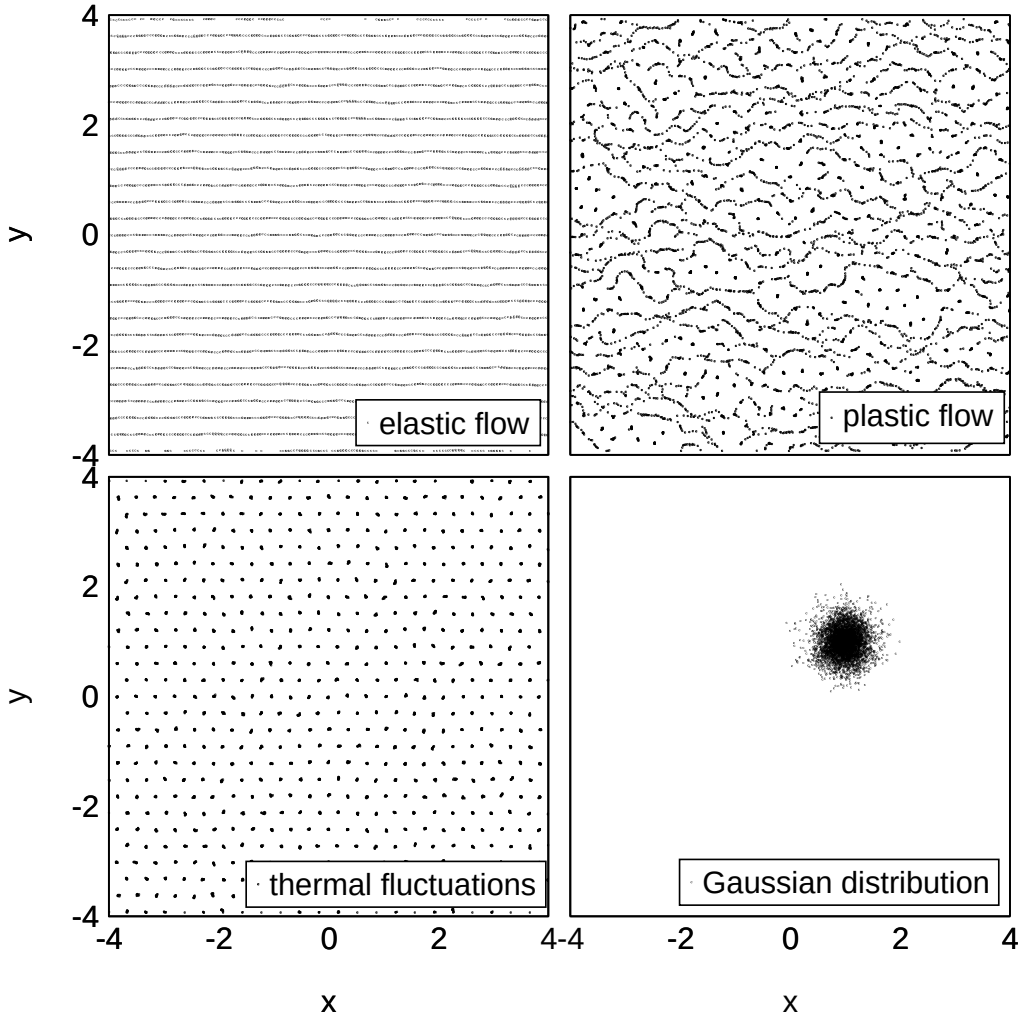

Figure A.1: The data used for the various compression approaches. Each run consists of 598 vortices, and 10 (out of 100) time steps have to be stored. The plots show the accumulation of vortex positions over the 10 time steps. The elastic (chapter 5) and plastic flow, and the thermal fluctuations (chapter 6) are realistic configurations. The Gaussian distribution of particles is only used to be able to compare our results with other works, and we have neglected the particle-particle interaction in this set.

and the *relative* error is

$$\frac{\epsilon(x)}{x} = \left|\frac{\tilde{x} - x}{x}\right|. \tag{A.2}$$

For the simulation data we are mainly interested in the absolute error: the range of possible numbers x and y is fixed to $x \in [-L_x/2, L_x/2]$ and $y \in [-L_y/2, L_y/2]$, where L_x and L_y are the length of the simulation cell, which is centred around the origin. Typical values for L_x and L_y are in the range of 1 to 100.

A.2 Compression methods

A.2.1 ASCII-files

The simplest approach to save the positions is to use a plain text file, and to write two-dimensional positions in clear text:

```
-3.931962 -2.322394
-3.443380 -2.375557
-3.917671 -2.629709 ...
```

This is very portable because no problems with conversion to Big or Little Endian format occur (see section A.2.2), and it is irrelevant how many bytes the system uses to represent a floating point number. However, such a data format needs 20 characters (*i.e.* 20 bytes) for each vortex position, *i.e.* 5 byte per floating point number with an error of $\approx 10^{-6}$. This is very inefficient because one byte is used to represent one out of only ten items (the digits `0` to `9`) although a byte can encode 256 items.

A.2.2 Binary files

An floating point number can be written to disk "as it is stored" in the computer. The number of bytes used for a floating point number is not fixed, and may vary for different platforms and compilers. Usually a `float` (in "C"-terminology) is a floating point number which is 4 byte long, and a `double` is 8 bytes long, and we assume this to be true in this section.

For `float`s, the relative error is $\approx 10^{-7}$, and this is sufficiently accurate for our purposes. By simply writing the binary numbers to a file, we can achieve a higher accuracy than writing ASCII-files, and need only 4 bytes per floating point number.

To be able to read and write data on different hardware architectures, one has to ensure that the bytes representing one floating point are written in the correct order: either as Big Endian (least significant byte last) or as Little Endian (least significant byte first). We found it most convenient to store data always as Little Endian and to convert to and from Big Endian on the fly while writing and reading files on Big Endian-based platforms.

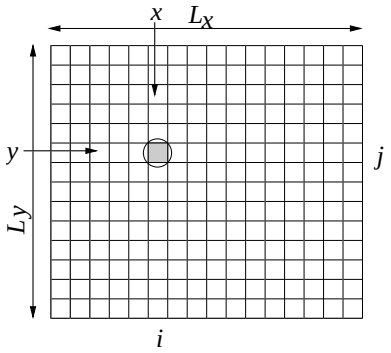

Figure A.2: Demonstrating the integer method and the resulting error. Instead of storing a particle's x and y position as floating point numbers, we store two indices i and j for the box it is located in. Error estimation: When reconstructing particle positions from indices, we always assume the particle was in the middle of its associated box. In the worst case it was at a corner of the box. Thus, the error is $E = \sqrt{r_x^2 + r_y^2}$, where r_x and r_y are half the length of a box in the x and y direction, respectively.

A.2.3 Integer method

A 4-byte long floating point number uses 24 bits to store the mantissa (in the binary system), and (nearly) 8 bits to encode the exponent.[1] The exponent is useful to extend the range of valid floating point numbers. This however, is for our data not advantageous, *i.e.* 8 of the 32 bits are not efficiently used, and this can be exploited.

The idea is to map all floating point numbers $\in [a, b]$ to integer numbers $[0, 2^n - 1]$, where $n \approx 24$ to obtain a comparable accuracy as for 4-byte floats. Then these integers are stored tightly following each other in a file, *i.e.* every integer occupies exactly n bits (which requires the implementation of special input and output routines). The absolute error for this approach (in one dimension) is $\epsilon = |b - a|/2^{n+1}$.

Using 24 bits, *i.e.* $n = 24$, this approach reduces storage requirements by $\frac{1}{4}$ in comparison to storing 4-byte `floats`, while not reducing the accuracy. This *lossless* compression is possible because the data is bounded to lie within the simulation cell.

The absolute error ϵ when using n_x and n_y bits to discretise the x and y direction can be estimated as follows (see figure A.2). For n_x bits we have 2^{n_x} boxes, and thus each box has a length $l_x = 2r_x = L_x/2^{n_x}$. As shown in figure A.2 the maximum error when reconstructing the position from the integer data is

$$E = \sqrt{r_x^2 + r_y^2} \;=\; \sqrt{\left(\frac{L_x}{2 \cdot 2^{n_x}}\right)^2 + \left(\frac{L_y}{2 \cdot 2^{n_y}}\right)^2} = \sqrt{2^{(-2n_x-2)} L_x^2 + 2^{(-2n_y-2)} L_y^2}. \tag{A.3}$$

[1] Using `gcc version egcs-2.91.66 19990314 (egcs-1.1.2 release)`.

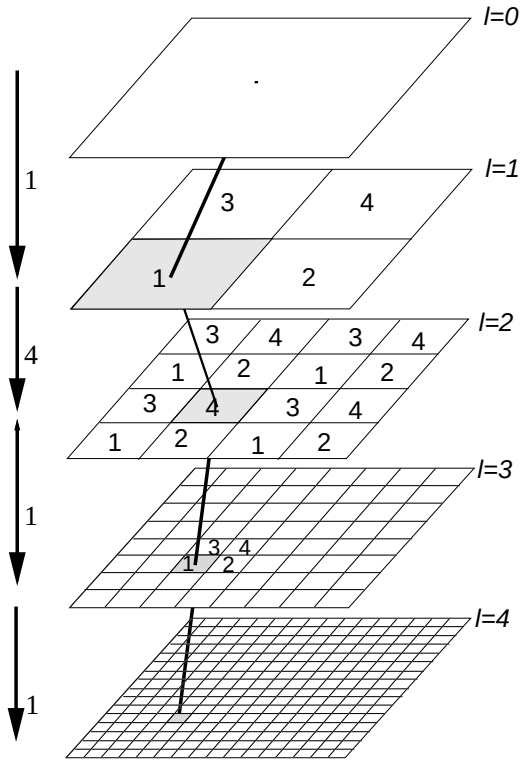

Figure A.3: The path $p = 1411$ is used to point to the shaded box in the lowest level $l = 4$ of the quad-tree. The figure demonstrates how the path grows: in level 1 it is $p = 1$, in level 2 $p = 14$, in level 3 $p = 141$, and in level 4 $p = 1411$ (not explicitly shown).

A.2.4 Tree method

A.2.4.1 Quad-tree method

We now try to exploit spatial and temporal coherence in our data. Figure A.3 introduces the quad-tree. Each node has four children, which are the quadrants of the node. These are labelled 1, 2, 3, and 4. The root-node (at level $l = 0$) is the simulation cell. The boxes in the deepest level (here $l = 4$) are the leaves of the quad-tree, which determine the accuracy.

We associate the x- and y-position of a particle with the centre of a leaf. Instead of storing the indices i and j to label leaves (as for the integer method), we encode leaves with a *path* through the quad-tree. In figure A.3, starting from the root-node at level $l = 0$ we add a 1 to the path to branch into the lower left quarter of the current box in the next level ($l = 1$). Now we add a 4 to the path because in the next level ($l = 2$) we branch into the upper right quarter of the current box. Thus the path grows, until — in the example in figure A.3 at level $l = 4$ — the leaves are reached. The final path is 1411. This describes the position of one particle. Paths for a quad-tree with 24 levels look like this:

```
123333333343421121121223
141111141423443124112134
141111311344321224443212 ...
```

An upper bound for the absolute error occurring when particle positions are approximated with box positions can be estimated in the same way as for the integer method, since the deepest level corresponds to figure A.2. To obtain the same accuracy as for the integer method we need as many levels in the tree as bits for the integer method (assuming $L_x = L_y$ and n_x=n_y for simplicity). For the integer method we need two numbers with n bits to encode one particle's position, whereas for the quad-tree method we need one path with n-levels to encode a particle's position. Since one level needs two bits to be stored (to code 4 possibilities), both methods have exactly the same compression and accuracy.

A.2.4.2 Spatial coherence

Sorting the paths shows that particles can be "close" too each other in the quad-tree description of their positions:

```
11111112321224314133431 3
11111144241234444434231 2
11111221413432341332113 1 ...
```

These data can be compressed by not storing the first k identical levels in the paths for two subsequent particles in the sorted list of paths. In the example shown above, this would eliminate "111111" for the second particle because it is identical with the preceeding particle ($k = 6$). Accordingly, we would not store "11111" for the third particle ($k = 5$).

However, somewhere we have to store k to be able to reconstruct the complete path at a later point. By sorting the paths, we also lose the identity of particles. If we wish to be able to recover which particle went where, *i.e.* to retain the particle's identity, we have to store a particle number together with each path.

Sorting the paths of the quad tree is equivalent to ordering particles along space-filling z-curves in the simulation cell (*Pilkington and Baden*, 1996). In the picture of z-curves, the compression resulting from not storing leading identical levels for subsequent particles, corresponds to storing the relative displacement between two particles next two each other along the z-curve.

The spatial coherence appears to have great potential when the particles cluster in certain places, as in many astronomy and chemistry simulations, and when it doesn't matter which particle goes where. Unfortunately, vortices repel each other and thus distribute as uniformly as possible, and we would like to keep track of paths of individual particles.

A.2.4.3 Temporal coherence

The simulation data describe particle positions as a function of time. Now we address the temporal correlation between the positions in two subsequent time steps. We first compute the relative displacement of each particle with respect to its position in the previous time-step. We then create a quad-tree to describe the *displacements*. Finally, we sort and shorten this quad-tree as described in section A.2.4.2.

The underlying idea is that the displacements of a set of vortices are less widely spread than the (uniformly distributed) particle positions if the positions are stored sufficiently frequently.

Periodic boundary conditions will result in huge jumps of a particle once it moves across the simulation cell border. These jumps will be stored inefficiently, which can be overcome if we — in such cases — store their new position outside the simulation cell, and apply periodic boundary conditions when reading the data back from the file.

A.3 Results

Table A.1 shows file sizes and compression ratios for the described methods. The data used are taken from the elastically moving system as shown in figure A.1 and investigated in chapter 5. We have used 24 bits for the integer method, and 24 levels for the quad-tree method. The obtained compression is thus lossless with respect to storing binary floats.

As expected, the integer method achieves a compression of $4/3 \approx 1.33$ as explained in section A.2.3 on page 122, and so does the simple quad-tree method (section A.2.4.1).

The quad-tree method using spatial coherence (section A.2.4.2) performs worse than the simple quad-tree. This is because we have to add 10 bit to every path to keep the particle's identity, but we cannot gain much by sorting the quad-tree paths and cutting of the first identical digits because spatial correlation is poor for the vortex system with it's homogenous vortex distribution. (This method performs much better on the normally distributed particle positions as shown in figure A.1 on page 120 because there is more spacial correlation.)

The data can be compressed losslessly by nearly a factor of two using the tree method exploiting the temporal coherence of the system (section A.2.4.3).

Table A.2 shows the same data as table A.1 but for lossy compression: only 14 bits and levels have been used to store the data. For 14 bits and $L_x = L_y$, we find

comp. ratio	bytes per position	bytes per pos. (gzipped)	method
1.0	8.00	6.67	binary floats (2×4 byte)
1.1	7.02	6.96	quad-tree, spatial coherence
1.3	6.00	6.00	quad-tree
1.3	6.00	5.73	integer method
1.9	4.23	4.23	quad-tree, temporal coherence

Table A.1: Comparison of different compression techniques for elastic flow data using 24 bits for the integer method and 24 levels for the tree methods. The first column shows the compression ratio in comparison to storing binary floating point numbers. The second column shows the (average) number of bytes required to encode one particle's position. The third column shows the number of bytes required after compressing further the compressed data file using `gzip`. The last column shows the employed compression method.

comp. ratio	bytes per position	bytes per pos. (gzipped)	method
1.0	8.00	6.67	binary floats (2×4 byte)
1.8	4.40	4.35	quad-tree, spatial coherence
2.3	3.51	3.51	quad-tree
2.3	3.51	3.47	integer method
4.3	1.88	1.88	quad-tree, temporal coherence

Table A.2: Same as table A.1 but with only 14 bits/levels.

using (A.3) for the error $E \approx 4 \cdot 10^{-5} L_x$ which is acceptable for most simulations. This yields compression rates as high as 4 in comparison to using binary floats.

In both, table A.1 and table A.2, the second column shows the number of required bytes per position after the compressed data file has been compressed using gzip. Generally, the gzipped-file is slightly smaller, except for the temporal coherence quad-tree method where it is actually marginally larger (not visible in tables). This indicates that we are close to the maximum compression of these data.[2]

A.3.1 Dependence on bits/levels

Figure A.4 shows how the achieved compression varies as a function of number of bits/levels used. For comparison we have shown the 8 bytes per position that are required for storing binary floats. For more than 16 bits all other four curves have the same slope, albeit different offsets. The curve for the integer method and the

[2]Gzip operates with a dictionary which is based on characters (*i.e.* 8 bit units). To be sure we use gzip most efficiently, we have also written our path-data as ASCII-text instead of closely packed bits before using gzip, but no better compression rates were achieved.

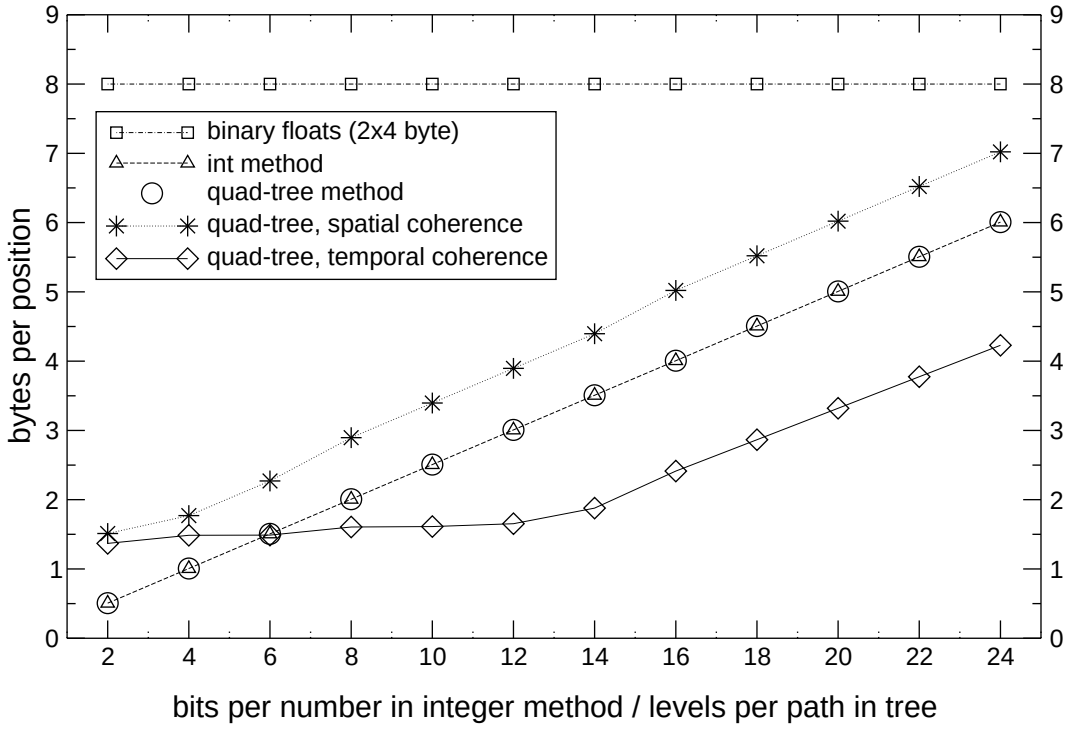

Figure A.4: Required number of bytes for coding one position for different accuracies. The best compression is achieved using the temporal coherence quad tree method. The compressed data is taken from an elastically moving system with 598 particles.

simple quad tree coincide as expected. The best compression is obtained with the temporal coherence quad tree method, which — for less than 10 levels — approaches a constant value of ≈ 1.5 bytes per position. This is due to the extra information included in the data file which allows to undo the sorting of the paths (this actually requires 10 bit per path for 598 particles), and starts to dominate for less than 10 levels. Using the spatial coherence quad tree method is actually worse than storing the tree directly. This, again, is due to the extra information about the order of the particles that has to be included.

At least for data from elastically moving systems the temporal coherence quad tree is the best compression method for more than 6 bits resolution, and less than 6 bit is not accurate enough to be useful.

A.3.2 Dependence on simulation data

Figure A.5 compares the compression properties of the temporal coherence quad tree method with the integer method (gzipped) and with storing floats (gzipped). With the temporal coherence quad tree method, the elastically moving system compresses best, thermal fluctuations compress well, and plastic flow has the smallest compression rate. However, in comparison to the gzipped float file with ≈ 7.4 bytes

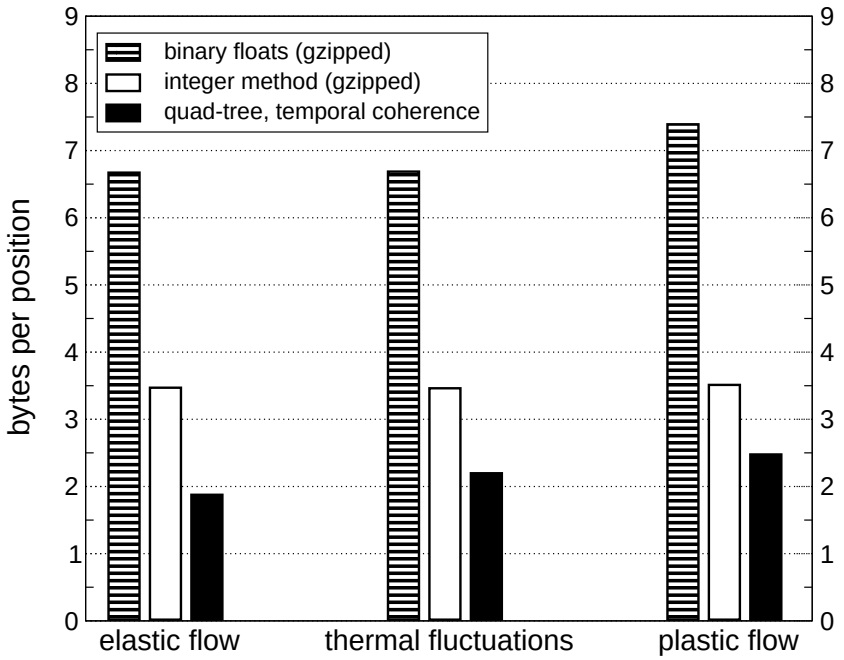

Figure A.5: Required number of bytes per position for compression of qualitatively different data. Shown are results for gzipped binary floats (2×4 bytes), the gzipped integer method (2×14 bits), and the temporal coherence quad-tree method (14 levels). Whereas the first two shrink by approximately 20% when being gzipped, the temporal coherence quad tree results do not shrink at all.

per position, the temporal coherence quad-tree method achieves a reduction in file size by a factor of three for plastic flow. Averaged over the three different kinds of data, the temporal coherence quad-tree method reduces the file size by about a factor of three in comparison to the (more accurate) float file, and by a factor of ≈ 1.5 in comparison to (gzipped) integer method files (of same accuracy).

A.3.3 Comparison with other works

Similar works (*Yang et al.*, 1999, *Omeltchenko et al.*, 2000) have employed the technique of sorting quad-trees (or oct-trees for three-dimensional systems) to compress data. In contrast to their simulations we need to keep track of our particles, and it is not likely that our particles cluster in some places of the simulation cell. Both groups compare their results for lossy compression with storing double floats (each requiring 8 byte) and achieve compression ratios of about a factor ten. The accepted error, for example in the work of *Omeltchenko et al.* (2000), is comparable to using 14 levels for our system (for a system size of $\approx 500 - 1000$ vortices).

Our temporal coherence quad-tree method needs ≈ 2.1 byte per particle position (averaged over different data types, figure A.5) using 14 levels. Thus, in comparison to using twice 8 byte per position, we get a compression of $16/2.1 \approx 7.6$. However, in

contrast to the order-of-magnitude compression by *Omeltchenko et al.*, this contains the order of the particles. Dropping the order of the objects, we only need ≈ 0.85 bytes per particle (because we need 10 bit = 1.25 byte to store the ID of a particle for the chosen system size of 598), and get a compression of $16/0.85 \approx 19$. While we only store positions, *Omeltchenko et al.* also store velocities which are not bounded and might compress worse. It is also possible that exploiting temporal coherence improves the compression.

A.4 Summary

We have developed a compression technique by extending quad-tree methods and exploiting the temporal coherence we find in our simulation data. In comparison to storing data with 4-byte floating point numbers, our method achieves a lossless compression of a factor ≈ 2, and for a lower but practically acceptable accuracy (14 levels), it reaches a compression of ≈ 4. Our method for uniformly distributed particle positions compares well with similar implementations.

Appendix B

Derivation of $\mathcal{U}$

We show how (6.19) can be transformed into (6.20) on page 89. We start with the Fourier representation of $U(\mathbf{r}, n)$, and show by taking the inverse Fourier transform the equivalence to (6.4) for $z = 0$. This provides several expressions that we need in order to perform the sum

$$\mathcal{U}(\mathbf{r}) \equiv \sum_{n \neq 0} U(\mathbf{r}, n). \tag{B.1}$$

The Fourier representation of $U(\mathbf{r}, n)$ is (*Feigel'man et al.*, 1990)

$$U(\mathbf{R}, n) = 4\pi\epsilon_0 s^2 \int \frac{\mathrm{d}^2 q}{(2\pi)^2} \frac{\mathrm{d}k}{2\pi} \; \frac{(q^2 + k^2) e^{ikns} e^{i\mathbf{q}\cdot\mathbf{R}}}{q^2(\lambda^{-2} + q^2 + k^2)} \tag{B.2}$$

where $\mathbf{q}$ is the in-layer variable and k is the out-of-layer variable in Fourier space. We write the z-position as $z = ns$ where n is an integer and s is the layer spacing.

In-plane interaction

We start with the in-plane interactions, $n = 0$

$$\begin{aligned} U(\mathbf{R}, 0) &= 4\pi\epsilon_0 s^2 \int \frac{\mathrm{d}^2 q}{(2\pi)^2} \frac{\mathrm{d}k}{2\pi} \; \frac{(q^2 + k^2) e^{i\mathbf{q}\cdot\mathbf{R}}}{q^2(\lambda^{-2} + q^2 + k^2)} \\ &= 4\pi\epsilon_0 s^2 \int \frac{\mathrm{d}^2 q}{(2\pi)^2} \; \frac{1}{q^2} e^{i\mathbf{q}\cdot\mathbf{R}} \underbrace{\int_{-\pi/s}^{\pi/s} \frac{\mathrm{d}k}{2\pi} \; \frac{q^2 + k^2}{\lambda^{-2} + q^2 + k^2}}_{I_1(q)} \end{aligned}$$

We simplify $I_1(q)$

$$\begin{aligned}
I_1(q) &= \int_{-\pi/s}^{\pi/s} \frac{\mathrm{d}k}{2\pi} \quad \frac{q^2+k^2}{\lambda^{-2}+q^2+k^2} \\
&= \int_{-\pi/s}^{\pi/s} \frac{\mathrm{d}k}{2\pi} \quad 1 - \frac{-\lambda^{-2}}{\lambda^{-2}+q^2+k^2} \\
&= \frac{1}{s} - \int_{-\pi/s}^{\pi/s} \frac{\mathrm{d}k}{2\pi} \quad \frac{-\lambda^{-2}}{\lambda^{-2}+q^2+k^2} \\
&\qquad \text{use} \quad k = x\sqrt{\lambda^{-2}+q^2} \\
&= \frac{1}{s} - \frac{\lambda^{-2}}{2\pi\sqrt{\lambda^{-2}+q^2}} \int_{-\pi/s}^{\pi/s} \mathrm{d}x \quad \frac{1}{1+x^2} \\
&\qquad \text{note that } \frac{\pi}{s} \approx 10^9 \\
&\approx \frac{1}{s} - \frac{\lambda^{-2}}{2\pi\sqrt{\lambda^{-2}+q^2}} \underbrace{\int_{-\infty}^{\infty} \mathrm{d}x \quad \frac{1}{1+x^2}}_{\pi} \\
&= \frac{1}{s} - \frac{1}{2\lambda\sqrt{1+\lambda^2 q^2}}.
\end{aligned} \tag{B.3}$$

Thus,

$$\begin{aligned}
&U(\mathbf{R},0) \\
&= 4\pi\epsilon_0 s^2 \int \frac{\mathrm{d}^2 q}{(2\pi)^2} \quad \frac{1}{q^2} e^{i\mathbf{q}\cdot\mathbf{R}} \left(\frac{1}{s} - \frac{1}{2\lambda\sqrt{1+\lambda^2 q^2}} \right) \\
&= 4\pi\epsilon_0 s \underbrace{\int \frac{\mathrm{d}^2 q}{(2\pi)^2} \quad \frac{1}{q^2} e^{i\mathbf{q}\cdot\mathbf{R}}}_{\frac{1}{2\pi}\ln\left(\frac{L}{R}\right)} \\
&\qquad - \frac{4\pi\epsilon_0 s^2}{\lambda} \underbrace{\int \frac{\mathrm{d}^2 q}{(2\pi)^2} \quad \frac{1}{q^2\sqrt{1+\lambda^2 q^2}} e^{i\mathbf{q}\cdot\mathbf{R}}}_{I_2(\mathbf{R})}
\end{aligned} \tag{B.4}$$

We simplify $I_2(\mathbf{R})$

$$\begin{aligned} I_2(\mathbf{R}) &= \int \frac{\mathrm{d}^2 q}{(2\pi)^2} \ \frac{1}{q^2\sqrt{1+\lambda^2 q^2}} e^{i\mathbf{q}\cdot\mathbf{R}} \\ &= \frac{1}{(2\pi)^2} \int_0^\infty q\mathrm{d}q \int_0^{2\pi} \mathrm{d}\theta \ \frac{1}{q^2\sqrt{1+\lambda^2 q^2}} e^{iqR\cos(\theta)} \\ &= \frac{1}{2\pi} \int_0^\infty \mathrm{d}q \ \frac{1}{q\sqrt{1+\lambda^2 q^2}} \underbrace{\frac{1}{2\pi} \int_0^{2\pi} \mathrm{d}\theta e^{iqR\cos(\theta)}}_{J_0(qR)} \end{aligned} \tag{B.5}$$

where $J_n(qR)$ is the Bessel function of first kind and n-th order, with the property

$$J_0(x) = \int_x^\infty \mathrm{d}y \ \ J_1(y) \tag{B.6}$$

and therefore

$$J_0(qR) = \int_{qR}^\infty \mathrm{d}y \ \ J_1(y) \overset{x=\frac{y}{q}}{=} \int_R^\infty q\,\mathrm{d}x \ \ J_1(xq) = q\int_R^\infty \mathrm{d}x \ \ J_1(xq) \tag{B.7}$$

$$\begin{aligned} I_2(\mathbf{R}) &= \frac{1}{2\pi} \int_0^\infty \mathrm{d}q \ \frac{1}{q\sqrt{1+\lambda^2 q^2}} \ q\int_R^\infty \mathrm{d}x \ \ J_1(xq) \\ &= \frac{1}{2\pi} \int_R^\infty \mathrm{d}x \int_0^\infty \mathrm{d}q \ \frac{J_1(xq)}{\sqrt{1+\lambda^2 q^2}} \\ &= \frac{1}{2\pi\lambda} \int_R^\infty \mathrm{d}x \int_0^\infty \mathrm{d}q \ \frac{J_1(xq)}{\sqrt{\lambda^{-2}+q^2}} \end{aligned} \tag{B.8}$$

We use the identity (*Watson*, 1944)

$$\int_0^\infty \mathrm{d}q \ \frac{J_1(xq)}{\sqrt{\lambda^{-2}+q^2}} = I_{\frac{1}{2}}\left(\frac{x}{2\lambda}\right) K_{\frac{1}{2}}\left(\frac{x}{2\lambda}\right) \tag{B.9}$$

where $I_n(x)$ is the modified Bessel function of first kind and n-th order and $K_n(x)$ is the modified Bessel function of second kind and n-th order. We use the special

properties (*Gradshteyn and Ryzhik*, 1994) of $I_{\frac{1}{2}}$ and $K_{\frac{1}{2}}$

$$\begin{aligned} I_{\frac{1}{2}}\left(\frac{x}{2}\right) &= \frac{2}{\sqrt{\pi x}}\sinh\left(\frac{x}{2}\right) = \frac{2}{\sqrt{\pi x}}\frac{1}{2}\left(e^{\frac{x}{2}} - e^{-\frac{x}{2}}\right) \\ K_{\frac{1}{2}}\left(\frac{x}{2}\right) &= \sqrt{\frac{\pi}{x}}e^{-\frac{x}{2}}, \\ I_{\frac{1}{2}}\left(\frac{x}{2}\right)K_{\frac{1}{2}}\left(\frac{x}{2}\right) &= \frac{1}{x}\left(1 - e^{-x}\right). \end{aligned} \tag{B.10}$$

It follows that

$$\begin{aligned} I_2(\mathbf{R}) &= \frac{1}{2\pi\lambda}\int_R^\infty \mathrm{d}x \;\; \frac{\lambda}{x}\left(1 - e^{-\frac{x}{\lambda}}\right) \\ &= \frac{1}{2\pi}\int_R^\infty \mathrm{d}x \;\; \frac{1}{x} \;\; - \;\; \frac{1}{2\pi}\int_R^\infty \mathrm{d}x \;\; \frac{e^{-\frac{x}{\lambda}}}{x} \\ &= \frac{1}{2\pi}\ln\left(\frac{L}{R}\right) \;\; + \;\; \frac{1}{2\pi}\mathrm{Ei}\left(-\frac{R}{\lambda}\right), \end{aligned} \tag{B.11}$$

where L is the system size, and $\mathrm{Ei}(x)$ the exponential-integral function

$$\mathrm{Ei}(-x) = -\int_x^\infty \mathrm{d}x' \;\; \frac{\exp(-x')}{x'}. \tag{B.12}$$

We continue from (B.4) and write

$$U(\mathbf{R},0) = 2\epsilon_0 s\left[\ln\left(\frac{L}{R}\right) - \frac{s}{2\lambda}\ln\left(\frac{L}{R}\right) - \frac{s}{2\lambda}\mathrm{Ei}\left(-\frac{R}{\lambda}\right)\right] \tag{B.13}$$

which reproduces (6.4).

Derivation of $\mathcal{U}$

We solve the sum in (B.1):

$$
\begin{aligned}
& \sum_{n\neq 0} U(\mathbf{R},n) \\
\overset{(B.2)}{=}\quad & \sum_{n\neq 0} 4\pi\epsilon_0 s^2 \int \frac{\mathrm{d}^2q}{(2\pi)^2}\frac{\mathrm{d}k}{2\pi}\ \ \frac{(q^2+k^2)e^{ikns}e^{i\mathbf{q}\cdot\mathbf{R}}}{q^2(\lambda^{-2}+q^2+k^2)} \\
=\quad & 4\pi\epsilon_0 s^2 \int \frac{\mathrm{d}^2q}{(2\pi)^2}\frac{\mathrm{d}k}{2\pi}\ \ \frac{q^2+k^2}{q^2(\lambda^{-2}+q^2+k^2)} e^{i\mathbf{q}\cdot\mathbf{R}} \underbrace{\sum_{n\neq 0} e^{ikns}}_{\frac{2\pi}{s}\delta(k)-1} \\
=\quad & 4\pi\epsilon_0 s^2 \int \frac{\mathrm{d}^2q}{(2\pi)^2}\ \ e^{i\mathbf{q}\cdot\mathbf{R}}\left[\frac{q^2}{q^2(\lambda^{-2}+q^2)}\frac{1}{s} - \ \frac{1}{q^2}\underbrace{\int\frac{\mathrm{d}k}{2\pi}\frac{q^2+k^2}{\lambda^{-2}+q^2+k^2}}_{\overset{(B.3)}{=} I_1(q)}\right] \\
\overset{(B.3)}{=}\quad & 4\pi\epsilon_0 s \int \frac{\mathrm{d}^2q}{(2\pi)^2}\ \ e^{i\mathbf{q}\cdot\mathbf{R}}\left[\frac{1}{\lambda^{-2}+q^2} - \frac{s}{q^2}\left(\frac{1}{s}-\frac{1}{2\lambda\sqrt{1+\lambda^2q^2}}\right)\right] \\
=\quad & 4\pi\epsilon_0 s \int \frac{\mathrm{d}^2q}{(2\pi)^2}\ \ e^{i\mathbf{q}\cdot\mathbf{R}}\left[\frac{1}{\lambda^{-2}+q^2}-\frac{1}{q^2}\right] + \frac{4\pi\epsilon_0 s^2}{2\lambda}\underbrace{\int\frac{\mathrm{d}^2q}{(2\pi)^2}\frac{e^{i\mathbf{q}\cdot\mathbf{R}}}{q^2\sqrt{1+\lambda^2q^2}}}_{\overset{(B.5)}{=} I_2(\mathbf{R})} \\
\overset{(B.11)}{=}\quad & 4\pi\epsilon_0 s\underbrace{\int \frac{\mathrm{d}^2q}{(2\pi)^2}\ \ e^{i\mathbf{q}\cdot\mathbf{R}}\left[\frac{1}{\lambda^{-2}+q^2}-\frac{1}{q^2}\right]}_{\frac{1}{2\pi}K_0\left(\frac{R}{\lambda}\right)} + \frac{2\epsilon_0 s^2}{2\lambda}\left[\ln\left(\frac{L}{R}\right)+\mathrm{Ei}\left(-\frac{R}{\lambda}\right)\right] \\
=\quad & 2\epsilon_0 s K_0\left(\frac{R}{\lambda}\right) - 4\pi\epsilon_0 s\underbrace{\int\frac{\mathrm{d}^2q}{(2\pi)^2}\frac{e^{i\mathbf{q}\cdot\mathbf{R}}}{q^2}}_{\frac{1}{2\pi}\ln\left(\frac{L}{R}\right)} + \frac{2\epsilon_0 s^2}{2\lambda}\left[\ln\left(\frac{L}{R}\right)+\mathrm{Ei}\left(-\frac{R}{\lambda}\right)\right] \\
=\quad & 2\epsilon_0 s\left[K_0\left(\frac{R}{\lambda}\right) - \ln\left(\frac{L}{R}\right) + \frac{s}{2\lambda}\left[\ln\left(\frac{L}{R}\right)+\mathrm{Ei}\left(-\frac{R}{\lambda}\right)\right]\right] \\
=\quad & 2\epsilon_0 s\left[K_0\left(\frac{R}{\lambda}\right) - \left(1-\frac{s}{2\lambda}\right)\ln\left(\frac{L}{R}\right) + \frac{s}{2\lambda}\mathrm{Ei}\left(-\frac{R}{\lambda}\right)\right] \\
\overset{(B.13)}{=}\quad & 2\epsilon_0 s K_0\left(\frac{R}{\lambda}\right) - U(\mathbf{R},0) = \mathcal{U}(\mathbf{R}).
\end{aligned}
$$

Appendix C

Notes on discrete Fourier transforms

To complement the information given in chapter 6, we investigate the difference between the analytical Fourier transform and the discrete version in its typical form (*Press et al.*, 1995, *Frigo and Johnson*, 1998). We extend our analysis from discrete Fourier transforms to discrete convolutions using Fourier transforms.

The discrete Fourier transform

Per definition (6.30)

$$\hat{f}(k) = \int_{-\infty}^{\infty} \mathrm{d}x \quad f(x) \exp(-\sqrt{-1}kx). \tag{C.1}$$

The discrete Fourier transform (DFT) can only be taken over a certain interval of length X, so the first alteration of $\hat{f}(k)$ is

$$\hat{f}_1(k) = \int_{0}^{X} \mathrm{d}x \quad f(x) \exp(-\sqrt{-1}kx). \tag{C.2}$$

The data, $f(x)$, are only available at discrete points, so we approximate the integral with a sum. We use

$$x_i = i\Delta x \quad \text{with} \quad i = 0, 1, \ldots, N-1 \qquad \Delta x = \frac{X}{N} \tag{C.3}$$

and N is the even number of data for f.

$$\hat{f}_2(k) = \sum_{i=0}^{N-1} \Delta x \quad f(x_i) \exp(-\sqrt{-1}kx_i). \tag{C.4}$$

Eventually, we compute $\hat{f}(k)$ only at discrete points k_j

$$\hat{f}_3(k_j) = \sum_{i=0}^{N-1} \Delta x \quad f(x_i) \exp(-\sqrt{-1} k_j x_i) \tag{C.5}$$

where

$$k_j = j\Delta k \qquad k = 0, 1, \ldots, N-1 \tag{C.6}$$

with

$$\Delta k = \frac{2\pi}{X} \qquad \text{and} \qquad \Delta x = \frac{2\pi}{K}. \tag{C.7}$$

K is the range of the data in Fourier-space. The exponent in (C.5) can be written as

$$k_j x_i = j\ \Delta k\ \ i\ \Delta x = j\frac{2\pi}{X} i\frac{X}{N} = ij\frac{2\pi}{N}. \tag{C.8}$$

Thus, we rewrite (C.5) using $f_i = f(x_i)$

$$\frac{\hat{f}_3(k_j)}{\Delta x} = \hat{f}_j \equiv \sum_{i=0}^{N-1} \quad f_i \exp\left(-\sqrt{-1}\frac{ij2\pi}{N}\right) \tag{C.9}$$

and define $\hat{f}_j$ to be the discrete Fourier transform of N points f_i. This is the expression that is evaluated in the numeric computation. The spacing Δx of the data points f_i can be excluded from the sum in (C.5) and that makes $\hat{f}_j$ dimensionless (assuming the f_i are dimensionless).

To formalise this, we introduce

$$\mathcal{F}_{\mathrm{DP}} = \frac{1}{\Delta x}\mathcal{F} \tag{C.10}$$

which is the Fourier operator for a Discrete set of Points, f_i, as defined in (C.9), and $\mathcal{F}$ is defined in (6.30).
The inverse Fourier transform for a discrete set of points is defined as

$$f_i = \sum_{j=0}^{N-1} \hat{f}_j \exp\left(\sqrt{-1}\frac{ij2\pi}{N}\right) \tag{C.11}$$

and we introduce the inverse Fourier operator for a discrete set of points

$$\mathcal{F}_{\mathrm{DP}}^{-1} = \frac{2\pi}{\Delta k}\mathcal{F}^{-1}. \tag{C.12}$$

The division by Δk is in analogy to dividing (C.10) by Δx and the reason for the factor 2π can be seen by comparing (C.11) with $\mathcal{F}^{-1}$ as defined in (6.31).

While composition of the forward and the backward Fourier transform $\mathcal{F}^{-1} \circ \mathcal{F}$ is an identity operator, *i.e.* $\mathcal{F}$ is self-inverse, the same is not true for

$$\mathcal{F}_{\mathrm{DP}}^{-1} \circ \mathcal{F}_{\mathrm{DP}} = \frac{2\pi}{\Delta k}\frac{1}{\Delta x} = N. \tag{C.13}$$

The discrete convolution in Fourier space

The relation (C.10) is important for the computation of (6.35) as we compute $\mathcal{F}_{\mathrm{DP}}\{\rho(\mathbf{r})\}$ and multiply it pointwise with $\mathcal{F}\{\mathcal{U}(\mathbf{r})\}$. To be consistent, we divide the analytical transform $\mathcal{F}\{\mathcal{U}(\mathbf{r})\}$ by Δx.

A similar issue arises for the result of the convolution (6.35):

$$\begin{aligned}
V_{\mathrm{MF,DP}}(\mathbf{r}) &= \mathcal{F}_{\mathrm{DP}}^{-1}\left\{\mathcal{F}_{\mathrm{DP}}\{\rho(\mathbf{r})\}\frac{\mathcal{F}\{\mathcal{U}(\mathbf{r})\}}{\Delta x}\right\} && \text{(C.14)}\\
&= \frac{2\pi}{\Delta k}\mathcal{F}^{-1}\left\{\frac{1}{\Delta x}\mathcal{F}\{\rho(\mathbf{r})\}\frac{\mathcal{F}\{\mathcal{U}(\mathbf{r})\}}{\Delta x}\right\} && \text{(C.15)}\\
&= \frac{2\pi}{\Delta k}\frac{1}{\Delta x}\frac{1}{\Delta x}\mathcal{F}^{-1}\left\{\mathcal{F}\{\rho(\mathbf{r})\}\mathcal{F}\{\mathcal{U}(\mathbf{r})\}\right\} && \text{(C.16)}\\
&\overset{(C.8)}{=} \frac{N}{\Delta x}\mathcal{F}^{-1}\left\{\mathcal{F}\{\rho(\mathbf{r})\}\mathcal{F}\{\mathcal{U}(\mathbf{r})\}\right\} && \text{(C.17)}\\
&\overset{(6.33)}{=} \frac{N}{\Delta x}V_{\mathrm{MF}}(\mathbf{r}) && \text{(C.18)}\\
& && \text{(C.19)}
\end{aligned}$$

Therefore, the convolution data, $V_{\mathrm{MF,DP}}$, obtained using the discrete Fourier transforms for a set of points has to be scaled by $\frac{\Delta x}{N}$ to get the required V_{MF}. In two dimensions the scaling factor is $\frac{\Delta x}{N_x}\frac{\Delta y}{N_y}$.

Implementation

We use the libraries of the "Fastest Fourier Transform in the West" (FFTW[1]). The algorithm (*Frigo and Johnson*, 1998) is self-optimising and one of the fastest Fast Fourier Transform implementations available.

[1]FFTW is available at `http://www.fftw.org`.

Bibliography

Abrikosov AA. On the magnetic properties of superconductors of the second group. *Soviet Physics–JETP*, **5**, 1174–1182 (1957).

Allen MP and Tildesley DJ. *Computer Simulations of Liquids*. Clarendon Press, Oxford (1989).

Andrei EY, Deville G, Glattli DC, Willimas FIB, Paris E and Etienne B. Observation of a magnetically induced wigner solid. *Physical Review Letters*, **60**, 2765–2768 (1988).

Aranson I and Vinokur V. Surface instabilities and vortex transport in current-carrying superconductors. *Physical Review B*, **57**, 3073–3083 (1998).

Aranson IS, Scheidl S and Vinokur VM. Non-equilibrium dislocation dynamics and instability of driven vortex lattices in two dimensions. *Physical Review B*, **58**, 14541–14547 (1998).

Artemenko SN and Kruglov AN. Structure of 2d vortex in a layered high-T_c superconductor. *Phys. Lett. A*, **143**, 485–488 (1990).

Balents L, Marchetti MC and Radzihovsky L. Comment on "moving glass phase of driven lattices". *Physical Review Letters*, **78**, 751 (1997).

Balents L, Marchetti MC and Radzihovsky L. Nonequilibrium steady states of driven periodic media. *Physical Review B*, **57**, 7705–7739 (1998).

Barber CB, Dobkin DP and Huhdanpaa H. The quickhull algorithm for convex hulls. *ACM Transactions on Mathematical Software*, **22**, 469–483 (1996).

Bardeen J, Cooper LN and Schrieffer JR. Theory of superconductivity. *Phys. Rev.*, **108**, 1175–1204 (1957).

Bardeen J and Stephen MJ. Theory of the motion of vortices in superconductors. *Phys. Rev.*, **140**, A1197–A1207 (1965).

Bednorz JG and Müller KA. Possible high T_c superconductivity in the Ba-La-Cu-O system. *Z. Physik B*, **64**, 189 (1986).

Berman CL and Greengard L. A renormalization method for the evaluation of lattice sums. *J. Math. Phys.*, **35** (1994).

Bhattacharya S and Higgins MJ. Dynamics of a disordered flux line lattice. *Physical Review Letters*, **70**, 2617–2620 (1993).

Blatter G, Feigel'man MV, Geshkenbein VB, Larkin AI and Vinokur V. Vortices in high-temperature superconductors. *Reviews of Modern Physics*, **66**, 1125–1388 (1994).

Blatter G, Geshkenbein V, Larkin A and Nordborg H. Low-field phase diagram of layered superconductors: The role of electromagnetic coupling. *Physical Review B*, **54**, 72–75 (1996).

Bou-Diab M, Dodgson MJW and Blatter G. Vortex collisions: Crossing or recombination. *Physical Review Letters*, **86**, 5132–5135 (2001).

Brandt EH. The flux-line lattice in superconductors. *Reports on Progress in Physics*, **58**, 1465–1594 (1995).

Brass A, Jensen HJ and Berlinsky A. Models of flux pinning in the quasi-static limit. *Physical Review B*, **39**, 102–116 (1989).

Braun D, Crabtree GW, Kaper HG, Koshelev AE, Leaf G, Levine DM and Vinokur VM. Structure of a moving vortex lattice. *Physical Review Letters*, **76**, 831 (1996).

Brézin E, Nelson DR and Thiaville A. Fluctuation effects near H_{c2} in type-II superconductors. *Physical Review B*, **31**, 7124–7132 (1985).

Buckel W. *Supraleitung. Grundlagen und Anwendungen*. VCH Verlagsgesellschaft, Weinheim, Germany, 5th edition (1993).

Bulaevskii LN, Ledvij M and Kogan VG. Distorted vortex in josephson-coupled layered superconductors. *Physical Review B*, **46**, 11807–11812 (1992).

Bulaevskii LN, Meshkov SV and Feinberg D. Evaporation of a single vortex line in a weakly coupled multilayered superconductor. *Physical Review B*, **43**, 3728–3731 (1991).

Buzdin A and Feinberg D. *J. Phys. (France)*, **51**, 1971 (1990).

Caillol JM, Levesque D, Weis JJ and Hansen JP. A Monte Carlo study of the classical two-dimensional one-component plasma. *Journal of Statistical Physics*, **28**(2), 325–349 (1982).

Carpentier D and Le Doussal P. Melting of two-dimensional solids on disordered substrates. *Physical Review Letters*, **81**, 1881–1884 (1998).

Chaikin PM and Lubensky TC. *Principles of condensed matter physics*. Cambridge University Press, Cambridge (1995).

Choquard P. Cooperative phenomena below melting of the one-component two-dimensional plasma. *Physical Review Letters*, **50**, 2086–2089 (1983).

Clem JR. Two-dimensional vortices in a stack of thin superconducting films: A model for high-temperature superconducting multilayers. *Physical Review B*, **43**, 7837–7846 (1991).

Clem JR. Anisotropy and two-dimensional behaviour in the high-temperature superconductors. *Supercond. Sci. Technol.*, **11**, 909–914 (1998).

Cox SJ, Daniell GJ, Fangohr H and Robinson AM. An $\mathcal{O}(N)$ multipole algorithm for the 2d Helmholtz equation (2001). Submitted.

Cubitt R, Forgan EM, G GY, Lee SL, Paul DM, Mook HA, Yethiraj M, Kes PH, Li TW, Menovsky AA, Tarnawski Z and Mortensen K. Direct observation of magnetic-flux lattice melting and decomposition in the high-T_C superconductor $Bi_{2.15}Sr_{1.95}CaCu_2O_{8+X}$. *Nature* (1993).

de Berg M, van Kreveld M, Overmars M and Schwarzkopf O. *Computational Geometry*. Springer Verlag, Berlin (1997).

de Leeuw SW and Perram JW. Statistical mechanis of two-dimensional coulomb systems. *Physica*, **113A**, 546–558 (1982).

de Leeuw SW, Perram JW and Smith ER. Simulation of electrostatic systems in periodic boundary conditions. I. Lattice sums and dielectric constants. *Proceedings of the Royal Society of London*, **373**, 27–56 (1980).

Dodgson MJW, Geshkenbein VB, Feigel'man M and Blatter G. Self-consistent theory of the thermal softening and instability of simple crystals. *cond-mat/0007072* (2000a).

Dodgson MJW, Koshelev AE, Geshkenbein VB and Blatter G. Evaporation of the pancake-vortex lattice in weakly coupled layered superconductors. *Physical Review Letters*, **84**, 2698–2701 (2000b).

Domínguez D. Dynamic transition in vortex flow in strongly disordered Josephson junction arrays and superconducting thin films. *Physical Review Letters*, **82**, 181–184 (1999).

Doyle RA, Khaykovich B, Konczykowski M, Zeldov E, Morozov N, Majer D, Kes P and Vinokur V. Vortex matter phase transitions in $Bi_2Sr_2CaCu_2O_8$. *Physica C*, **282-287**, 323–326 (1997).

Ewald PP. Die Berechnung optischer und elektrostatischer Gitterpotentiale. *Annalen der Physik*, **64**, 253–287 (1921).

Faleski MC, Marchetti MC and Middleton AA. Vortex dynamics and defects in simulated flux flow. *Physical Review B*, **54**, 12427–12436 (1996).

Fangohr H, Cox SJ and de Groot PAJ. Vortex dynamics in two-dimensional systems at high driving forces. *Physical Review B*, **64**, 064505 (2001a).

Fangohr H, de Groot PAJ and Cox SJ. Critical transverse forces in weakly pinned driven vortex systems. *Physical Review B*, **63**, 064501 (2001b).

Fangohr H, Koshelev AE and Dodgson MJW. Vortex matter in layered superconductors without josephson coupling: numerical simulations within mean field approach. *cond-mat/0210580* (2002). Submitted to Phys. Rev. B.

Fangohr H, Price A, Cox S, de Groot PAJ, Daniell GJ and Thomas KS. Efficient methods for handling long-range forces in particle-particle simulations. *J. Comput. Phys*, **162**, 372–384 (2000).

Feigel'man MV, Geshkenbein VB and Larkin AI. Pinning and creep in layered superconductors. *Physica C*, **167**, 177–187 (1990).

Ferrenberg AM and Swendsen RH. New Monte Carlo technique for studying phase transitions. *Physical Review Letters*, **61**, 2635–2638 (1988).

Ferrenberg AM and Swendsen RH. Optimized Monte Carlo data analysis. *Physical Review Letters*, **63**, 1195–1198 (1989).

Frigo M and Johnson SG. FFTW : an adaptive software architecture for the FFT. In *1998 ICASSP conference proceedings*, volume 3, pages 1381–1384 (1998).

Fruchter L. Metastable states of a driven flux lattice in a superconductor with strong pins. *Physica C*, **370**, 157–162 (2002a).

Fruchter L. Transition to plastic motion as a critical phenomenon and anomalous interface layer of a 2d driven vortex lattice. *Eur. Phys. J. B*, **25**, 313–317 (2002b).

Geometry Centre. Center for the computation and visualization of geometric structures. www.geom.umn.edu (1999).

Giamarchi T and Le Doussal P. Elastic theory of pinned flux lattices. *Physical Review Letters*, **72**, 1530–1534 (1994).

Giamarchi T and Le Doussal P. Elastic theory of flux lattices in the presence of weak disorder. *Physical Review B*, **52**, 1242–1270 (1995).

Giamarchi T and Le Doussal P. Moving glass phase of driven lattices. *Physical Review Letters*, **76**, 3408–3411 (1996).

Giamarchi T and Le Doussal P. *Spin Glasses and Random fields*, chapter Statics and Dynamics of Disordered Elastic Systems. World Scientific (1998).

Ginzburg VL and Landau LD. *Zh. Eksperim. Teor. Fiz.*, **20**, 1064 (1950).

Goertzel G. An algorithm for the evaluation of finite trigonometric series. *American mathematical monthly*, **34** (1958).

Gordeev S (2000). Private communication.

Gorkov LP. *Sov. Phys.—JETP*, **9**, 1364 (1959).

Gradshteyn IS and Ryzhik IM. *Table of Integrals, Series, and Products*. Academic Press (1994).

Greengard L and Rohklin V. A fast algorithm for particle simulations. *J. Comp. Phys.*, **73**, 325 (1987).

Grier DG, Murray CA, Bolle CA, Gammel PL and Bishop DJ. Translational and bond-orientational order in the vortex lattice of the high-T_c superconductor $Bi_{2.1}Sr_{1.9}Ca_{0.9}Cu_2O_{8+\delta}$. *Physical Review Letters*, **66**, 2270–2273 (1991).

Grigorenko AN, Bending SJ, Fangohr H, Bael MJV, Bekaert J, Lange M and Moshchalkov VV. Symmetry locking and domain formation in commensurate structures (2002). In preparation for submission.

Grønbech-Jensen N. Summation of logarithmic interactions in periodic media. *Intern. J. Mod. Phys. C*, **7**, 873–881 (1996).

Grønbech-Jensen N, Bishop AR and Domínguez D. Metastable filamentary vortex flow in thin film superconductors. *Physical Review Letters*, **76**, 2985–2988 (1996).

Gropp WD, Kaper HG, Leaf GK, Levine DM, Palumbo M and Vinokur VM. Numerical simulation of vortex dynamics in type II superconductors. *J. Comp. Phys.*, **123**, 254–266 (1996).

Groth J, Reichhardt C, Olson CJ, Field SB and Nori F. Vortex plastic motions in twinned superconductors. *Physical Review Letters*, **77**, 3625–3628 (1996).

Haile JM. *Molecular Dynamics Simulation, Elementary Methods*. John Wiley & Sons, professional paperback edition (1997).

Hellerqvist MC, Ephorn D, White WR, Beasley MR and Kapitulnik A. Vortex dynamics in two-dimensional amorphous $Mo_{77}Ge_{23}$ films. *Physical Review Letters*, **76**, 4022–4025 (1996).

Higgins MJ and Bhattacharya S. Varieties of dynamics in a disordered flux-line lattice. *Physica C*, **257**, 232–254 (1996).

Jensen HJ, Brass A and Berlinsky AJ. Lattice deformations and plastic flow through bottlenecks in a two-dimensional model for flux pinning in type-II superconductors. *Physical Review Letters*, **60**, 1676–1679 (1988).

Johansen T, Baziljevich M, Shantsev D, Goa P, Galperin Y, Kang W, Kim H, Choi E, Kim MS and Lee S. Dendritic magnetic instability in superconducting MgB_2 films. *cond-mat/0104113* (2002). In press, Europhys. Lett.

Kamerlingh Onnes H. *Leiden Comm.*, **120b** (1911).

Khaykovich B, Konczykowski M, Zeldov E, Doyle RA, Majer D, Kes PH and Li TW. Vortex-matter phase transitions in $Bi_2Sr_2CaCu_2O_8$: Effects of weak disorder. *Physical Review B*, **56**, R517–R520 (1997).

Kittel C. *Introduction to Solid State Physics*. John Wiley & sons, 7th edition (1996).

Klein T, Joumard I, Blanchard S, Marcus J, Cubitt R, Giamarchi T and Le Doussal P. A Bragg glass phase in the vortex lattice of a type II superconductor. *Nature*, **413**, 404 (2001).

Kohandel M and Kardar M. Melting of flux lines in an alternating parallel current. *Physical Review B*, **59**, 9637–9641 (1999).

Kokkaliaris S, de Groot PAJ, Gordeev SN and Zhukov AA. Onset of plasticity and hardening of the hysteretic response in the vortex system of $YBa_2Cu_3O_{7-\delta}$. *Physical Review Letters*, **82**, 5116–5119 (1999).

Kolton AB, Domínguez D and Grønbech-Jensen N. Hall noise and transverse freezing in driven vortex lattices. *Physical Review Letters*, **83**, 3061–3064 (1999).

Kolton AB, Domínguez D and Grønbech-Jensen N. Dynamical ordering in the c-axis in 3d driven vortex lattices. *cond-mat/0002017* (2000a).

Kolton AB, Domínguez D, Olson CJ and Grønbech-Jensen N. Driven vortices in 3d layered superconductors: Dynamical ordering along the c-axis. *Physical Review B*, **62**, R14657 (2000b).

Koshelev AE (2002). Private Communication.

Koshelev AE and Vinokur VM. Dynamic melting of the vortex lattice. *Physical Review Letters*, **73**, 3580–3583 (1994).

Kubo R, Toda M and Hashitsume N. *Statistical Physics II, Nonequilibrium Statistical Mechanics*. Springer-Verlag (1985).

Kunchur MN, Christen DK and Phillips JM. Observation of free flux flow and high dissipation levels in $YBa_2Cu_3O_{7-\delta}$ epitaxial films. *Physical Review Letters*, **70**, 998–1001 (1993).

Larkin AI and Ovchinnikov YV. Pinning in type II superconductors. *J. Low. Temp. Phys.*, **34**, 409–427 (1979).

Lawrence WE and Doniach S. In E Kanda, editor, *Proceedings of the Twelfth International Conference on Low Temperature Physics*, page 361. Academic Press of Japan, Kyoto (1971).

Le Doussal P. Private communication (1999).

Le Doussal P and Giamarchi T. Moving glass theory of driven lattices with disorder. *Physical Review B*, **57**, 11356–11403 (1998).

Le Doussal P and Giamarchi T. Dislocations and Bragg glasses in two dimensions. *Physica C*, **331**, 233–240 (2000).

Lekner J. Summation of dipolar fields in simulated liquid vapor interfaces. *Physica A*, **157**, 826–838 (1989).

Lekner J. Summation of Coulomb fields in computer-simulated disordered-systems. *Physica A*, **176**, 485–498 (1991).

Lenk R and Gellert W. *Fachlexikon abc Physik*, volume 1. Harri Deutsch, Frankfurt/M., Leipzig, 2nd edition (1989).

Li YH and Teitel S. Phase transitions and vortex-line entanglement in a model high-temperature superconductor. *Physical Review B*, **49**, 4136–4144 (1994).

Lindemann F. *Phys. Z. (Leipzig)*, **11**, 69 (1910).

London F and London H. The electromagnetic equations of the supraconductor. *Proceedings of the Royal Society of London*, **A149**, 71–88 (1935).

Marconi VI and Domínguez D. Transverse depinning and melting of a moving vortex lattice in driven periodic josephson junction arrays. *Physical Review Letters*, **82**, 4922–4925 (1999).

Metropolis NA, Rosenbluth AW, Rosenbluth MN, Teller AH and Teller E. Equation of state calculations by fast computing machins. *J. Chem. Phys.*, **21**, 1087–1092 (1953).

Molinari M, Fangohr H, Generowicz J and Cox SJ. Finite element optimizations for efficient non-linear electrical tomography reconstruction. In *Proceedings of the 2nd World Congress on Industrial Process Tomography*, pages 406–417 (2001).

Moon K, Scalettar RT and Zimányi GT. Dynamical phases of driven vortex systems. *Physical Review Letters*, **77**, 2778–2781 (1996).

Morozov N, Zeldov E, Majer D and Koczykowski M. Paramagnetic ac susceptibility at the first-order vortex-lattice phase transition. *Physical Review B*, **54**, R3784–R3877 (1996).

Nagamatsu J, Nakagawa N, Muranaka T, Zenitani Y and Akimitsu J. Superconductivity at 39 K in magnesium diboride. *Nature*, **410**, 63 (2001).

Nattermann T. Scaling approach to pinning: Charge density waves and giant flux creep in superconducters. *Physical Review Letters*, **64**, 1530–1533 (1990).

Nelson DR. Vortex entanglement in high-T_c superconductors. *Physical Review Letters*, **60**, 1973 (1988).

Nguyen AK and Sudbø A. Topological phase fluctuations, amplitude fluctuations, and criticality in extreme type-II superconductors. *Physical Review B*, **60**, 15307–15331 (1999).

Nordborg H and Blatter G. Vortices and 2d bosons: A path-integral Monte Carlo study. *Physical Review Letters*, **79**, 1925–1928 (1997).

Nordborg H and Blatter G. Numerical study of vortex matter using the bose model: First-order melting and entanglement. *Physical Review B*, **58**, 14556–14571 (1998).

Olive E and Brandt EH. Point defects in the flux-line lattice of superconductors. *Physical Review B*, **57**, 13861–13871 (1998).

Olson C, Reichhardt C, Scalettar R, Zimanyi G and Gronbech-Jensen N. Disordering transitions in vortex matter: Peak effect and phase diagram. *cond-mat/0008350* (2000a).

Olson C, Reichhardt C and Vinokur V. Hysteretic depinning and dynamical melting for magnetically interacting vortices in disordered layered superconductors. *cond-mat/0010002* (2001).

Olson CJ and Grønbech-Jensen N. Depinning and dynamic phases in driven three-dimensional lattices in anisotropic superconductors. *Physica C*, **341-348**, 1083 (2000).

Olson CJ and Reichhardt C. Transverse depinning in strongly driven vortex lattices with disorder. *Physical Review B*, **61**, R3811–R3814 (2000).

Olson CJ, Reichhardt C and Nori F. Fractal networks, braiding channels, and voltage noise in intermittently flowing rivers of quantized magnetic flux. *Physical Review Letters*, **80**, 2197–2200 (1998a).

Olson CJ, Reichhardt C and Nori F. Nonequilibrium dynamic phase diagram for vortex lattices. *Physical Review Letters*, **81**, 3757–3760 (1998b).

Olson CJ, Scalettar RT, Zimányi GT and Grønbech-Jensen N. The effect of splayed pins on vortex creep and critical currents. *Physical Review B*, **62**, R3612–R3615 (2000b).

Omeltchenko A, Campbell TJ, Kalia RK, Liu X, Nakano A and Vashishta P. Scalable I/O of large-scale molecular dynamics simulations: A data-compression algorithm. *Computer. Phys. Commun.*, **131**, 78–85 (2000).

Pardo F, de la Cruz F, Gammel PL, Bucher E and Bishop DJ. Observation of smectic and moving-Bragg-glass phases in flowing vortex lattices. *Nature*, **396**, 348–350 (1998).

Pardo F, De La Cruz F, Gammel PL, Oglesby CS, Bucher E, Batlogg B and Bishop DJ. Topological defects in the flux-line lattice and their relationship the critical current of a type-II superconductor. *Physical Review Letters*, **78**, 4633–4636 (1997).

Pearl J. *Appl. Phys. Lett.*, **5**, 65 (1964).

Pilkington JR and Baden SB. Dynamic partitioning of non-uniform structured workloads with spacefilling curves. *IEEE Transactions on Parallel and Distributed Systems*, **7**, 288–299 (1996).

Pippard AB. An experimental and theoretical study of the relation between magnetic field and current in a superconductor. *Proceedings of the Royal Society of London*, **A216**, 547–568 (1953).

Press WH, Teukolsky SA, Vetterling WT and Fannery BP. *Numerical Recipes in Fortran*. Cambridge University Press, 2nd edition (1992).

Press WH, Teukolsky SA, Vetterling WT and Fannery BP. *Numerical Recipes in C*. Cambridge University Press, 2nd edition (1995).

Price AR. *Hybrid Monte Carlo Studies of High Temperature Superconductors*. Ph.D. thesis, University of Southampton (2000).

Price AR, Fangohr H, Cox SJ and de Groot PA. Monte Carlo simulation of layered high temperature superconductors. *Physica C*, **341-348**, 1303–1304 (2000).

Rademacher M. Single molecules feel the force. *Physics World*, pages 33–37, September (1999).

Rae AIM, Forgan EM and Doyle RA. The interpretation of magnetisation and entropy jumps in the mixed state of high-temperature superconductors. *Physica C*, **301**, 301–314 (1998).

Rapaport DC. *The Art of Molecular Dynamics Simulation*. Cambridge University Press, Cambridge, Great Britain, 1st edition (1995).

Reichhardt C and Nori F. Phase locking, devil's staircases, farey trees, and Arnold tongues in driven vortex lattices with periodic pinning. *Physical Review Letters*, **82**, 414–417 (1999).

Ryu S, Doniach S, Deutscher G and Kapitulnik A. Monte Carlo simulation of flux lattice melting in a model high-T_c superconductor. *Physical Review Letters*, **68**, 710–713 (1992).

Ryu S, Hellerqvist M, Doniach S, Kapitulnik A and Stroud D. Dynamical phase transition in a driven disordered vortex lattice. *Physical Review Letters*, **77**, 5114–5118 (1996).

Ryu S and Stroud D. First-order melting and dynamics of flux lines in a model for $YBa_2Cu_3O_{7-\delta}$. *Physical Review B*, **54**, 1320–1333 (1996).

Scheidl S and Vinokur VM. Driven dynamics of periodic elastic media in disorder. *Physical Review E*, **57**, 2574–2593 (1998).

Seshadri R and Westervelt RM. Statistical mechanics of magnetic bubble arrays. I. topology and thermalization. *Physical Review B*, **46**, 5142–5149 (1992).

Shi AC and Berlinsky AJ. Pinning and I-V characteristics of a two-dimensional defective flux-line lattice. *Physical Review Letters*, **67**, 1926–1929 (1991).

Spencer S and Jensen HJ. Absence of translational ordering in driven vortex lattices. *Physical Review B*, **55**, 8473–8481 (1997).

Täuber UC and Nelson DR. Interactions and pinning energies in the bose glass phase of vortices in superconductors. *Physical Review B*, **52**, 16106–16124 (1995).

Theunissen MH, Van der Drift E and Kes PH. Size effects in flow of flux-line solids and liquids. *Physical Review Letters*, **77**, 159–162 (1996).

Thorel R. Fabrication et étude d'un monochristal de vortex dans le niobium supraconducteur. *J. Phys. (Paris)*, **34**, 447–452 (1973).

Tinkham M. *Introduction to Superconductivity*. McGraw-Hill, 2nd edition (1996).

Tirado-Rives J and Jorgensen WL. Molecular-dynamics simulations of the unfolding of apomyoglobin in water. *Biochemistry*, **32**, 4175–4184 (1993).

Troyanovski AM, Aarts J and Kes PH. Collective and plastic motion in superconductors at high flux densities. *Nature*, **399**, 665–668 (1999).

van Otterlo A, Scalettar RT and Zimanyi GT. Phase diagram of disordered vortices from London Langevin simulations. *Physical Review Letters*, **81**, 1497–1500 (1998).

Verlet L. Computer 'experiments' on classical fluids. I. thermodynamical properties of Lennard-Jones molecules. *Phys. Rev.*, **159**, 98–103 (1967).

Vinokur V, Khakovich B, Zeldov E, Konczykowski M, Doyle RA and Kes PH. Lindemann criterion and vortex-matter phase transition in high-temperature superconductors. *Physica C*, **295**, 209–217 (1998).

Watson GN. *Theory of Bessel functions*. Cambridge University Press, Cambridge, 2nd edition (1944).

Wilkin NK and Jensen HJ. Decoupling and melting in a layered superconductor. *Europhysics Letters*, **40**, 423–428 (1997a).

Wilkin NK and Jensen HJ. Disorder driven destruction of a phase transition in the vortex system of a superconductor. *Physical Review Letters*, **79**, 4254–4257 (1997b).

Yang DY, Grama A and Sarin V. Bounded-error compression of particle data from hierarchical approximate methods. In *Proceedings of Supercomputing (CDROM)*. Portland (1999).

Yaron U, Gammel PL, Huse DA, Kleiman RN, Oglesby CS, Bucher E, Batlogg B, Bishop DJ, Mortensen K, Clausen K, Bolle CA and De La Cruz F. Neutron diffraction studies of flowing and pinned magnetic flux lattices in 2H-$NbSe_2$.

Physical Review Letters, **73**, 2748 (1994).

Yates K, Newman DJ and de Groot PAJ. Monte Carlo simulation of two-dimensional flux lattice melting. *Physica C*, **241**, 111–117 (1995).

Yazdani A, Howald CM, White WR, Beasley MR and Kapitulnik A. Competition between pinning and melting in the two-dimensional vortex lattice. *Physical Review B*, **50**, 16117–16120 (1994).

Yazdani A, White WR, Hahn MR, Gabay M, Beasley MR and Kapitulnik A. Observation of Kosterlitz-Thouless-type melting of the disordered vortex lattice in thin films of *a*-MoGe. *Physical Review Letters*, **70**, 505–508 (1993).

Zeldov E, Majer D, Konczykowsik M, Vinokur VM, Geshkenbein VB and Shtrikman H. Nature of the irreversibility line in $Bi_2Sr_2CaCu_2O_8$. *Nature*, **375**, 373 (1995).

Zhu BY, Xing DY, Dong J and Zhao BR. Dynamical phase transition of a driven vortex lattice with disordered pinning. *Physica C*, **311**, 140–150 (1999).